

1998

Synthetic aperture radar imaging of embedded objects in dielectric slabs

Geoffrey J. Zhang
Iowa State University

Follow this and additional works at: <https://lib.dr.iastate.edu/rtd>

 Part of the [Electrical and Electronics Commons](#)

Recommended Citation

Zhang, Geoffrey J., "Synthetic aperture radar imaging of embedded objects in dielectric slabs " (1998). *Retrospective Theses and Dissertations*. 11828.

<https://lib.dr.iastate.edu/rtd/11828>

This Dissertation is brought to you for free and open access by the Iowa State University Capstones, Theses and Dissertations at Iowa State University Digital Repository. It has been accepted for inclusion in Retrospective Theses and Dissertations by an authorized administrator of Iowa State University Digital Repository. For more information, please contact digirep@iastate.edu.

INFORMATION TO USERS

This manuscript has been reproduced from the microfilm master. UMI films the text directly from the original or copy submitted. Thus, some thesis and dissertation copies are in typewriter face, while others may be from any type of computer printer.

The quality of this reproduction is dependent upon the quality of the copy submitted. Broken or indistinct print, colored or poor quality illustrations and photographs, print bleedthrough, substandard margins, and improper alignment can adversely affect reproduction.

In the unlikely event that the author did not send UMI a complete manuscript and there are missing pages, these will be noted. Also, if unauthorized copyright material had to be removed, a note will indicate the deletion.

Oversize materials (e.g., maps, drawings, charts) are reproduced by sectioning the original, beginning at the upper left-hand corner and continuing from left to right in equal sections with small overlaps. Each original is also photographed in one exposure and is included in reduced form at the back of the book.

Photographs included in the original manuscript have been reproduced xerographically in this copy. Higher quality 6" x 9" black and white photographic prints are available for any photographs or illustrations appearing in this copy for an additional charge. Contact UMI directly to order.

UMI

A Bell & Howell Information Company
300 North Zeeb Road, Ann Arbor, MI 48106-1346 USA
313:761-4700 800:521-0600

Synthetic aperture radar imaging of embedded objects
in dielectric slabs

by

Geoffrey J. Zhang

A dissertation submitted to the graduate faculty
in partial fulfillment of the requirements for the degree of
DOCTOR OF PHILOSOPHY

Major: Electrical Engineering (Electromagnetics)

Major Professor: Dr. Hsiu C. Han

Iowa State University

Ames, Iowa

1998

Copyright © Geoffrey J. Zhang, 1998. All rights reserved.

UMI Number: 9826589

**Copyright 1998 by
Zhang, Geoffrey J.**

All rights reserved.

**UMI Microform 9826589
Copyright 1998, by UMI Company. All rights reserved.**

**This microform edition is protected against unauthorized
copying under Title 17, United States Code.**

UMI
300 North Zeeb Road
Ann Arbor, MI 48103

Graduate College
Iowa State University

This is to certify that the Doctoral dissertation of
Geoffrey J. Zhang
has met the dissertation requirements of Iowa State University

Signature was redacted for privacy.

Major Professor

Signature was redacted for privacy.

For the Major Program

Signature was redacted for privacy.

For the Graduate College

I would like to dedicate this Ph.D. dissertation to Professor Yushi Sun. Without his valuable help I would not have been able to further my graduate studies here at Iowa State University.

TABLE OF CONTENTS

ACKNOWLEDGMENTS	xiv
ABSTRACT	xv
GENERAL INTRODUCTION	1
PART I DEVELOPMENT OF ALGORITHMS FOR	
ONE-DIMENSIONAL INVERSION PROBLEMS	
CHAPTER 1 INTRODUCTION TO PART I	4
1.1 Inverse Problems and NDE	4
1.2 Solution Methods for Inverse Problems	4
1.3 Motivation for Research and Scope of Part I	6
CHAPTER 2 GEOMETRIC MODEL AND WKB SOLUTION	7
2.1 Geometric Model	7
2.2 WKB Solution	8
CHAPTER 3 FOUR INVERSION ALGORITHMS	13
3.1 Algorithm I — Use $R(k; z = 0)$ for Lossless Case	13
3.2 Algorithm II — Use $ R(k; z) $ for Lossless Case	15
3.3 Algorithm III — Use $R(k; z = 0)$ for Low-Loss Case	19
3.4 Algorithm IV — Use $ R(k; z) $ for Low-Loss Case	21
CHAPTER 4 NOISE EFFECTS	24
CHAPTER 5 SIMULATION EXAMPLES	27

CHAPTER 6	EXPERIMENTAL RESULTS	33
6.1	Experimental Setup	33
6.2	Data Correction	34
6.3	Inversion Results	35
CHAPTER 7	CONCLUSION TO PART I	37
PART II	SAR IMAGING OF EMBEDDED OBJECTS	
	INSIDE DIELECTRIC SLABS	38
CHAPTER 8	INTRODUCTION TO PART II	39
8.1	Background	39
8.2	Motivation for Research	41
8.3	Arrangement of Part II	42
CHAPTER 9	BASIC ISSUES REGARDING SAR IMAGING	43
9.1	Point Target Model and SFCW Monostatic Mode	43
9.1.1	Point Target Model	43
9.1.2	SFCW Mode	44
9.1.3	Monostatic Mode	45
9.2	Focusing Techniques	45
9.2.1	SAR Technique	45
9.2.2	Focusing Technique	49
9.2.3	Matched Filtering Technique	50
9.3	Doppler Shift	51
9.3.1	Stop-and-Go Mode	52
9.4	Sampling Criteria	53
9.4.1	Temporal-Frequency-Domain Sampling	53
9.4.2	Space-Domain Sampling	54
9.4.3	Data Interpolation	56

9.5	Sidelobe Suppression	57
9.6	Inflection Point Calculation	58
CHAPTER 10 SAR IMAGING OF OBJECTS IN HOMOGENEOUS		
	MEDIUM	61
10.1	$f - x$ Method	62
10.2	$t - x$ Method	63
10.3	Recovering Observable Signals	64
	10.3.1 Basic Concept	64
	10.3.2 Simulation Examples	66
10.4	$f - \phi$ Method	66
10.5	Comparison of Different Methods	69
CHAPTER 11 STFT AND $t - x - \theta$ METHOD		
	71	
11.1	STFT Technique	72
	11.1.1 Continuous Time STFT	72
	11.1.2 Discrete Time STFT	73
11.2	$f - x - \phi$ Method and $t - x - \theta$ Method	74
11.3	Single Target Identification With Zero Bandwidth	75
CHAPTER 12 EXPERIMENTAL CASE STUDIES		
	80	
12.1	Background	80
12.2	Experimental Setup	81
12.3	Data Preprocessing	83
	12.3.1 Specular Reflection Removal	83
	12.3.2 Horn Antenna Mismatch Removal	87
	12.3.3 Distance Determination	88
	12.3.4 Refractive Index Estimation Based On Distance Domain Signal	89
12.4	Image Formation and Processing	90

LIST OF TABLES

Table 5.1	Reproduced data for Example 1 by Algorithms I and II	27
Table 5.2	Reproduced data for Example 2 by Algorithm III	28
Table 5.3	Reproduced data for Example 3 by Algorithm IV	28
Table 5.4	Reproduced data for Example 4 by Algorithms I and II	30
Table 5.5	Reproduced data for Example 4 using geometrical model	31
Table 5.6	Reproduced data for Example 5 by Algorithm II	31
Table 5.7	Reproduced data for Example 6 by Algorithm II	32
Table 6.1	Inversion result from experimental data	35
Table 11.1	Mean and Variance for x_0 and y_0	76
Table 13.1	Seven different cases of target distributions	100
Table 13.2	Comparison of n_r obtained via different methods	108
Table 15.1	Comparison of separations between wires	124

LIST OF FIGURES

Figure 2.1	Relative permittivity profile.	7
Figure 2.2	TE wave in defined coordinates.	8
Figure 3.1	Relation between θ and d_{min} for different values of ϵ_r	16
Figure 5.1	Three relative permittivity profiles $\epsilon_r(z)$	29
Figure 5.2	Complex plane plot of $R(k)$ for Profile 3.	31
Figure 6.1	Experimental set-up.	33
Figure 6.2	Plot of normalized seven measurements of reflection coefficients at different distances for obtaining normalized correction factor.	36
Figure 6.3	Plot of $ R(k) ^2$: “solid line” is theoretical curve; “dashed line” is experimental curve with metal plate correction; “dotted line” is experimental curve with accurate formula correction [27]; and “dash-dotted line” is experimental curve with simplified formula correction [25].	36
Figure 9.1	Different scanning modes: (a) monostatic mode, and (b) bistatic mode.	46
Figure 9.2	Different modes produce different results: (a) little signal is received in the monostatic mode, and (b) strong signal is received in the bistatic mode.	47
Figure 9.3	A target under illumination between positions x_m and x_n	48

Figure 9.4	Geometry for deriving spatial frequencies.	54
Figure 9.5	A curve showing the normalized stepsize reduces as θ_b increases. . .	56
Figure 9.6	Two different ways of interpolation produces different results. . . .	57
Figure 9.7	Ray bended at the boundary of two different media.	59
Figure 9.8	Two extreme paths and true path.	60
Figure 10.1	Geometry for SAR imaging when targets and antenna are in the same medium.	62
Figure 10.2	Images of one target formed by using different data attributes: (a) complex data, (b) real part of the data, (c) imaginary part of the data, and (d) magnitude of the data.	67
Figure 10.3	Images of two targets formed by using different data attributes: (a) complex data, and (b) real part of the data.	68
Figure 10.4	Evolution of an image when more antenna length is added. (Description is in the text.)	70
Figure 11.1	Filter banks and down-sampling by a factor of m	77
Figure 11.2	STFT windows and the corresponding looking angles.	77
Figure 11.3	$x - \phi$ relationship for a single target case.	78
Figure 11.4	$x - \phi$ relationship after edge detection is performed.	79
Figure 11.5	Target coordinates retrieved from different antenna locations: (a) x -coordinates, and (b) y -coordinates.	79
Figure 12.1	Spatial spectra: (top) specular reflection; (bottom) point-target scattering.	82
Figure 12.2	Experimental setup.	83
Figure 12.3	Targets arrangement on Plexiglas slab: (left) for Experiment I, and (right) for Experiment II.	84
Figure 12.4	Spatial spectrum for all temporal frequencies.	85

Figure 12.5	Spatial spectrum at 95 GHz: (a) before specular reflection is removed, and (b) after specular reflection is removed.	85
Figure 12.6	Notch filter shapes for different values of ξ	86
Figure 12.7	Distance domain image showing horn antenna mismatch which corresponds to the dark bands near the bottom.	86
Figure 12.8	Signal part due to horn antenna mismatch ($x = -70$).	87
Figure 12.9	Dimensions of antenna horn used for experiment.	88
Figure 12.10	Signal part showing little antenna horn mismatch after specular reflection removal ($x = -70$).	88
Figure 12.11	Signals due to interface specular reflections ($x = -70$).	89
Figure 12.12	Signals due to interface specular reflections at four different antenna positions: (a) $x = -70$ mm, (b) $x = -30$ mm, (c) $x = 10$ mm, and (d) $x = 50$ mm.	90
Figure 12.13	Images from Experiment I with different widths of notch filters. (a) $\xi = 0$, (b) $\xi = 0.005$, (c) $\xi = 0.01$, (d) $\xi = 0.05$, (e) $\xi = 0.08$, and (f) $\xi = 0.15$	91
Figure 12.14	Split images to reveal weak targets.	93
Figure 12.15	Positive and negative looking images to reveal weak targets. (a) positive looking image, and (b) negative looking image.	94
Figure 12.16	Images for Experiment II: (a) without specular reflection removal ($\xi = 0$), and (b) with specular reflection removal ($\xi = 0.05$).	95
Figure 12.17	SAR image for Experiment II with dimensions denoted.	96
Figure 13.1	2-D cross-correlation results for seven different cases.	99
Figure 13.2	Images for different values of n_r for Case 4 (three targets). Top row is for $n_r = 1.6$, middle row is for $n_r = 2.0$ (true value), and bottom row is for $n_r = 2.4$	101

Figure 13.3	Flowchart showing the process for obtaining ϵ and d from SAR imaging data using Algorithm II developed in Part I.	103
Figure 13.4	Experimental setup for single wire experiment.	104
Figure 13.5	Cross-correlation result of two images at different refractive indices for single wire experiment.	105
Figure 13.6	Image for single wire experiment with $n_r = 1.6$	105
Figure 13.7	Cross-correlation result of two images at different refractive indices for double wire experiment.	106
Figure 13.8	Image for double wire experiment with $n_r = 1.6$	106
Figure 13.9	Cross-correlation result of two images at different refractive indices for triple wire experiment.	108
Figure 13.10	Image for triple wire experiment with $n_r = 1.6$	108
Figure 15.1	One possible geometry for InSAR: two antennas are separated only by a vertical (z -direction) distance.	113
Figure 15.2	Setup for InSAR Experiment I: (a) a metallic plate with two holes in it, and (b) experimental setup with the plate tilted by 25° to reduce specular reflection.	115
Figure 15.3	Intensity images formed using data collected from antennas at different elevations: (a) image corresponding to lower antenna, and (b) image corresponding to upper antenna.	116
Figure 15.4	Zoomed-in intensity images showing simple image registration: (a) image related to lower antenna data, (b) image related to upper antenna data, (c) image in (b) shifted in x -direction by 6 pixels (1.2 mm), (d) image in (c) scaled up by 11.4%.	118
Figure 15.5	Zoomed-in interferograms. (a) before registration, (b) after registration.	119

Figure 15.6	Setup for InSAR Experiment II: three short vertical metallic wires (about 20 mm in length) are attached to the front of a Plexiglas board.	120
Figure 15.7	Two intensity images corresponding to (a) upper antenna, and (b) lower antenna.	121
Figure 15.8	Registration through minimizing function g	122
Figure 15.9	Interferograms: (a) before image registration, and (b) after image registration.	123
Figure A.1	Relative permittivity profile.	127
Figure A.2	Magnitudes of reflection coefficients for Case 1.	131
Figure A.3	Magnitudes of reflection coefficients for Case 2.	131

ACKNOWLEDGMENTS

I would like to express my gratitude to my major advisor, Dr. Hsiu C. Han, for introducing me to microwave NDE from a totally different background and for providing me the opportunity to pursue my Ph.D. I enjoyed our numerous discussions, appreciated the uncountable amount of time he spent with me in this research, and valued his constant encouragement. All this will no doubt direct me throughout my life.

I would also like to thank Dr. William Lord, Dr. Dragan Mirković, Dr. Satish S. Udpa, and Dr. Robert J. Weber for taking the time to serve on my committee and for providing much useful advice along the way.

I would also like to thank my fellow graduate student, Edward S. Mansueto, for various kinds of help during my study at Iowa State University.

ABSTRACT

This Ph.D. dissertation is composed of three parts. In Part I, simple, fast and practical algorithms for solving one-dimensional nonlinear inverse problems are proposed. The thickness and permittivity of a dielectric slab can be determined from frequency-domain data. Prior knowledge of the exact distance between the antenna and the slab surface is not required for the inversion, thus making the method applicable under practical conditions. Furthermore, the method is extended to low-loss situations in which the dielectric permittivity is a complex number. Noise effect has been studied, indicating the robustness of the algorithms with respect to noise. Both computer simulations and laboratory experiments show that the proposed algorithms turn out accurate and reliable results. In Part II, synthetic aperture radar (SAR) imaging of embedded objects inside dielectric slabs is studied. First, basic issues regarding SAR imaging especially for our setting are addressed. Then, three different approaches for reconstructing images are analyzed, and their advantages and disadvantages discussed and compared. Although the Doppler shift frequency does not exist in the setting of our study, the concept of antenna's physical looking angles is introduced instead and their relationship to spatial spectra provided. Based on this new outlook, the technique of short-time Fourier transform (STFT) is employed to provide a three-dimensional data set linking together the looking angle, time, and antenna location. Consequently, an effective and powerful method for estimating the relative permittivity of the host dielectric material is developed. This greatly facilitates SAR imaging of embedded objects in reality. Case studies based on experimental data are provided using algorithms developed in both Part I and Part II. It is shown that

through one experimental scan we are not only able to image the objects embedded inside the sample, but also able to retrieve the effective permittivity. This eliminates the requirement of either the prior knowledge of the material permittivity or the exercise of a pre-experiment to determine it. In Part III, preliminary studies have been conducted on interferometric SAR (InSAR) for forming three-dimensional imagery. Good indications have been obtained from lab experiments.

GENERAL INTRODUCTION

Microwave (which roughly covers 0.3 to 300 GHz) nondestructive evaluation (NDE) has been used in a great number of applications, ranging from large scale remote sensing to detection of tumors in the body. Comparing to conventional NDE methods, microwave NDE techniques offer particularly useful properties in evaluating dielectric composite materials thanks to their low dielectric losses which provide good depth of penetration of electromagnetic waves in this band.

The goal of the present research is to image embedded objects inside dielectric media without requirement of knowing in advance the dielectric properties of the host material. Thus, the algorithms for this purpose should possess the ability of forming an image while generating the dielectric permittivity. Conventionally, the dielectric properties are required before imaging is possible. This is usually accomplished either with some prior knowledge or by conducting an experiment in advance to obtain the necessary knowledge before the imaging process starts. Two groups of algorithms have been developed to this end. The first group contains inversion algorithms which are able to retrieve the permittivity and the thickness of a dielectric slab in a simple, fast, and accurate manner. The second group of algorithms proposed is capable of not only forming the image of the embedded objects, but also estimating the permittivity of the host material during the imaging process. The essence of the algorithms lies in the flexibility of converting SAR data among four different domains, namely, the time-domain, the temporal-frequency-domain, the space-domain, and the spatial-frequency-domain in order to reveal the information more clearly and separate signal due to different causes. This allows us to reduce specular reflections

from slab surfaces and horn antenna mismatch, and to judiciously use the signal part coming from a certain direction (a particular looking angle) while disregarding the signals from other directions. These techniques render clearer image on the one hand, and permit two different images of the same scene to be created on the other, which, in turn, provides an estimation of the permittivity of the host material. Validation with experimental data processed by both groups of algorithms is provided. The possibility of three-dimensional SAR imaging is also studied, indicating a promising potential.

The dissertation is composed of three parts. In Part I, four algorithms are developed for solving one-dimensional inversion problems. In Part II, SAR imaging technique is studied and the related algorithms developed. In Part III, preliminary studies have been conducted in forming three-dimensional imagery via interferometric SAR.

PART I

**DEVELOPMENT OF ALGORITHMS FOR
ONE-DIMENSIONAL INVERSION PROBLEMS**

CHAPTER 1 INTRODUCTION TO PART I

1.1 Inverse Problems and NDE

In the past few decades, inverse scattering problems have been widely studied due to their ever increasing applications. The solutions have been used in target identification, system design and optimization, medical imaging, material characterization, geophysical survey, remote sensing, and nondestructive evaluation. Although many different methods have been developed, most are only valid restricted to theory under many assumptions. In fact, even the seemingly simplest problems turn out to be quite difficult to solve.

An inverse problem involves looking for causes from results; a forward problem, on the other hand, is to find results based on known causes. Therefore, the former corresponds to a synthesis procedure, and the latter an analysis procedure.

1.2 Solution Methods for Inverse Problems

Usually, inverse problems can be approached from three different view points [1]. These three approaches are: (1) the database approach, (2) the iterative approach, and (3) the explicit solution approach. Each of these three approaches is briefly described below.

(1) The *database approach*: In this approach, a result (e.g., a measurement) is compared with the pre-stored patterns in a database to identify the possible causes. The effectiveness of this method relies on the completeness of previous experiences. The advantage of this method is that the causes can be quickly identified if the responses of such targets have been recorded. The disadvantage of this method is that we are not able to find the causes if the corresponding target pattern is not found in our database. In this

case, we either take a similar response as our solution or resort to other methods.

(2) The *iterative approach*: In this approach, a forward model for calculating results from various causes has to be set up before the inversion. For a given result, a guess of the causes is made and used as the input to the forward model. Adjustments to the guessed causes are continuously made until the result produced from the forward model matches the one given. Optimization schemes are often incorporated in this approach to minimize the error. There are both exact and approximate iterative methods. The effectiveness of the iterative approach depends on the complication of the forward model. However, convergence of the iterative approach is usually a question. Even if an iteration process converges, it may lead to a local minimum if there are multiple minima of the cost function. This results in a situation that the success of the iterative approach heavily depends on the accuracy of the initial guess. *A priori* knowledge of the parameters may be needed.

(3) The *explicit solution approach*: In this approach, a closed-form solution is obtained. Usually, explicit solution only exists for a few problems in practice. Hence, its application is restricted. However, it has great theoretical value. Examples of this method could be found in [2, 3, 4, 5]. The advantage of this method is that, with closed-form solutions, we can obtain the result fast.

One-dimensional inverse scattering theory could be traced back to Lord Raleigh [6]. In 1926, M. Born [7] developed an approximation method, now widely known as the *Born Approximation*, for solving weak scattering problems in quantum mechanics. In the years that follow, different methods have been developed using various assumptions and approximations. A partial list of achievements is given in [4, 5, 8, 9, 10, 11, 12, 13, 14]. Reference [15] provides a review on exact inverse methods in one dimension.

In [16], a very interesting scheme, called geometrical method, was devised for solving one dimensional scattering problems. Although it works well with simulated data, it has a few restrictions. One restriction is that this method can only deal with reflection

coefficients measured right at the surface of a dielectric slab. Another is it loses accuracy drastically in the presence of noise, which is inevitable in practice. Still another is that this method can only deal with lossless dielectric materials.

For lossy dielectric permittivity inversion the authors in [17] proposed a method based on the magnitudes of the reflection coefficients and of one transmission coefficient to determine the complex refractive index of concrete. Although the method only requires a single frequency, it demands the measurement of reflection coefficients at many incidence angles plus a transmission coefficient. Also, the thickness of the material must be known *a priori*.

1.3 Motivation for Research and Scope of Part I

The motivation for this part of the study arises from the fact that the property of the host material should be known before successful NDE methods could be applied and reliable results obtained.

In this part, algorithms that are more practical and less complicated in calculation than the geometrical method [16] are developed. These algorithms can also be used to deal with cases with low-loss dielectric materials.

This part is organized as follows. In Chapter 2, the mathematical model for one-dimensional reflection coefficient calculation of an inhomogeneous dielectric slab is established. Then, the WKB solution is formulated, which leads to the solution of reflection coefficient. In Chapter 3, four algorithms for retrieving dielectric slab parameters are developed. Two of them are for lossless cases and the other two for low-loss cases. In Chapter 4, noise effects on the accuracy of the inversion results are analyzed. In Chapter 5, simulation examples are provided to test the effectiveness of the developed algorithms. In Chapter 6, experimental validation is carried out and the reconstructed data are presented.

CHAPTER 2 GEOMETRIC MODEL AND WKB SOLUTION

2.1 Geometric Model

The geometry under consideration is a two-layer medium, with Region 1 being an inhomogeneous dielectric slab, and Regions 0 and 2 homogeneous half spaces. The relative permittivity profile (as shown in Fig. 2.1) is defined by

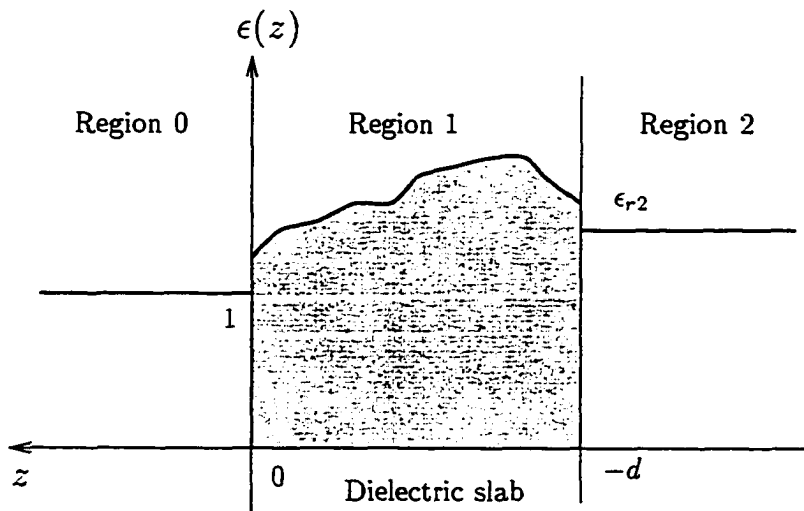


Figure 2.1 Relative permittivity profile.

$$\begin{cases} \epsilon_{r0}(z) = 1, & z > 0 \\ \epsilon_{r1}(z) = \epsilon_r(z), & 0 \geq z \geq -d \\ \epsilon_{r2}(z) = \epsilon_{r2}, & z < -d \end{cases} \quad (2.1)$$

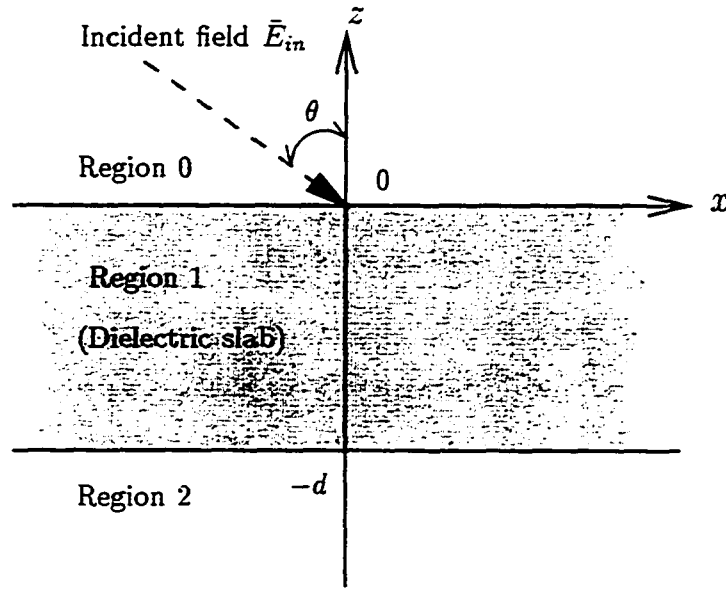


Figure 2.2 TE wave in defined coordinates.

It is assumed that the material is nondispersive (dispersionless) in the frequency range of interest, and that the permeability is equal to μ_0 , the free space permittivity (nonmagnetic).

2.2 WKB Solution

While the forward problem is to determine the reflection coefficient, $R(k)$, at $z \geq 0$ based on a given $\epsilon(z)|_{-d \leq z \leq 0}$, the inverse problem is to seek $\epsilon(z)$ from the reflection data, $R(k)$.

Suppose that a TE wave is impinging upon the slab from Region 0 at an angle θ , as shown in Fig. 2.2, and the “ $e^{-i\omega t}$ ” time convention is adopted, which is suppressed in all the following analysis, the Helmholtz equation, or the reduced wave equation, for this particular case is

$$\frac{d^2 \bar{E}^m}{dz^2} + k^2 [\epsilon_{r_m}(z) - \sin^2 \theta] \bar{E}^m = 0 \quad (2.2)$$

with $m = 0, 1, 2$, denoting Regions 0, 1, and 2, respectively. And

$$\bar{E}_{in} = \hat{y} E_0 e^{i(k_x x - k_z z)}$$

with

$$k_x = k \sin \theta, \quad k_z = k \cos \theta, \quad k = \omega \sqrt{\mu_0 \epsilon_0}$$

Since Regions 0 and 2 are homogeneous, the solutions for the \bar{E} -field are readily obtained as

$$\bar{E}^0 = \hat{y} E_0 (e^{-ik_z z} + R e^{ik_z z}) e^{ik_x x} \quad (2.3)$$

$$\bar{E}^2 = \hat{y} E_0 T e^{-ik_{2z} z} e^{ik_{2x} x} \quad (2.4)$$

where R and T are the reflection coefficient in Region 0 and the transmission coefficient in Region 2, respectively.

From the phase matching condition and the dispersion relations, it is obtained that

$$\left\{ \begin{array}{l} k_x = k_{1x} = k_{2x} = k \sin \theta \\ k_{1z} = \sqrt{k_1^2(z) - k_{1x}^2} = k \sqrt{\epsilon_r(z) - \sin^2 \theta} \\ k_{2z} = \sqrt{k_2^2 - k_{2x}^2} = k \sqrt{\epsilon_{r2} - \sin^2 \theta} \end{array} \right. \quad (2.5)$$

For Region 1, the WKB method [18] can be used to find an approximate solution for \bar{E}^1 . For this purpose, it is assumed that

$$\bar{E}^1 = \hat{y} E(z) e^{ik_x x}$$

Substituting this into (2.2) yields

$$\frac{d^2 E(z)}{dz^2} - k_x^2 E(z) + \omega^2 \mu_0 \epsilon_0 \epsilon_r(z) E(z) = 0$$

or,

$$\frac{d^2 E(z)}{dz^2} + k_{1z}^2 E(z) = 0 \quad (2.6)$$

Let

$$E(z) = Ae^{i\omega\tau(z,\omega)}$$

so that

$$\frac{d^2 E(z)}{dz^2} = \{i\omega\tau''(z,\omega) - \omega[\tau'(z,\omega)]^2\} Ae^{i\omega\tau(z,\omega)} \quad (2.7)$$

If $\nu = \frac{1}{\omega} \ll 1$, a perturbation series can be formed as follows,

$$\tau(z,\omega) = \tau_0(z) + \tau_1(z)\nu + \tau_2(z)\nu^2 + \dots \quad (2.8)$$

Substituting (2.8) into (2.7) produces

$$\frac{i}{\nu}[\tau_0'' + \tau_1''\nu + \tau_2''\nu^2 + \dots] - \frac{1}{\nu^2}[\tau_0' + \tau_1'\nu + \tau_2'\nu^2 + \dots]^2 + k_{1z}^2 = 0 \quad (2.9)$$

To form a system of differential equations, the terms in (2.9) are grouped according to their powers of ν . This is a valid approach¹ if

$$\frac{\tau_0''}{\nu} \ll \left(\frac{\tau_0'}{\nu}\right)^2 \quad (2.10)$$

Here, a first-order approximation is considered, i.e., the following two equations are solved,

$$k_{1z}^2 - \frac{1}{\nu^2}\tau_0'^2 = 0 \quad (2.11)$$

$$i\tau_0'' - 2\tau_0'\tau_1' = 0 \quad (2.12)$$

The corresponding solutions are

$$\tau_0(z) = \pm \int_0^z k_{1z}(z')\nu dz' \quad (2.13)$$

and

$$\tau_1(z) = i \ln \left(\sqrt{k_{1z}(z)\nu} \right) \quad (2.14)$$

By combining (2.7), (2.8), (2.13), and (2.14), we obtain

$$E(z) = \frac{A}{\sqrt{k_{1z}(z)/\omega}} e^{\pm i \int_0^z k_{1z}(z') dz'} \quad (2.15)$$

¹This condition is studied in Example 6 in Chapter 5.

Hence, the total electric field in Region 1 is

$$\bar{E}^1(z) = \hat{y} \frac{e^{ik_x x}}{\sqrt{k_{1z}(z)/\omega}} \left[A_+ e^{i \int_0^z k_{1z}(z') dz'} + A_- e^{-i \int_0^z k_{1z}(z') dz'} \right] \quad (2.16)$$

where, A , A_+ , and A_- are constants yet to be determined.

Before applying boundary conditions, the tangential components of the magnetic fields need to be formulated. From Maxwell's equation

$$\bar{H} = \frac{1}{i\omega\mu} \nabla \times \bar{E}$$

it is found that

$$\left\{ \begin{array}{l} H_x^0 = \frac{ik_z E_0}{i\omega\mu} (e^{-ik_z z} - R e^{ik_z z}) e^{ik_x x} \\ H_x^1 = \frac{i\sqrt{k_{1z}(z)\omega}}{i\omega\mu} (A_- e^{-i \int_0^z k_{1z}(z') dz'} - A_+ e^{i \int_0^z k_{1z}(z') dz'}) e^{ik_x x} \\ H_x^2 = \frac{ik_{2z} E_0 T}{i\omega\mu} e^{-ik_{2z} z} e^{ik_x x} \end{array} \right. \quad (2.17)$$

Define

$$I(z) = - \int_0^z k_{1z}(z') dz' \quad (2.18)$$

The four boundary conditions yield four algebraic equations. They are

$$\left\{ \begin{array}{l} E_0(1+R) = \frac{1}{\sqrt{k_{1z}(0)/\omega}} [A_+ + A_-] \\ E_0 T e^{ik_{2z} d} = \frac{1}{\sqrt{k_{1z}(-d)/\omega}} [A_+ e^{-iI(-d)} + A_- e^{iI(-d)}] \\ k_z E_0(1-R) = \sqrt{k_{1z}(0)\omega} [A_- - A_+] \\ k_{2z} E_0 T e^{ik_{2z} d} = \sqrt{k_{1z}(-d)\omega} [A_- e^{iI(-d)} - A_+ e^{-iI(-d)}] \end{array} \right. \quad (2.19)$$

Also define two constants as

$$R_{01} = \frac{k_z - k_{1z}(0)}{k_z + k_{1z}(0)} \quad (2.20a)$$

$$R_{12} = \frac{k_{1z}(-d) - k_{2z}}{k_{1z}(-d) + k_{2z}} \quad (2.20b)$$

and solve for R , the reflection coefficient measured at the front surface of the slab (i.e., $z = 0$), to get

$$R(k) = \frac{R_{01} + R_{12}e^{i2I(-d)}}{1 + R_{01}R_{12}e^{i2I(-d)}} \quad (2.21)$$

For homogeneous media, the above formula is seen to be the same as (26) presented on page 131 in [19].

The WKB solution derived above will be used as the foundation for the inversion algorithms. In turn, the accuracy of these algorithms also rely on the WKB assumptions.

CHAPTER 3 FOUR INVERSION ALGORITHMS

In this chapter four algorithms are developed for solving one-dimensional inverse scattering problems.

3.1 Algorithm I — Use $R(k; z = 0)$ for Lossless Case

Algorithm I deals with the reflection coefficient $R(k)$ obtained at $z = 0$ of a lossless dielectric slab. In order to obtain R_{01} and R_{12} , and, in turn, obtain constitutive parameters, long division on (2.21) is performed, which results in

$$R = R_{01} + \frac{R_{01}^2 - 1}{R_{01}} \sum_{n=1}^{\infty} (R_{01} R_{12} e^{i\gamma})^n (-1)^n \quad (3.1)$$

where, $\gamma = 2I(-d)$. In fact, (3.1) can also be obtained by the so-called *ray-tracing model* [20]. Before proceeding further, we need to know the period of either $\Re\{R\}$, or $\Im\{R\}$, or $|R|$ in k -domain, the wavenumber domain. In practice, this information can be obtained through actual measurement. Once the spectrum of one of the above quantities is known, the separation between two neighboring maxima or minima will provide us with the value of the period. For example, let two adjacent maxima be at k_1 and k_2 , respectively, then

$$\Delta\gamma = 2I(-d; k_2) - 2I(-d; k_1) = 2\pi$$

or

$$\gamma = 2I(-d) = 2\pi k / \Delta k \quad (3.2)$$

where $\Delta k = k_2 - k_1$ is the period in k over which the spectrum of R repeats itself. Making use of (3.2), one can rewrite (3.1) as

$$R(k) = R_{01} + \frac{R_{01}^2 - 1}{R_{01}} \sum_{n=1}^{\infty} (R_{01} R_{12} e^{i \frac{2\pi}{\Delta k} k})^n (-1)^n \quad (3.3)$$

Using orthogonality property for function $\exp(ix)$, namely, for $m, n = 0, \pm 1, \pm 2, \dots$,

$$\int_{\Delta k} e^{in \frac{2\pi}{\Delta k} k} e^{im \frac{2\pi}{\Delta k} k} dk = \begin{cases} \Delta k, & \text{if } m + n = 0 \\ 0, & \text{otherwise} \end{cases}$$

and integrating both sides of (3.3) produces (3.4a), then multiplying $e^{-i \frac{2\pi}{\Delta k} k}$ to both sides of (3.3) and again integrating produces (3.4b), i.e.,

$$R_{01} = \frac{1}{\Delta k} \int_{k_1}^{k_2} R(k) dk \quad (3.4a)$$

$$R_{12} = \frac{1}{(1 - R_{01}^2) \Delta k} \int_{k_1}^{k_2} R(k) e^{-i \frac{2\pi}{\Delta k} k} dk \quad (3.4b)$$

It is found from (2.20a), after obtaining R_{01} , that

$$\epsilon_r(0) = \sin^2 \theta + \cos^2 \theta \left(\frac{1 - R_{01}}{1 + R_{01}} \right)^2 \quad (3.5)$$

To obtain $\epsilon_r(-d)$ and ϵ_{r2} , two measurements at two different incidence angles, θ_1 and θ_2 , are required. As (2.20b) shows

$$R_{12}(\theta_i) = \frac{\sqrt{\epsilon_r(-d) - \sin^2 \theta_i} - \sqrt{\epsilon_2 - \sin^2 \theta_i}}{\sqrt{\epsilon_r(-d) - \sin^2 \theta_i} + \sqrt{\epsilon_{r2} - \sin^2 \theta_i}} \quad (3.6)$$

for $i = 1, 2$, and we arrive at

$$\epsilon_r(-d) = \frac{(1 - \alpha_{\theta_2}) \sin^2 \theta_2 - (1 - \alpha_{\theta_1}) \sin^2 \theta_1}{\alpha_{\theta_1} - \alpha_{\theta_2}} \quad (3.7)$$

and

$$\epsilon_{r2} = \alpha_{\theta_i} \epsilon(-d) + (1 - \alpha_{\theta_i}) \sin^2 \theta_i \quad (3.8)$$

where

$$\alpha_\theta = \left[\frac{1 - R_{12}(\theta)}{1 + R_{12}(\theta)} \right]^2$$

Furthermore, if the profile in Region 1 changes slowly, $I(-d)$ may be approximated by an one-step trapezoid integration, i.e.,

$$I(-d) \approx \frac{d}{2} [k_{1z}(0) + k_{1z}(-d)] \quad (3.9)$$

from which the thickness is estimated as

$$d \approx \frac{2\pi k}{\Delta k [k_{1z}(0) + k_{1z}(-d)]} = \frac{2\pi}{\Delta k \left[\sqrt{\epsilon_r(0) - \sin^2 \theta_i} + \sqrt{\epsilon_r(-d) - \sin^2 \theta_i} \right]} \quad (3.10)$$

As a special case, when the slab is homogeneous, (3.10) becomes

$$d = \frac{\pi k}{k_{1z}(0)\Delta k} = \frac{\pi k}{k_{1z}(-d)\Delta k} = \frac{\pi}{s\Delta k} \quad (3.11)$$

where $s = \sqrt{\epsilon_r - \sin^2 \theta}$.

The smallest value of d that can be retrieved is determined as follows: The frequency range of our w -band lab equipment is from 75 to 110 GHz. From (3.11) d_{min} is obtained as

$$d_{min} = \frac{\pi}{s \cdot \Delta f \cdot 2\pi/c} \approx \frac{4.286}{s} \quad (\text{mm}) \quad (3.12)$$

which is a function of both ϵ_r and θ . In (3.12), c is the speed of EM wave propagating in free space. Figure 3.1 shows the relationship between θ and d_{min} for several values of ϵ_r .

3.2 Algorithm II — Use $|R(k; z)|$ for Lossless Case

Algorithm II deals with the reflection coefficient measured at any arbitrary distance from the front surface of a lossless dielectric slab. The reflection coefficient given in (2.21) is defined at $z = 0$. In practice, however, it is easier to measure $R(k)$ at a certain distance, $z = d_0 > 0$, away from the interface. For this purpose we only need to modify (2.21) by adding a phase delay corresponding to the two-way distance, $2d_0$, and obtain

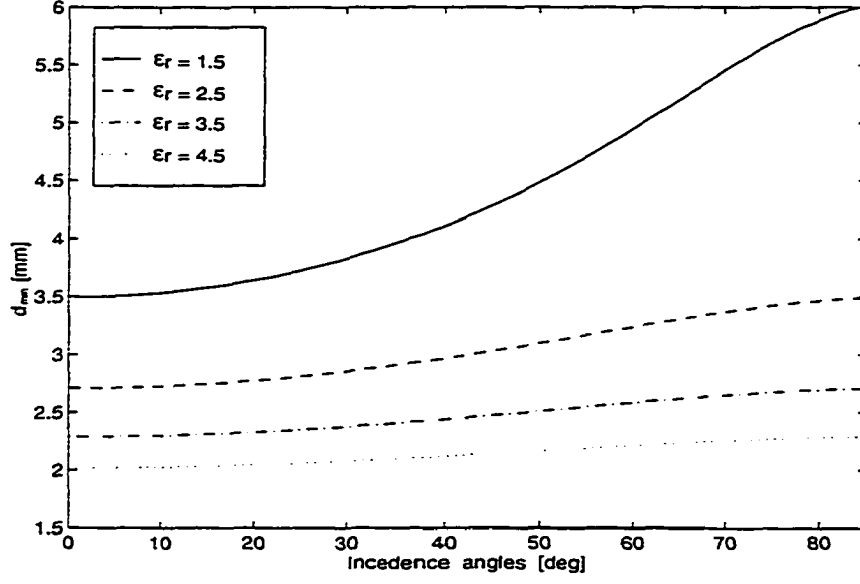


Figure 3.1 Relation between θ and d_{min} for different values of ϵ_r .

$$R(k) = \frac{R_{01} + R_{12}e^{i\gamma}}{1 + R_{01}R_{12}e^{i\gamma}} e^{i2k_z d_0} \quad (3.13)$$

Furthermore, the exact value of d_0 may be unknown, and a slight deviation from this true value will invalidate the algorithm proposed in [17]. More specifically, the reflection coefficient will generate a complicated picture instead of a nice circle in the complex R -plane. Algorithm II is developed to clear this hurdle. The goal is to remove the $e^{i2k_z d_0}$ factor from the inversion algorithm. One way of doing this is to take the modulus on both sides of (3.13), which leads to

$$\begin{aligned} |R(k)|^2 &= \frac{|R_{01} + R_{12}e^{i\gamma}|^2}{|1 + R_{01}R_{12}e^{i\gamma}|^2} |e^{i2k_z d_0}|^2 \\ &= \frac{R_{01}^2 + R_{12}^2 + 2R_{01}R_{12} \cos \gamma}{1 + R_{01}^2 R_{12}^2 + 2R_{01}R_{12} \cos \gamma} \\ &= \frac{\beta + \delta \cos \gamma}{1 + \delta \cos \gamma} \end{aligned} \quad (3.14)$$

where

$$\beta = \frac{(R_{01}^2 + R_{12}^2)}{(1 + R_{01}^2 R_{12}^2)} \quad (3.15a)$$

$$\delta = \frac{2R_{01}R_{12}}{(1 + R_{01}^2 R_{12}^2)} \quad (3.15b)$$

Expanding the denominator of (3.14) into a Taylor series results in

$$\frac{1}{1 + \delta \cos \gamma} = \sum_{n=0}^{\infty} (-1)^n \delta^n \cos^n \gamma \quad (3.16)$$

Substituting (3.16) into (3.14) yields

$$|R(k)|^2 = \beta + (\beta - 1) \sum_{n=1}^{\infty} (-1)^n \cos^n \gamma \delta^n \quad (3.17)$$

Now, we use the following trigonometric identities

$$\left\{ \begin{array}{l} \cos^{2n} x = \frac{1}{2^{2n-1}} \left\{ \sum_{m=0}^{n-1} C_{2n}^m \cos[(2n - 2m)x] + \frac{C_{2n}^n}{2} \right\} \\ \cos^{2n+1} x = \frac{1}{2^{2n}} \left\{ \sum_{m=0}^n C_{2n+1}^m \cos[(2n - 2m + 1)x] \right\} \\ C_m^j = \frac{m!}{j!(m-j)!} \end{array} \right.$$

to rearrange (3.17). In practice, if the precision is prescribed, the series described in (3.17) can then be truncated at a certain term due to the fact that $|\delta \cos \gamma| < 1$ is generally satisfied. For instance, if the truncation error is to be of the order of $\mathcal{O}(\delta^6)$, we have

$$\begin{aligned} |R|^2 &= f_0(\beta, \delta) + f_1(\beta, \delta) \cos \gamma + f_2(\beta, \delta) \cos 2\gamma + f_3(\beta, \delta) \cos 3\gamma \\ &\quad + f_4(\beta, \delta) \cos 4\gamma + f_5(\beta, \delta) \cos 5\gamma + \dots \end{aligned} \quad (3.18)$$

where

$$f_0(\beta, \delta) = \beta + \frac{1}{2}(\beta - 1)\delta^2 + \frac{3}{8}(\beta - 1)\delta^4 + \mathcal{O}(\delta^6) \quad (3.19a)$$

$$f_1(\beta, \delta) = (1 - \beta)\delta \left(1 + \frac{3}{4}\delta^2 + \frac{5}{8}\delta^4 \right) + \mathcal{O}(\delta^7) \quad (3.19b)$$

Expressions for f_m ($m \geq 1$) are not written out here explicitly because they are not independent of f_0 and f_1 , and are not necessary as a result. By

$$\int_{2\pi} \cos m\gamma \cos n\gamma dk = \begin{cases} 2\pi, & \text{if } m = n = 0 \\ \pi, & \text{if } m = n \neq 0 \\ 0, & \text{otherwise} \end{cases}$$

for $m, n = 0, \pm 1, \pm 2, \dots$, we obtain

$$f_0(\beta, \delta) = \frac{1}{\Delta k} \int_{\Delta k} |R(k)|^2 dk \quad (3.20a)$$

$$f_1(\beta, \delta) = \frac{2}{\Delta k} \int_{\Delta k} |R(k)|^2 \cos\left(\frac{2\pi}{\Delta k}k\right) dk \quad (3.20b)$$

From (3.19) and (3.20), β and δ can be solved simultaneously. There are many mathematical solvers we can resort to, such as MAPLE, MATHEMATICA, MATLAB, etc. What is necessary to point out is that usually more than one set of solutions is obtained, of which we have to discard but one based on our knowledge of the physical solution domain. Then, via (3.15a) and (3.15b) R_{01} and R_{12} are subsequently found. Similar to Algorithm I, the constitutive parameters and the thickness of the slab can be approximately determined using (3.5) through (3.11).

It is worth noting that there is one ambiguity in results which always exists as long as amplitude data are used. This ambiguity ends up with two sets of solutions with $\epsilon_r(0)$ and $\epsilon_r(-d)/\epsilon_{2r}$ interchangeable. The root cause of this is due to $|R(k)|$ is identical for lossless dielectric materials measured from either side of the slab when the dielectric property is the same for Region 0 and Region 2. The analogy by 1-D transmission line is that the corresponding scattering matrix always has the relation $|S_{11}| = |S_{22}|$. However, if $k_z \neq k_{2z}$, then $|R(k)|$ *would* be different for two different measurements from two sides, and the uniqueness of the solution is assured.

3.3 Algorithm III — Use $R(k; z = 0)$ for Low-Loss Case

Algorithm III is for the case when the reflection coefficient is measured at the front surface ($z = 0$) while the slab is made of a homogeneous lossy material. In this case, the relative permittivity of the slab is complex and can be expressed as

$$\epsilon_r = \epsilon^R + i\epsilon^I$$

The z -component of k_1 is now

$$k_{1z} = k \sqrt{\epsilon^R + i\epsilon^I - \sin^2 \theta} \quad (3.22)$$

Define

$$s = \sqrt{\epsilon^R - \sin^2 \theta}$$

which is a function of both z and θ . Take the following condition as the criterion for low loss

$$\frac{\epsilon^I}{s^2} \ll 1 \quad (3.23)$$

The expression for k_{1z} is simplified into

$$k_{1z} \approx k \left(s + \frac{i \epsilon^I}{2s} \right) \quad (3.24)$$

and

$$I(z) \approx -k \int_0^z \left(s + \frac{i \epsilon^I}{2s} \right) dz \quad (3.25)$$

When the slab is homogeneous, i.e., s , ϵ^R , and ϵ^I are independent of z , $I(-d)$ is simply

$$I(-d) = ksd + \frac{i k \epsilon^I d}{2s} \quad (3.26)$$

Thus,

$$i\gamma = i2I(-d) = i2ksd - \frac{k\epsilon^I d}{s} \quad (3.27)$$

with which (2.21) is reformulated as

$$R \approx \frac{R_{01} + R_{12} e^{i2ksd} e^{-\frac{ke^f d}{s}}}{1 + R_{01} R_{12} e^{i2ksd} e^{-\frac{ke^f d}{s}}} \quad (3.28)$$

where R_{01} and R_{12} are defined in (2.20a) and (2.20b) but are complex now. Expanding the denominator of (3.28), we obtain

$$R \approx R_{01} + \frac{1 - R_{01}^2}{R_{01}} \sum_{n=1}^{\infty} \left(R_{01} R_{12} e^{i2ksd} e^{-\frac{ke^f d}{s}} \right)^n (-1)^{n-1} \quad (3.29)$$

Integrate (3.29) over one period, we get

$$\int_{\Delta k} R(k) dk = R_{01} \Delta k + \frac{(1 - R_{01}^2)}{R_{01}} q + \mathcal{O}(q^2) \quad (3.30)$$

where

$$q = R_{01} R_{12} \int_{\Delta k} e^{i2ksd} e^{-\frac{ke^f d}{s}} dk \quad (3.31)$$

It can be shown that if

$$\left| \frac{(1 - R_{01}^2) R_{12}}{\Delta k R_{01}} \int_{\Delta k} e^{i2ksd} e^{-\frac{ke^f d}{s}} dk \right| \ll 1 \quad (3.32)$$

then, we can obtain R_{01} by

$$R_{01} \approx \frac{1}{\Delta k} \int_{\Delta k} R(k) dk \quad (3.33)$$

Working on the condition defined by (3.32) yields

$$\begin{aligned} & \left| \frac{(1 - R_{01}^2) R_{12}}{\Delta k R_{01}} \int_{\Delta k} e^{i2ksd} e^{-\frac{ke^f d}{s}} dk \right| \\ &= \frac{(1 - R_{01}^2)}{2sd\Delta k} \left| \frac{R_{12}}{R_{01}} \right| \frac{e^{-\frac{e^f}{s^2}(k_1 sd)} (1 - e^{-\pi \frac{e^f}{s^2}})}{\sqrt{1 + (\frac{2e^f}{s^2})^2}} \\ &\approx \frac{(1 - R_{01}^2)}{2sd\Delta k} \left| \frac{R_{12}}{R_{01}} \right| e^{-\frac{e^f}{s^2}(k_1 sd)} [1 - e^{-\pi \frac{e^f}{s^2}}] \end{aligned} \quad (3.34)$$

which leads to the following conclusions:

1. If the loss is very small, then

$$e^{-\pi \frac{\epsilon''}{s^2}} \rightarrow 1$$

Hence, the left-hand side of (3.32) approaches 0 and the condition is well satisfied. In this case, Algorithm III reduces to Algorithm I.

2. If d is rather large, then

$$e^{-\frac{\epsilon''}{s^2}(k_1 s d)} \rightarrow 0$$

Equation (3.32) is also well satisfied. This corresponds to the situation in which the reflection from the back surface can be ignored due to large thickness and EM energy decays to a negligible level along the paths. In fact, both “low loss” and “large thickness” are relative terms. “low loss” is compared with s value and “large thickness” compared wavelength.

Once R_{01} is obtained from (3.33), (3.5) can be used to calculate ϵ_r . It is worth noting that in [21] the authors claimed that the permittivity of small loss medium was calculated by the geometrical method proposed in [16] and the same criterion as that given in (3.23) was also used. This is, in fact, not possible. Serious errors were discovered in [21] in the related part of the derivation (see Section 2.3 of [22]).

3.4 Algorithm IV — Use $|R(k; z)|$ for Low-Loss Case

Algorithm IV is for the case when the reflection coefficient is measured at any arbitrary distance, say, $z = d_0$, away from the slab front surface, and the slab is made of homogeneous lossy dielectric material. The same procedure will be taken as that in Algorithm II to stamp out the d_0 term. To make things easier, we assume $\epsilon_{r2} = 1$. As a result, $R_{01} = -R_{12}$ and $\beta = -\delta$. We use the same assumptions as for Algorithm III, and define

$$\begin{cases} a = 2ksd \\ b = \frac{k\epsilon'' d}{s} \end{cases} \quad (3.35)$$

It is seen, similar to (3.14), that

$$\begin{aligned}
|R(k)|^2 &= \frac{|R_{01}|^2 |1 - e^{ia} e^{-b}|^2}{|1 - R_{01} e^{ia} e^{-b}|^2} |e^{i2k_z d_0}|^2 \\
&= \left(\frac{k_z - ks}{k_z + ks} \right)^2 + 2 \left(\frac{k_z - ks}{k_z + ks} \right)^2 \left[\frac{(k_z - ks)^2}{(k_z + ks)^2} \cos a \right. \\
&\quad \left. - \cos a + 2 \frac{(k_z - ks)}{(k_z + ks)^3} \frac{\epsilon^I k}{s} k_z \sin a \right] e^{-b} + \mathcal{O}(e^{-2b}) \\
&= \left(\frac{\cos \theta - s}{\cos \theta + s} \right)^2 + 2 \left(\frac{\cos \theta - s}{\cos \theta + s} \right)^2 \left[\frac{(\cos \theta - s)^2}{(\cos \theta + s)^2} \cos a \right. \\
&\quad \left. - \cos a + 2 \frac{(\cos \theta - s)}{(\cos \theta + s)^3} \frac{\epsilon^I}{s} \cos \theta \sin a \right] e^{-b} + \mathcal{O}(e^{-2b}) \quad (3.36)
\end{aligned}$$

Now, by curve fitting, $|R(k)|^2$ can be approximated by

$$F(k) = a_1 + (a_2 \cos x + a_3 \sin x) e^{-a_4 x} \quad (3.37)$$

in which, $a_m|_{m=1}^4$ are parameters to be determined. By comparing (3.37) to (3.36) it can be seen that

$$x = \frac{2\pi}{\Delta k} k \quad \text{and} \quad a_4 = \frac{\epsilon^I}{2s^2}$$

Once these parameters are found, they lead to ϵ^R , ϵ^I , and d , in the following fashion,

$$\epsilon^R = \left(\frac{1 + \sqrt{a_1}}{1 - \sqrt{a_1}} \right)^2 \cos^2 \theta + \sin^2 \theta \quad (3.38a)$$

$$\epsilon^I = 2s^2 = 2(\epsilon^R - \sin^2 \theta) \quad (3.38b)$$

$$d = \frac{\pi}{s\Delta k} = \frac{\pi}{\sqrt{\epsilon^R - \sin^2 \theta} \Delta k} \quad (3.38c)$$

In [17] an approach was proposed for the determination of dielectric constant of concrete using the absolute values of the reflection coefficient $|R|$ at several angles of incidence

θ and the absolute value of the transmission coefficient $|T|$ at normal incidence ($\theta = 0$). The complex refractive index n is estimated by a nonlinear-least-square method in which the theoretical expressions for the reflection and transmission coefficients are fitted. Although the method only uses one single frequency ($f = 57.5$ GHz), it demands the knowledge of the thickness of the slab. Also, the measurement is required for several incidence angles plus a transmission coefficient. In certain practical situations this is difficult to satisfy.

The refractive index obtained in [17] is $2.55 + i0.084$, which, obviously, meets the low-loss condition (3.23) defined previously. Presumably, Algorithm IV developed in this section would handle this same problem more elegantly.

CHAPTER 4 NOISE EFFECTS

In this chapter the noise effect on the accuracy of the above algorithms is studied. Our assumptions are: (i) the noise is additive, (ii) the noise has a normal distribution with zero mean and variance σ^2 , and (iii) the noise at different frequencies are *iid* (independently identically distributed). With these in mind, we proceed our analysis and denote the reflection coefficient contaminated by noise $n(k)$ as $\tilde{R}(k)$, which has the relation

$$\tilde{R}(k) = R(k) + n(k) \quad (4.1)$$

where, $n(k)$ is the noise at wavenumber k .

Substituting $\tilde{R}(k)$ into (3.4a) for calculating R_{01} , we obtain

$$\begin{aligned} \tilde{R}_{01} &= \frac{1}{\Delta k} \int_{k_1}^{k_2} \tilde{R}(k) dk \\ &= \frac{1}{\Delta k} \int_{k_1}^{k_2} [R(k) + n(k)] dk \end{aligned}$$

Approximating this integration by summation gives

$$\tilde{R}_{01} \approx \frac{1}{\Delta k} \sum [R(k_m) + n(k_m)] \delta k$$

where, the summation is implicitly understood as in terms of m , running from 1 to M . M is the number of data points within Δk . δk is the increment in wavenumber k . Thus

$$\begin{aligned} \tilde{R}_{01} &\approx \frac{1}{M} \sum R(k_m) + \frac{1}{M} \sum n(k_m) \\ &= \frac{1}{M} \sum R(k_m) + \bar{n}. \end{aligned} \quad (4.2)$$

Knowing that $n(k)$ has normal distribution, $n(k) \sim N(0, \sigma^2)$, it is obtained readily through the *central limit theorem* [23] that

$$\bar{n} \sim N\left(0, \frac{\sigma^2}{M}\right) \quad (4.3)$$

which says that \tilde{R}_{01} is much less affected by noise than $\tilde{R}(k)$ is, because the resultant effect has a much smaller variance than the one we start with. That is, \tilde{R}_{01} is “cleaner”.

For \tilde{R}_{12} , we resort to (3.4b) to obtain

$$\begin{aligned}\tilde{R}_{12} &= \frac{1}{(1 - \tilde{R}_{01}^2)\Delta k} \int_{k_1}^{k_2} \tilde{R}(k) e^{-i\frac{2\pi}{\Delta k}k} dk \\ &\approx \frac{\delta k}{(1 - \tilde{R}_{01}^2)\Delta k} \left[\sum R(k_m) e^{-i\frac{2\pi}{\Delta k}k_m} + \sum n(k_m) e^{-i\frac{2\pi}{\Delta k}k_m} \right] \\ &\approx \frac{1}{(1 - \tilde{R}_{01}^2)} \left[\frac{1}{M} \sum R(k_m) e^{-i\frac{2\pi}{\Delta k}k_m} + \frac{1}{M} \sum n(k_m) e^{-i\frac{2\pi}{\Delta k}k_m} \right]\end{aligned}$$

For the moment, we just analyze the second term inside the brackets, namely

$$\begin{aligned}\frac{1}{M} \sum n(k_m) e^{-i\frac{2\pi}{\Delta k}k_m} \\ = \frac{1}{M} \sum \cos\left(\frac{2\pi}{\Delta k}k_m\right) n(k_m) - i \frac{1}{M} \sum \sin\left(\frac{2\pi}{\Delta k}k_m\right) n(k_m)\end{aligned}\quad (4.4)$$

Define

$$Y = \frac{1}{M} \sum \cos\left(\frac{2\pi}{\Delta k}k_m\right) n(k_m)$$

then

$$\begin{aligned}E\{Y\} &= E\left\{\frac{1}{M} \sum \cos\left(\frac{2\pi}{\Delta k}k_m\right) n(k_m)\right\} \\ &= \frac{1}{M} \sum \cos\left(\frac{2\pi}{\Delta k}k_m\right) E\{n(k_m)\} \\ &= 0\end{aligned}\quad (4.5)$$

and

$$\begin{aligned}Var\{Y\} &= \frac{1}{M^2} \sum \cos^2\left(\frac{2\pi}{\Delta k}k_m\right) Var\{n(k_m)\} \\ &= \frac{\sigma^2}{M^2} \sum \cos^2\left(\frac{2\pi}{\Delta k}k_m\right) \\ &\approx \frac{\sigma^2}{2M^2}\end{aligned}\quad (4.6)$$

In the same manner, we can analyze the $\frac{1}{M} \sum \sin\left(\frac{2\pi}{\Delta k}k_m\right) n(k_m)$ term and obtain exactly the same conclusion for the mean and the variance. As with \tilde{R}_{01} , the noise effect on \tilde{R}_{12} is

also rather small due to the fact that the resultant noise effect has a normal distribution of zero mean and variance $\frac{\sigma^2}{2M}$, which is much smaller than σ^2 for comparatively large M . It is thus seen that both \bar{R}_{01} and \bar{R}_{12} are less sensitive to noise than $\bar{R}(k)$ is. A simulation example is provided in the next chapter. The conclusions obtained here have a great significance for practical applications where noise is unavoidable.

CHAPTER 5 SIMULATION EXAMPLES

Six simulation examples emphasizing on different aspects of the foregoing algorithms are provided in this chapter to show the validity of them.

- **Example 1**

In this example, we assume the parameters as

$$\epsilon_{r1} = 5, \quad \epsilon_{r2} = 2, \quad d = 10 \text{ (mm)}, \quad \theta = 45^\circ.$$

Using this information to generate R -spectrum, and then using Algorithms I and II to reproduce the parameters. The results are shown in Table 5.1.

Table 5.1 Reproduced data for Example 1 by Algorithms I and II

	ϵ_{r1}	ϵ_{r2}	d (mm)
Exact	5.0000	2.0000	10.00
Algorithm I	5.0651	2.0389	9.93
Algorithm II	5.0401	2.0307	9.96

- **Example 2**

In this example, a low-loss slab is simulated and the results are shown in Table 5.2. In all the three cases listed therein it is assumed that

$$\epsilon_{r2} = 2.0, \quad \epsilon^R = 3.0, \quad \epsilon^I = 0.2$$

with different incidence angles and/or slab thicknesses. Conditions (3.23) and (3.32) have been checked to hold.

Table 5.2 Reproduced data for Example 2 by Algorithm III

	θ	d (mm)	ϵ^R	Error(%)	ϵ^I	Error(%)
Case 1	45°	50	3.0946	3.15	0.2124	6.18
Case 2	0°	50	3.0795	2.65	0.2099	4.94
Case 3	0°	20	3.0361	1.20	0.2040	2.00

• **Example 3**

In this example, low-loss case is simulated and the results obtained from Algorithm IV are shown in Table 5.3. The difference between this one and Example 2 is that d_0 is unknown here.

Table 5.3 Reproduced data for Example 3 by Algorithm IV

	Exact	Reproduced ($\theta = 0^\circ$)	Error(%)	Reproduced ($\theta = 30^\circ$)	Error(%)
ϵ^R	2.5	2.5971	-3.885	2.5915	-3.661
ϵ^I	0.05	0.0595	-19.292	0.0573	-14.600
d(mm)	20	19.70	-1.5053	19.72	1.382
ϵ^R	2.5	2.5138	-0.552	2.5119	-0.476
ϵ^I	0.10	0.0999	0.116	0.1003	-0.252
d(mm)	20	20.08	-0.385	19.92	0.363
ϵ^R	2.5	2.5108	-0.433	2.5106	-0.424
ϵ^I	0.15	0.1588	-5.869	0.1508	-0.554
d(mm)	20	21.84	-0.921	19.93	0.334

• **Example 4**

In this example, the reflection coefficients for three nonlinear permittivity profiles (shown in Fig. 5.1) are calculated by multi-layer model [19] as well as WKB model. In Appendix A, the reflection coefficient from a slab with linearly varying permittivity is

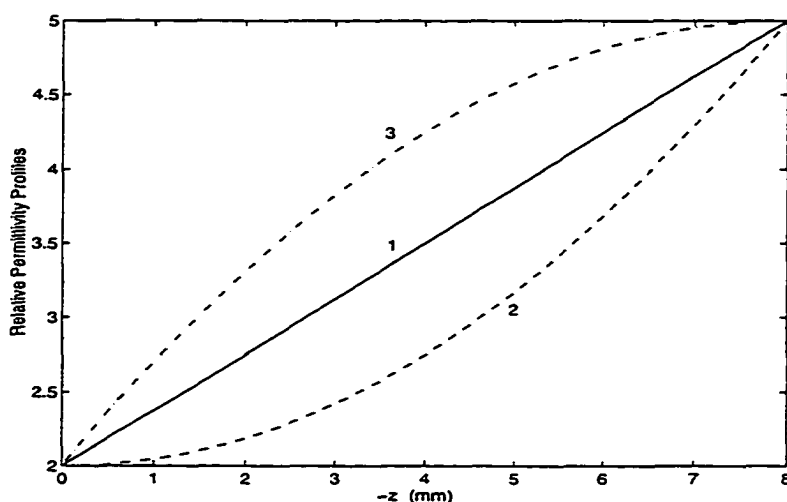


Figure 5.1 Three relative permittivity profiles $\epsilon_r(z)$.

derived. It is seen there that the multi-layer model works well as long as the number of layers is sufficiently large, which is dependent upon the permittivity profile, the thickness of the slab, and the frequency range being considered.

The inversion results are given in Table 5.4. From the reconstructed data it is seen that Profile 1 gives the best overall result. This is due to the fact that the maximum rate of change for profile is minimum for linear profile change among the three. Thus, WKB assumption, (2.10) is best satisfied.

It is noted that the reflection coefficient obtained through multi-layer method is no longer a circle centered on the real axis when plotted on the complex plane. Take Profile 3 for an example, the corresponding plot is shown in Fig. 5.2. The radii and the centers for the two circles are

$$r_1 = 0.59, \quad C_1 = -0.200 - i0.015$$

$$r_2 = 0.46, \quad C_2 = -0.147 - i0.015$$

If the imaginary parts of the C 's are ignored and the formulas provided in [16] are used to retrieve the parameters, we get Table 5.5. The inversion data are now far less accurate. Hence, the geometrical method works well only with WKB solution.

Table 5.4 Reproduced data for Example 4 by Algorithms I and II

	$\epsilon_{r1}(0)$	$\epsilon_{r1}(-d)$	ϵ_{r2}	d (mm)
Exact	2.0000	5.0000	1.0000	8.000
WKB-I-1 ^a	2.0001	5.0528	1.0062	8.133
I - 1	2.0058	4.9955	0.9994	8.166
I - 2 ^b	1.9963	4.9090	0.9827	7.522
I - 3	2.0300	4.9081	0.9815	8.805
II - 1	2.1603	5.0135	1.0631	7.779
II - 2	1.9227	5.0115	0.9672	7.262
II - 3	1.8071	5.0716	0.9191	8.735

^aWKB model used to generate R -spectrum and Algorithm I used for Profile 1.

^bMulti-layer model used to generate R -spectrum and Algorithm I used for Profile 2.

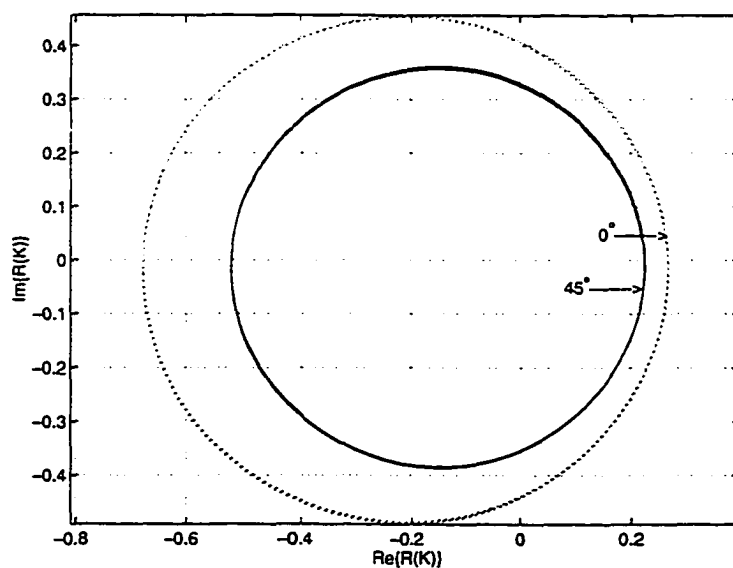
Figure 5.2 Complex plane plot of $R(k)$ for Profile 3.

Table 5.5 Reproduced data for Example 4 using geometrical model

$\epsilon_{r1}(0)$	$\epsilon_{r1}(-d)$	ϵ_{r2}
2.2550	6.1371	0.7902

• **Example 5**

In this example, Algorithm II is used under the influence of noise, which is assumed to be normally distributed. The noise is added to $R(k)$ in the following fashion: $R(k) + N(0, [\rho |R(k)|_{max}]^2)$. The simulated results for $\epsilon_{r1} = 3.0$ and $\epsilon_{r2} = 2.0$ are given in Table 5.6. It is observed that the retrieved data are close to their true values even with strong noise contamination.

Table 5.6 Reproduced data for Example 5 by Algorithm II

ρ	ϵ_1	Error(%)	ϵ_2	Error(%)
0.0000	3.00335	0.1115	1.99570	-0.2148
0.2948	3.00931	0.3103	2.04376	0.2188
0.5896	3.01379	0.4596	2.09156	4.5780
0.8844	3.01692	0.5622	2.13916	6.9580
1.0000	3.01775	0.5902	2.15777	7.8887

• **Example 6**

In this example, condition (2.10) is studied. Considering (2.10) and (2.13), we obtain an equivalent condition for WKB method to be a good approximation as

$$\frac{d\epsilon_{r1}(z)}{dz} \ll \frac{4\pi f}{c} (\epsilon_{r1}(z) - \sin^2 \theta)^{3/2} \quad (5.1)$$

which basically tells us that the rate of change of the permittivity profile should be within certain limit.

In evaluating (5.1), we require that $\min\{\epsilon_{r1}(z)\}$ be used for $\epsilon_{r1}(z)$, $\max\{\theta\}$ be used for θ , and $\min\{f\}$ be used for f on the right hand side of the equation. This is to guarantee that the above requirement be satisfied for every point of z within the slab.

If we assume that the permittivity changes linearly, and that

$$\epsilon_{r1}(0) = 2.0, \quad \epsilon_{r2} = 1.0, \quad d = 8, \text{ mm} \quad \theta_1 = 0^\circ, \quad \theta_2 = 40^\circ$$

we have

$$\frac{\epsilon_{r1}(-d) - \epsilon_{r1}(0)}{d} \ll \frac{4\pi \times 750}{3} [2.0 - \sin^2(40^\circ)]^{3/2} \Rightarrow \epsilon_{r1}(-d) \ll 41.74$$

Table 5.7 shows the reproduced data for $\epsilon_{r1}(-d)$ going from 2.1 up to 40.0. It is observed that even when $\epsilon_{r1}(-d) = 10.0$, the reconstructed parameters are still quite accurate. Beyond this point, the results start to go astray as the WKB assumptions are obviously violated.

Table 5.7 Reproduced data for Example 6 by Algorithm II

$\frac{\epsilon_{r1}(-d)}{\text{(exact)}}$	$\epsilon_{r1}(0)$	$\epsilon_{r1}(-d)$	Error (%)	ϵ_{r2}	d	Error (%)
2.1	2.0017	2.0877	0.586	0.9943	8.0161	0.20
2.5	2.0031	2.4863	0.548	0.9944	8.0088	0.11
3.0	2.0021	3.0248	0.827	1.0053	7.9794	0.26
4.0	2.0042	3.9636	0.91	0.9915	8.0201	0.25
5.0	2.0022	5.0532	1.06	1.0058	7.9709	0.36
8.0	2.0132	7.7608	2.99	0.9758	8.0663	0.83
10.0	2.0056	9.7869	2.13	0.9847	8.0509	0.64
15.0	1.9974	13.822	7.85	0.9428	8.2425	3.03
20.0	2.0022	19.700	1.50	0.9776	8.0453	0.57
25.0	2.0042	25.434	1.74	1.0086	7.9398	0.75
30.0	2.0051	23.982	20.06	0.9626	8.7727	9.66
40.0	1.9635	175.83	339.6	3.9584	4.5948	42.57

CHAPTER 6 EXPERIMENTAL RESULTS

6.1 Experimental Setup

A HP85106C millimeter-wave network analyzer system with HP W8510A test modules were used to generate, receive, and analyze signals in the 75 – 110 GHz range [24]. The setup of the experiment is sketched in Fig. 6.1. The sample used in the experiment is a piece of Plexiglas slab.

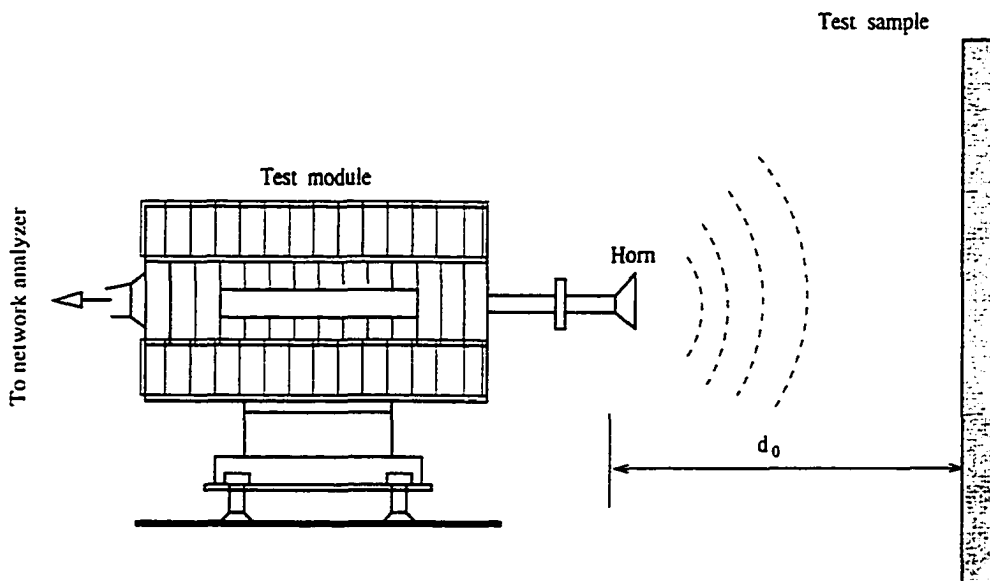


Figure 6.1 Experimental set-up.

As the derivations in the previous chapters are valid only for plan waves, the distance d_0 between the slab and the horn antenna should not be too small. Using the far zone condition, it is required that

$$d_0 > 2D^2/\lambda$$

where D is the horn aperture size. The standard gain horn antenna (25 dB) is used. Calibration procedures are performed to remove propagational and directivity errors before the experiment. Gating technique in time domain is applied to remove the mismatch effect between wave guide and the horn as well as the background noise from outside ranges.

6.2 Data Correction

The gain of the horn antenna and the attenuation of the field due to distance effect are compensated after the experimental data are recorded. There are two commonly used ways of performing compensation: one is to use theoretical calculations based on antenna geometry, and the other is to use experimental data for correction.

Fig. 6.2 displays the normalized measurement data of an aluminum-coated mirror taken as a perfect conductor. The normalization is done with respect to distance, which is approximately obtained from time domain data¹. The compensation factor, f_c , is obtained for each value of k through a quadratic polynomial fitting, producing

$$f_c = 3.056828533 \times 10^{-2} - 1.656249958 \times 10^{-5} k + 3.61785703 \times 10^{-9} k^2 \quad (6.1)$$

Note, f_c is valid for correcting any experimental data as long as the same antenna is used and d_0 satisfies roughly $260 \leq d_0 \leq 450$. For d_0 outside this range we should acquire new compensation factor through experiments. In fact, if permitted, it is advisable to obtain the compensation factor for each and every d_0 .

It is worth pointing out that, by using the ‘‘Gain’’ formulae from [25] and [27], the resultant correction factors are quite different, in both magnitudes and slopes, from the

¹It is seen here that we do not know the exact value of d_0 .

experimental results. The $|R|^2 \sim k$ plot is shown in Fig. 6.3. In the plot, the “solid line” is the theoretical curve; the “dashed line” is the experimental curve with metal plate correction; the “dotted line” is the experimental curve with the accurate formula correction [27]; and the “dash-dotted line” is the experimental curve with the simplified formula correction [25].

The reason that those formulae are not accurate enough is that too much simplification is made in the derivation. Reference [26] used edge-wave diffraction theory in an unconventional way to predict the field in the immediate vicinity of the aperture plane of a pyramidal microwave horn. The far field may then be inferred by Fourier transformation. We did not verify this approach because our goal here is to find a way which works and works well.

6.3 Inversion Results

Because the exact value of d_0 is not available in the experiment, we use Algorithm II to reproduce the parameters of the Plexiglas slab. The result is given in Table 6.1. Comparing with the W-band dielectric constant provided in [28], the relative error is found to be 0.81%. The error for the recovered thickness is about 0.53%. Both of them show good agreement with the theoretical values.

Table 6.1 Inversion result from experimental data

	ϵ_r	ϵ_{2r}	d (mm)
Reconstructed data	2.6311	1.1658	5.71
References data	2.61 ^a	1.00	5.68 ^b

^aobtained from Reference [28].

^bobtained from direct measurement.

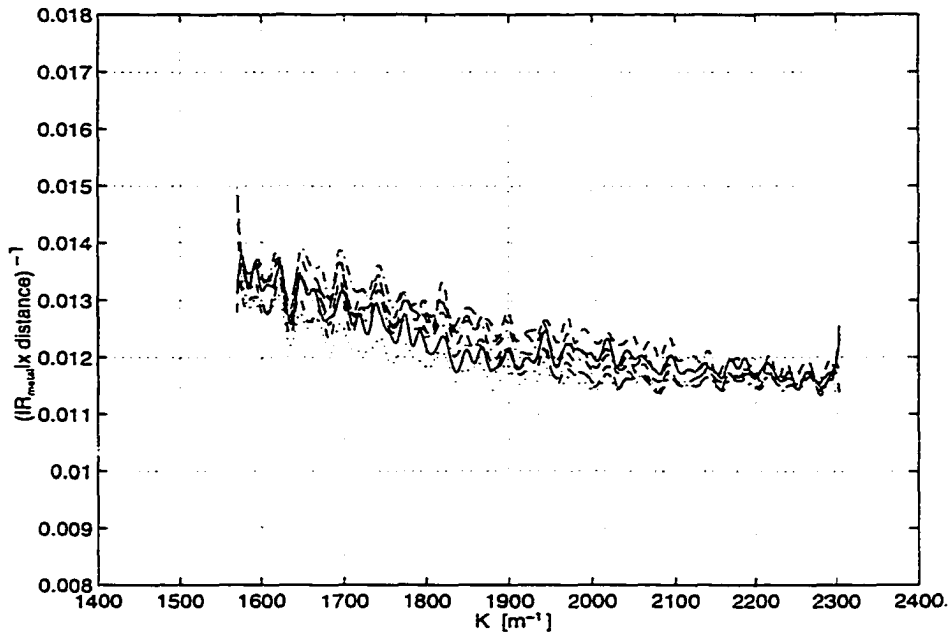


Figure 6.2 Plot of normalized seven measurements of reflection coefficients at different distances for obtaining normalized correction factor.

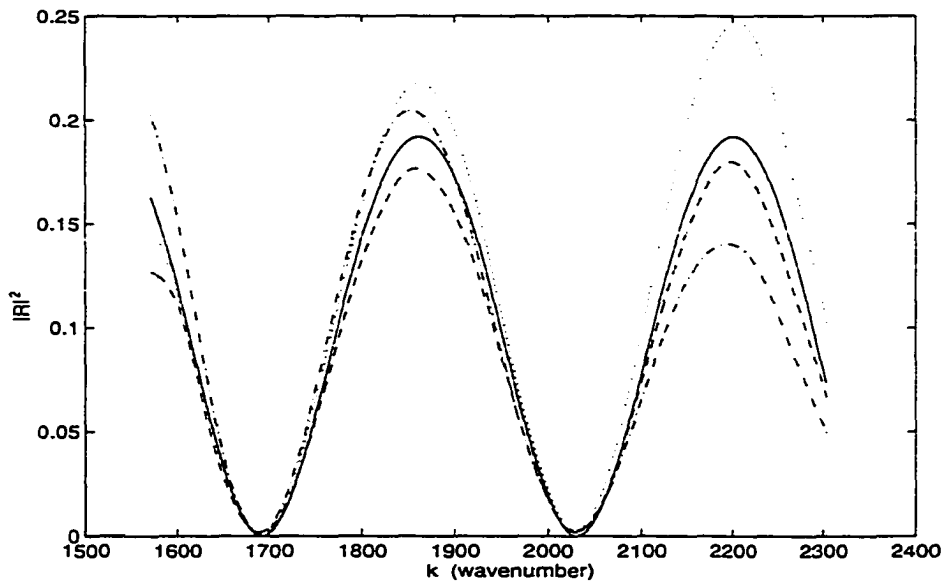


Figure 6.3 Plot of $|R(k)|^2$: “solid line” is theoretical curve; “dashed line” is experimental curve with metal plate correction; “dotted line” is experimental curve with accurate formula correction [27]; and “dash-dotted line” is experimental curve with simplified formula correction [25].

CHAPTER 7 CONCLUSION TO PART I

Simple, effective, and practical algorithms have been proposed in this part for solving one-dimensional nonlinear inversion problems. The solution is based on the WKB method and the properties of the corresponding reflection coefficient are studied. Achievements and original contributions have been made with these algorithms. First, the reflection coefficient of EM waves is no longer required to be measured right at the slab front surface. This bridges the gap between the theoretical study and the practical applications. Second, inversion problems under low-loss condition have been addressed. Third, the noise effect on the accuracy of the inversion results is analyzed, showing that the algorithms are robust with respect to noise influence. Finally, both the simulated and experimental results show the feasibility of these algorithms. The algorithms will be applied in Part II in forming SAR imagery of objects embedded in dielectric materials whose dielectric constants are not known.

PART II

**SAR IMAGING OF EMBEDDED OBJECTS INSIDE
DIELECTRIC SLABS**

CHAPTER 8 INTRODUCTION TO PART II

8.1 Background

Radar operates by transmitting a particular type of a waveform and detects the nature of the signal. Because radar supplies its own illumination, it has the day/night capability. Because radio waves propagate through clouds and rain with limited attenuation, it has the all-weather capability. Synthetic Aperture Radar (SAR) [30, 31] is developed based on the concept that a synthesized aperture is able to accomplish what would otherwise require a larger physical aperture.

Microwave imaging in general, and SAR imaging in particular, is an important growing technology in recent years [32] with the potential to produce high-resolution images for a variety of applications, including (1) analytical and physical simulation of radar target signatures for determining responses of radar sensors, (2) diagnostic methods for the identification and alteration of radar reflectivity components of complex objects, (3) non-destructive and noninvasive testing for imaging through media which support microwave propagation, and (4) object recognition systems which use the image as an identifier unique to a particular object. The traditional means of nondestructive evaluation, such as ultrasonics and eddy currents, albeit powerful in certain situations, may not be feasible in cases where the materials are dielectric. The former method causes too much attenuation, and the latter generates no response. Ultrasonics and eddy currents also may not work in situations which prevent contact or close-by testing.

SAR image formation can be viewed as the process of compressing a return signal by correlating it with a reference point target response [33]. In principle, the most general

SAR algorithm, time-domain convolution, computes an exact reference function and correlation for every image pixel. Other methods make approximations that trade performance for reduced complexity. These various algorithms differ in how they model the reference function and how they implement the correlation. Much of the difference in reference is due to operating conditions (radar frequency, aircraft vs. satellite platforms) and image requirements (size, resolution, etc.). Correlator implementation is affected by a number of factors including complexity of the reference function, processing-time requirements, and availability of radar and signal-processing hardware. No single image-formation technique is appropriate for all applications.

One of the important applications for SAR imaging is target detection. This area has been greatly studied. High resolution SAR technology is especially useful for detecting small targets embedded in strong ground clutter such as foliage. The key problem is the description of the statistical properties of radar clutter and noise. There are many articles in dealing with such problems. In [34] and [35] the authors considered removing local means as a preprocessing technique so that Gaussian assumption for clutter and noise is approximately valid. In [36] coherent subtraction was proposed as the preprocessing method. Here, one of the images is assumed to be target free and the other is to be sought in the presence of target. In [37] polarimetric SAR was considered for target detection. The three output images of the polarimetric SAR are first processed by a polarization whitening filter, whose output is next used with a two-parameter detector for target detection. In [38] an adaptive image formation was proposed to exploit the aspect-angle dependence of man-made scatterers in foliage penetrating SAR. The algorithm proposed identifies the locations that are likely to correspond to aspect-dependence scatterers. In the vicinity of such scatters, the algorithm chooses the aperture to match the expected return from a man-made scatterer. Elsewhere, the algorithm uses the full aperture.

Recently, considerable attention has also been directed to the use of airborne SAR for detecting both large and small underground objects. However, the common practice is to

rely on assumptions and algorithms developed in the context of free-space radar propagation [39, 40]. Although in some cases the implicit assumption of free-space propagation can lead to acceptable results, in other important cases it will result in severe degradation to images of underground objects. Reference [41] investigated the conditions under which significant improvements to image quality result if proper account is taken of the detailed effects of the soil medium on radar wave propagation.

Algorithms using spectral estimation methods have also been proposed. Basically, these algorithms were developed to compensate the disadvantages of Fourier methods [42]. Fourier SAR imaging exploits the Fourier transform pair relationship between signal history measurement (polar-to-rectangular [43] or migration [44] formatted) and scene reflectivity. Fourier imaging exhibits several drawbacks for imaging interferometric intensity and phase/height. And in this regard modern spectral estimation techniques offer attractive alternatives to Fourier SAR imaging. Other techniques such as artificial neural networks have also found its use in SAR imaging [45, 46].

8.2 Motivation for Research

The algorithms developed in Part I of this dissertation are able to reproduce parameters, such as permittivity and thickness, of dielectric slabs quickly as well as accurately. This is a very important issue as these parameters play an important role in SAR imaging of embedded objects in dielectric host materials. This is so because, during the process of SAR imaging, the phase of the received signal is of utmost importance due to the nature of coherent averaging in forming the image. Phase deviation from its true value will distort the image being sought. If the incorrect use of the host or the background refractive index is made, a significant phase error will accumulate.

To obtain the refractive index, conventionally, a separate measurement in advance is required for providing information regarding the host medium, for example, through a reflectometric measurement. However, this exercise may not be feasible or practical in

many applications. The goal here is to establish a composite approach to image targets in dielectric slabs. The main feature of this approach is that one can retrieve information on the embedded targets and the host medium from a single synthetic aperture measurement.

8.3 Arrangement of Part II

Part II contains seven chapters. In Chapter 9, some basic issues involving SAR imaging particularly tailored to our setting are addressed. In Chapter 10, three algorithms are presented assuming targets in a homogeneous medium. These algorithms are essentially equivalent in terms of the final results. This provides the freedom of selecting one specific algorithm best fitting the situation at hand. In Chapter 11, SAR imaging of embedded objects in dielectric materials is analyzed. Two important aspects are studied. One is the handling of specular reflections so that their effect on the resultant image is kept minimal; the other is the estimation of the dielectric permittivity of the host materials. This facilitates the practical application of the algorithms as a whole entity, i.e., one single experiment yields the permittivity as well as the imagery. In Chapter 12, experimental case studies are conducted to show how data is collected and processed, and how images are formed. In Chapter 13, cross-correlation technique is applied between the positive looking and the negative looking images to estimate refractive index. Also, algorithms from Part I and Part II are combined together to investigate the experimental data. The outcome further proves the usefulness of the algorithms. Finally, in Chapter 14, conclusions are drawn.

CHAPTER 9 BASIC ISSUES REGARDING SAR IMAGING

9.1 Point Target Model and SFCW Monostatic Mode

The purpose of this chapter is to address some basic issues regarding SAR imaging, many of which implicitly or explicitly underlie the material covered in the later chapters.

9.1.1 Point Target Model

Point target model [47, 48] is widely used to represent targets in radar imaging, together with some other models such as the *Bragg Model* [48, 49]. In the point target model, the targets are described to behave as a series of discrete, uncoupled, broadband, and isotropically radiating points regardless of the aspect angle. In addition, we further assume that the EM waves do not experience phase change upon scattering from point targets.

Of course, these assumptions do not always satisfy in real life ¹. Careful interpretation of the resultant images is called for to acquire a good understanding about the targets as the images do not visually resemble the geometrical shapes of the objects. The reason that microwave images are not the same as optical ones is [51]: the former are dominated by strong reflections from edges, corners and flat faces which are hit broadside from the radar direction (specular reflection). Smooth surfaces that are curved or tilted with respect to the radar are often transparent and show little on the image. With SAR algorithms, a target of a line segment is by no means equivalent to the superposition of a great number of point targets.

¹Recommendations are made for target models which, the author claimed, “nearly approach the real world” in [50].

9.1.2 SFCW Mode

In our research the stepped frequency continuous wave (SFCW) radar is used rather than the impulse radar. The stepped-frequency waveform is a discrete implementation of the linear FM waveform [52]. The choice of SFCW mode of operation is not only because it conforms with our microwave network analyzer, but also because it has certain advantages over pulse radar [53]: In our research the object is located close to the radar antenna, about 200 – 500 mm. In order to have good down-range resolution², that is, to be able to discriminate small range differences among targets, at such short distances, the pulse radar must have extremely high precision in the time domain. e.g., on the order of 10^{-12} seconds. This puts a rather high demand, if not an impossible one, on radar system design as well as system cost.

On the other hand, the achievable down-range resolution depends on the signal bandwidth and is independent of the particular waveform. The commonly adopted criterion is

$$\text{Down-range resolution} \equiv \frac{v}{2 \times \text{BW}} \quad (9.1)$$

where, BW is the bandwidth of the transmitted signal. v is the velocity of propagation of EM propagation, i.e.,

$$v = \frac{c}{\sqrt{\epsilon_r}}$$

with c being the free-space speed of light and ϵ_r is the relative permittivity of the transmission media. Since ϵ_r for dielectric materials is larger than unity, the down-range resolution is reduced (improved) when imaging targets in materials with large ϵ_r . Therefore, as long as we have wide enough bandwidth we can achieve the desired down-range resolution.

²Resolution is different from accuracy, but together they constitute the precision of the measurement process, which decides the resultant image. The former is the ability to distinguish closely spaced objects, the latter is the ability to provide an unbiased estimate of the absolute range. It was pointed out recently in [54] that the conventional definition, which the author calls *nominal resolution*, is not accurate enough. The *functional resolution* was defined instead, which uses phase information and allows one to measure the scatterer positions with good accuracy.

9.1.3 Monostatic Mode

Figure 9.1 shows the geometry of both monostatic mode and bistatic mode. In monostatic mode, the transmitter and the receiver are placed at the same position (collocated). Normally, the same antenna is used both as a transmitter and a receiver. In bistatic mode, on the other hand, the transmitter and the receiver are separately placed at different positions. Here, we restrict that the transmitter does not move during measurement. In Fig. 9.1, the phase difference between signals received by Receiver b is $\frac{2\Delta d}{\lambda}2\pi$ for monostatic mode, while that for bistatic mode is $\frac{\Delta d}{\lambda}2\pi$. Thus, the former is twice as large as the latter. Because resolution is directly related to observed phase differences, the resolution performance is doubled for the monostatic mode. Thus, this type of mode is equivalent to halving the wavelength used for bistatic mode [55]. However, as point target model does not always represent the true story, we may miss a target with monostatic mode which, otherwise, may give rise to a large response with bistatic mode. An example of this situation is depicted in Fig. 9.2, where, because the target is tilted with respect to the broadside of the antenna beam, the specular reflection is toward a different direction and is not received by the receiver in the monostatic mode. In our research, the monostatic mode is adopted.

9.2 Focusing Techniques

9.2.1 SAR Technique

SAR technique can be interpreted using a combination of concepts from many disciplines [56]: (1) **Radar**: pulse echo, Doppler, and strip map system. (2) **Optics**: wavefront reconstruction, zone plate lenses, and holography. (3) **Communications theory**: sampling criteria and coherent reception. (4) **Antenna theory**: resolution, propagation, and delay-add. (5) **Linear system theory**: convolution, Fourier techniques, and shift-variant operations.

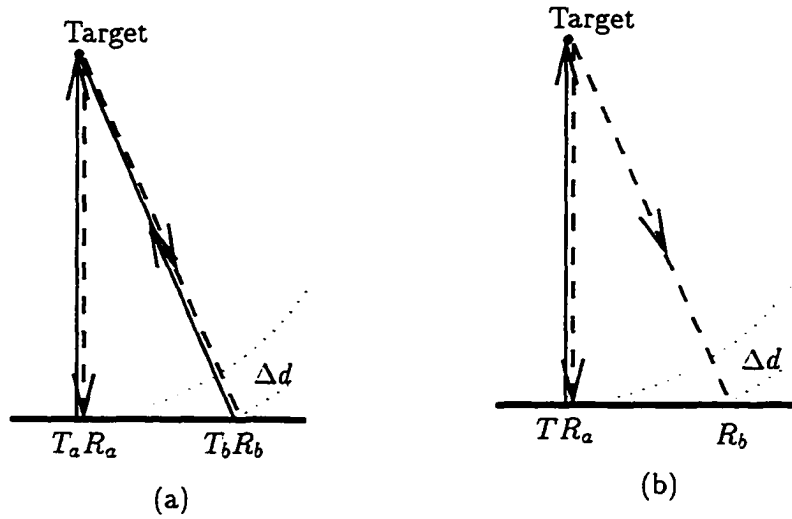


Figure 9.1 Different scanning modes: (a) monostatic mode, and (b) bistatic mode.

An antenna of dimension D at wavelength λ , and at range R , will produce a footprint of approximate width w

$$w \approx \frac{\lambda R}{D} \quad (9.2)$$

In fact, the footprint of the radar signal does not suddenly disappear outside of this region but fades quickly. The width w defined above specifies the size where the power of the footprint is $2/\pi$ of the maximum power, called the *Rayleigh's* resolution. Another definition is based on half power of the maximum called 3 dB level resolution.

If the focusing system is shift invariant, resolution of two adjacent object points lying in a plane normal to the line-of-sight can be expected if their separation is greater than the spot dimension by Rayleigh resolution criterion. It is seen from (9.2) that for the same wavelength λ and the same aperture dimension D , the farther away the targets are, the poorer resolution we obtain; putting it in another way, for the same wavelength λ and the same range distance R , to achieve better resolution larger aperture dimension is required. This is difficult to realize in many situations. The synthetic aperture concept was conceived such that it can handle this resolution dilemma without physically using

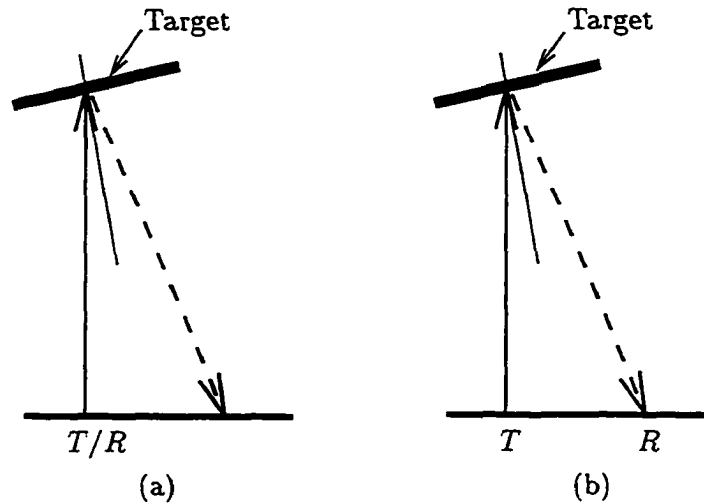


Figure 9.2 Different modes produce different results: (a) little signal is received in the monostatic mode, and (b) strong signal is received in the bistatic mode.

antennas of impractical dimensions.

Figure 9.3 shows a synthetic aperture of length L , which is usually a lot larger than the real antenna dimension, D . During the movement of the antenna, the target in the figure is always illuminated between antenna positions x_m and x_n . The corresponding cross-range resolution can be derived as [57]

$$\rho_{\text{SAR}} \approx \frac{D}{2} \quad (9.3)$$

It should be emphasized that this resolution can be realized only when the radar scatterers comprising the target have substantially omnidirectional reflection polar diagrams [58]. Our point-target model satisfies this condition. In general, however, targets often have relatively narrow polar diagrams and it will be this which determines the resolution. The narrower the polar diagram, the poorer the degree to which the scatterer can be resolved.

Interestingly, the resolution now is (1) independent of range distance, and (2) directly proportional to D as against to inversely proportional to D as expressed in (9.2) for

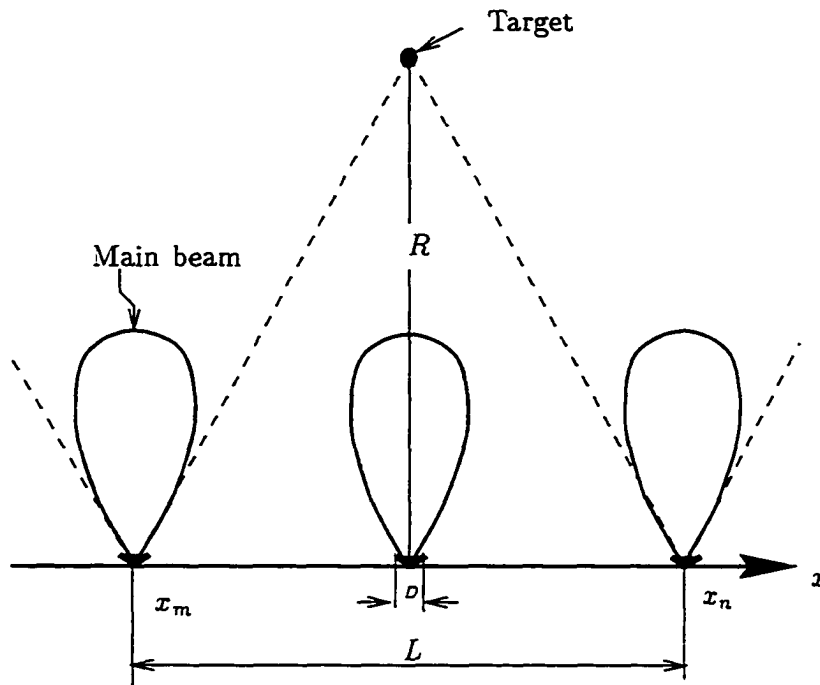


Figure 9.3 A target under illumination between positions x_m and x_n .

physical antennas. Also observed from the foregoing discussions is the fact that the down-range and cross-range resolutions are independent. The former is restricted by bandwidth of transmitted signal and the latter achieved through focusing synthetic array discussed in the next subsection. which allows the entire radar footprint width, i.e., the maximum length, to be used as the synthetic aperture length. Therefore, focused synthetic aperture can have a maximum length

$$L_{\max} = \frac{\lambda R}{D} \quad (9.4)$$

The result of the combined processes is a two dimensional image of the object formed in the radial (down-range) and normal to the radial (cross-range) directions.

9.2.2 Focusing Technique

The phase of the return signal from a given point target can be predicted, knowing this, the return signal can be phase corrected and a longer length of data from the point target can be used for signal processing. This is focused processing, or *focusing*. In other words, focusing generates a large antenna whose length is inversely proportional to the dimension of the physical antenna used to sample the array. A smaller antenna will result in a larger synthetic aperture.

This focusing is in fact the coherent signal summation, and it is the essential feature of the synthetic aperture formation; this requires that the signal be available in complex form. The required phase corrections are those necessary to force the summed signals to an in-phase condition. If a phase term equal to the argument of phase of the signal is subtracted from each signal prior to summation, the phase variations will be corrected and the summed signals will be in-phase. The result of the summation will be a maximum. The importance to have accurate signal phase is thus seen. For a point where no target exists, the phase corrected signal will not present a coherent pattern; hence, after summation over all antenna baseline positions and all temporal frequencies, the overall result will not be able to reach its maximum. This is also the basic conclusion of matched filtering technique discussed in the next section.

The phase factor includes both the phase inherent to the reflection coefficient and the phase associated with the two-way propagation delay. The former is not considered in our point target model, and the latter depends on the signal paths and its propagation speeds along the paths. Both of which are functions of material permittivity. Besides phase factor, the amplitude is another one, which is affected by the target property and its location. That is, the amplitude includes both the magnitude of the reflection coefficient and the spreading loss due to inverse square of the distance. The range profile is therefore a cell-by-cell sequence of the resultant magnitudes of the phaser sums of signals from all elements contained in the range resolution cells.

The focusing operation constitutes a significant computational burden. From what we see above, a distinct phase correction must be applied for each position, which constitutes one pixel in the final image. An image may contain up to thousands of pixels. The approach to this in the past relied on coherent optical processing [59], although it is now mostly replaced by electronic methods. In the next chapter, different algorithms are presented.

In reality, radar return signals are corrupted by noise which mainly affect the phase information. Some corrective methods may be needed before imaging process [60].

9.2.3 Matched Filtering Technique

Focusing, or coherent summation, discussed above leads to the process called the matched-filtering technique. The signals the radar receiver receives are always corrupted by noise. Hence the receiver must, somehow, be optimized. The matched filter receiver can be obtained based on the maximization of the signal-to-noise ratio for the simple problem of detecting a single target in stationary white Gaussian noise [61]. It was shown by Woodward [62] that this type of receiver also preserves all information in the radar return. The derivation of matched filters can be found in [47, 61, 62, 63]. The most important results are summarized below.

Assume that the received signal is $s(t)$, and its Fourier transform is $S(f)$. Then, the transfer function of the matched filter is

$$H(f) = S^*(f) \quad (9.5)$$

and the corresponding impulse response is

$$h(t) = s^*(-t) \quad (9.6)$$

where, $*$ denotes complex conjugation.

To see how we can extract distance information from the amplitude and phase of the received signals, we look at the electric field at the receiving antenna, which consists of

the sum of the reflections from each point target, namely [64],

$$E(f_n) = \sum_{m=1}^M E(m, f_n) \quad (9.7)$$

where

$$E(m, f_n) = \frac{E_0 \sqrt{\sigma_m}}{|r_m|^2} e^{i2k_n \cdot r_m} e^{-i2\pi f_n t} \quad (9.8)$$

and r_m is the distance to the m th target. E_0 is the amplitude of the transmitted electric field. σ_m is the radar cross-section of the target. k_n is the wavenumber in the medium of propagation corresponding to frequency f_n .

Now, selecting transfer functions $H(n, m)$ defined as

$$H(n, m) = e^{-i2k_n \cdot r_m} \quad (9.9)$$

The complex scattering coefficient $A(m)$ and target position can be determined by taking inner product, i.e.,

$$A(m) = \langle E, H(m) \rangle = \sum_{n=1}^N E(m, n) H(m, n) \quad (9.10)$$

As was stated earlier, the down-range resolution is determined by signal bandwidth rather than the pulse width. This actually is the result of matched filter processing. In other words, the width of the matched filter input τ_p would be the time resolution afforded without matched filter processing, while the time resolution with processing is $1/\text{BW}$. Thus, we see that matched filtering not only enhances detectability (accuracy) by maximizing receiver output SNR, but also decouples pulse length from range resolution. Therefore, long pulses of tolerable average power can be used to obtain large energy for satisfying the detectability requirements, while at the same time a wide bandwidth can be used to obtain good resolution. In fact, it is the important result that allows us to use SFCW mode in our studies.

9.3 Doppler Shift

At a given frequency f , when there is a change in distance between the transmitter and the receiver, the received signal frequency f' will no longer be the same as that of

the transmitter. This phenomenon is called the Doppler effect. The difference between the two, $f_d = f' - f$, is called the Doppler shift [65]. When the relative distance between the transmitter and the receiver is decreasing, the received frequency f' is higher than f , leading to $f_d > 0$, and vice versa.

Doppler effect is not only used to measure target motion, it is also the basic physical effect used in synthetic aperture imaging radars to achieve very high resolution. However, in our stop-and-go mode of measurement Doppler shift does not exist in the strict sense. In the following discussion we will see that it is the geometry change in the experiment that results in cross-range resolution. This phenomenon will be brought into full play when the estimation of dielectric permittivities is studied.

9.3.1 Stop-and-Go Mode

Imaging methods can be divided into two major categories according to the process employed: in-place imaging and object-motion imaging. In the first method, the image is derived from observation of the object held in a fixed position relative to the observer; the resulting image is derived from and can be uniquely associated with a particular object orientation. In the second method, the imaging process requires relative motion between object and imaging system; in some cases, the resulting image is derived from and associated with a range of object orientations.

The scenario we are dealing with belongs to the first one. Specifically, in our setup the radar antenna is stepped in uniform linear increments and a series of static measurements is made of the phase and amplitude of the received signal. Provided that the Nyquist sampling criterion is met, a sequence of such measurements is identical to the phase history that would be observed with a continuous movement.

It was mentioned above that geometry we use is an equally-spaced stepsize along a reclinear baseline. This, however, is not an inherent restriction of the technique. The antenna positions may well be non-reclinear and unequally-spaced. In fact, spotlight SAR

is an example [66], which may result in even higher resolution.

It is important to point out that although there is no relative movement between targets and antenna during measurements, there is rich information in the return signal when investigated as a function of antenna locations. This will be elucidated more thoroughly in the following chapters.

9.4 Sampling Criteria

Our SAR data are functions of two basic discrete variables — the temporal frequency and the antenna location. Thus, the sampling rates in both the temporal-frequency-domain and the space-domain should be high enough to avoid aliasing.

9.4.1 Temporal-Frequency-Domain Sampling

In the context of our study, we have bandlimited signal. Therefore, the corresponding signal as a function of time extends to infinity. As time and distance has one-to-one correspondence, the distance thus extends to infinity, too. If frequency increment is Δf , then the period in distance is

$$\text{Period in distance } y_{\max} = \frac{c}{2\Delta f} \quad (9.11)$$

Considering the two-way propagation, this says that objects from beyond $y = y_{\max}/2$ will appear as if they were in the range $0 \leq y \leq y_{\max}/2$. To reduce the interference as much as possible, we should reduce Δf . However, for the same bandwidth small Δf means more data points and longer processing time. In practice, we have the prior knowledge that either beyond a certain point no objects exist or the reflections from objects beyond our imaging region are too weak to cause any major effect.

In our experimental setup, the maximum number of points in the 35 GHz bandwidth is 801, thus

$$\Delta f_{\min} = \frac{(110 - 75) \times 10^9}{800}$$

and

$$y_{\max} = \frac{c}{2\Delta f_{\min}} \approx 3429 \text{ mm} \quad (\text{one-way distance})$$

9.4.2 Space-Domain Sampling

When sampling space-domain data the same rule regarding Nyquist rate holds. The Nyquist rate here specifies the maximum distance between two samples in space for the given maximum spatial frequency bandwidth to avoid aliasing.

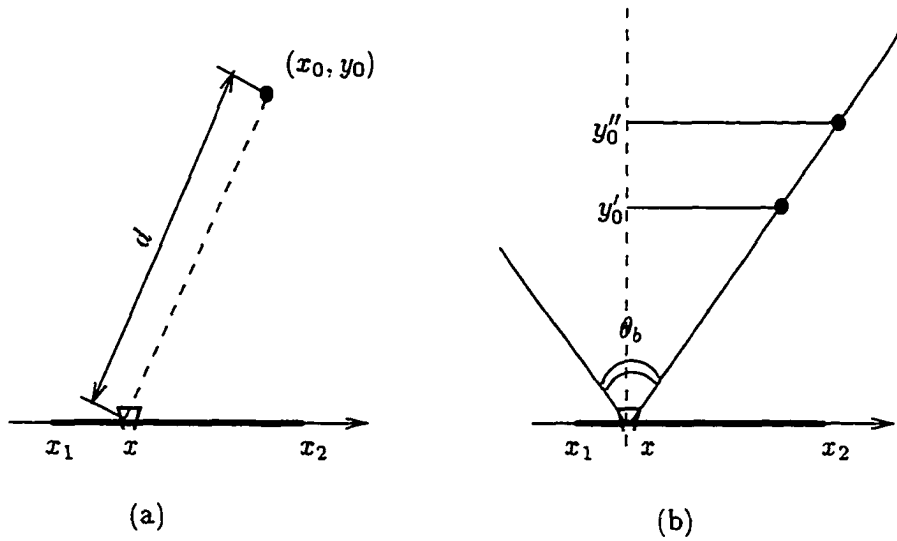


Figure 9.4 Geometry for deriving spatial frequencies.

Fig. 9.4(a) shows that the phase delay from x to the point target at (x_0, y_0) is

$$\text{Phase delay} = \frac{4\pi}{\lambda} \sqrt{y_0^2 + (x - x_0)^2} \quad (9.12)$$

Define spatial frequency f_x as [75]

$$f_x = \frac{d}{dx} (\text{Phase delay}) \quad (9.13)$$

or

$$f_x = \frac{2}{\lambda} \frac{x - x_0}{\sqrt{y_0^2 + (x - x_0)^2}} = \frac{2}{\lambda} \sin \theta \quad (9.14)$$

and

$$\omega_x = 2k \frac{x - x_0}{\sqrt{y_0^2 + (x - x_0)^2}} = 2k \sin \theta$$

where k is the wavenumber.

If $y_0 \geq y_{\min}$, where y_{\min} is some value smaller than which no targets present, then

$$\lim_{\substack{x \rightarrow \pm\infty \\ y_0 \geq y_{\min}}} f_x = \pm \frac{2}{\lambda} \quad (9.15)$$

Thus, it is bandlimited. Accordingly, the Nyquist frequency (or sometimes the folding frequency) [67] is $\frac{1}{2\Delta x}$, which has to satisfy

$$\frac{1}{2\Delta x} > \frac{2}{\lambda} \quad (9.16)$$

where Δx is the stepsize of the antenna movement.

Rewriting the above equation yields

$$\Delta x < \frac{\lambda}{4} \quad (9.17)$$

This claims that we are able to avoid aliasing as long as the antenna movement stepsize is less than a quarter of the wavelength. When working with a band of frequencies, the highest frequency (corresponding to the shortest wavelength) should be chosen for (9.17).

The above analysis is a little too pessimistic, though. It can be shown that the spatial frequencies are limited by the region of support in the $x - y$ plane. In Fig. 9.4(b) we see that if antenna sidelobes are neglected, there is a maximum beam width beyond which targets are not illuminated. Assume that the antenna's main beam spans an angle θ_b , we then get

$$\frac{x - x_0}{\sqrt{y_0^2 + (x - x_0)^2}} \leq \sin \frac{\theta_b}{2} \quad (9.18)$$

and

$$\max\{f_x\} = \frac{2}{\lambda} \sin \frac{\theta_b}{2} \quad (9.19)$$

so that the corresponding stepsize is now

$$\Delta x < \frac{\lambda}{4 \sin \frac{\theta_b}{2}} \quad (9.20)$$

This permits a larger stepsize Δx , nevertheless not at the risk of aliasing. A plot is shown in Fig. 9.5 to reveal the relationship between the normalized Δx with respect to the wavelength and the main beam stretching angle. Obviously, the larger the θ_b , the more restricted is Δx .

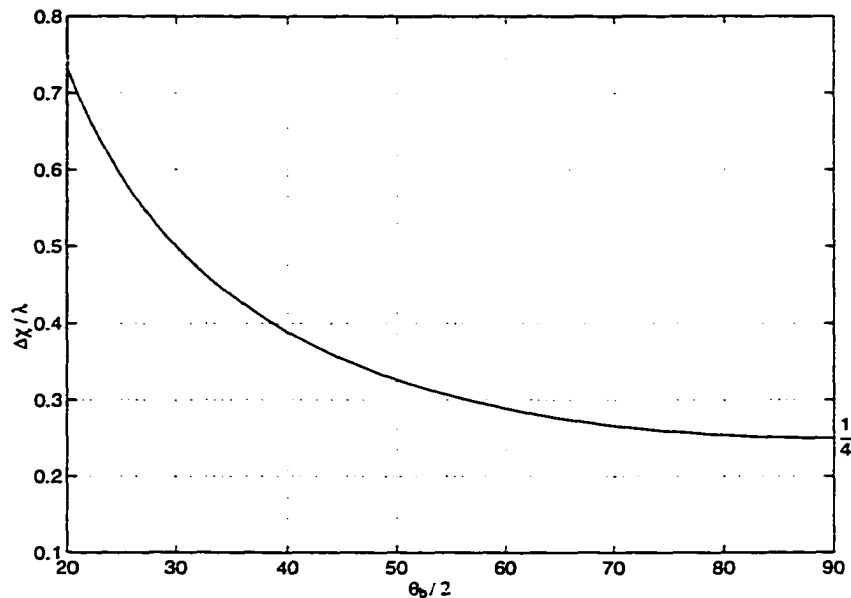


Figure 9.5 A curve showing the normalized stepsize reduces as θ_b increases.

9.4.3 Data Interpolation

The interpolation process is computationally expensive, but necessary. Because we are dealing with discrete data, the distance of a particular resolution cell may not correspond to the data points available. Rounding-off would be imprecise.

It is important to note that the nature of the complex data in our study is phaser rather than vector, although the two share the same mathematical forms. Therefore, The interpolation must be carried out with respect to the amplitude and the phase separately. In other words, it would be mistaken to interpolate with respect to the real part and the imaginary part, which is the scenario when dealing with a vector. This is seen in Fig. 9.6.

Suppose two data points d_1 and d_2 satisfy $d_1 = d_2^*$, two different results are obtained through different interpolation processes. Point A corresponds to the interpolation of phasers, while Point B to the interpolation of vectors. Obviously, the two results are not the same. Also important to note is that prior to the interpolation of phase, phase unwrapping [68] is required, although doing it locally is quite enough. Because the periodic nature of trigonometric functions, the phase we obtain is really its primary value restricted to within $[-\pi, \pi]$.

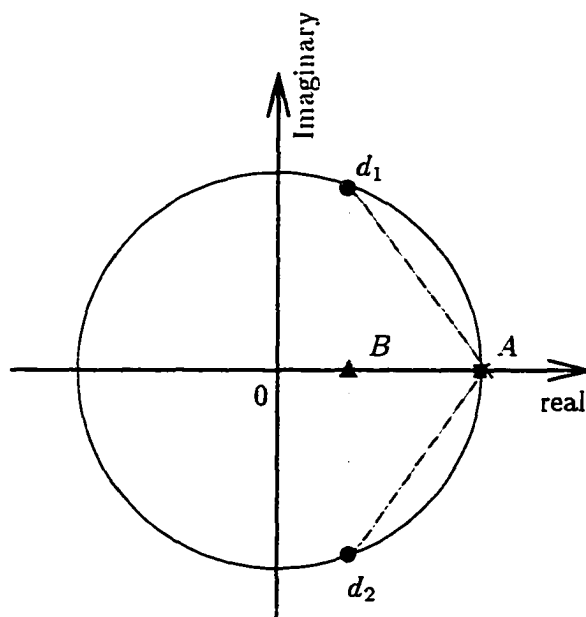


Figure 9.6 Two different ways of interpolation produces different results.

9.5 Sidelobe Suppression

To obtain high quality imagery, careful attention must be paid to sidelobes that are introduced in the storage process and the filter formation process.

One way of suppressing sidelobe levels is to use window techniques, which is analogous to slowly tapering off to zero the coefficient of Fourier series rather than using an abrupt truncation which results in Gibb's phenomena. Reference [69] provides a good descrip-

tion of different windows. The general rule is that although sidelobes can be suppressed through windowing, this is done invariably at the expense of mainlobe resolution. In [70] a class of nonlinear operators are presented, which significantly reduce sidelobe levels without degrading mainlobe resolution. Implementation is via sequential nonlinear operators applied to complex-valued SAR imagery.

9.6 Inflection Point Calculation

In SAR imaging process the distance the scattered EM wave travels from the target to the receiver is needed. This requires the knowledge of inflection points at boundaries for multi-layer media. There are various ways of calculating the inflection points, and they are summarized briefly below.

The geometry considered is shown in Fig. 9.7. Theoretically, the inflection point can be calculated by Snell's law. Unfortunately, the closed form solution for this simple problem does not exist to the best of our knowledge. Hence, different numerical methods have been developed to find the inflection points.

- **Bending Method:** In this method an inflection point is guessed, and the satisfaction of Snell's law is checked. The guessed point will be accepted if Snell's law is conditionally met; otherwise, a new guess about the inflection point will be made following the very same process.
- **Shooting Method:** In this method the path of ray is assumed, which crosses the boundary at a certain point. Starting from this point and following Snell's law, the ray in the second medium may or may not hit the target. The former gives the correct inflection point, and the latter requires a change of the ray path from the antenna and the process continues. The name of the method is from the idea that each time the initial launch direction is adjusted until a hit at the target is achieved.
- **Minimization Method:** In this method the inflection point is so decided as to minimize the total travel time for the ray. (Note, the minimization is not done to the path length.)

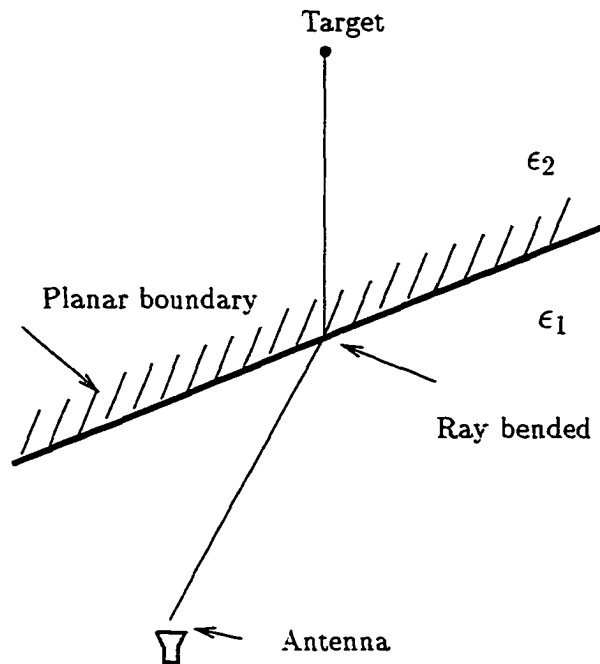


Figure 9.7 Ray bended at the boundary of two different media.

The minimization process can be carried out in different ways.

• **Approximation Method:** In [73] an *approximation method* is proposed. The basic idea is as follows. In Fig. 9.8 it is assumed that $\epsilon_{r2} \geq \epsilon_{r1}$. Two extreme cases are considered. If $\epsilon_{r2} = \epsilon_{r1}$, the inflection point is at a ; if $\epsilon_{r2} \gg \epsilon_{r1}$, the corresponding inflection point will be at b . It is then argued that the true inflection point must fall somewhere between a and b . An approximation method was suggested for the position of the inflection point as

$$\begin{cases} x_i = x_b + \sqrt{\frac{\epsilon_{r1}}{\epsilon_{r2}}}(x_a - x_b) \\ y_i = y_b + \sqrt{\frac{\epsilon_{r1}}{\epsilon_{r2}}}(y_a - y_b) \end{cases} \quad (9.21)$$

If (9.21) were accurate enough, it would save a lot of computational time. To this end, first, the result by the bending method [74] is compared with that by the minimization method. For both cases the results are almost identical. Next, the result of the approxi-

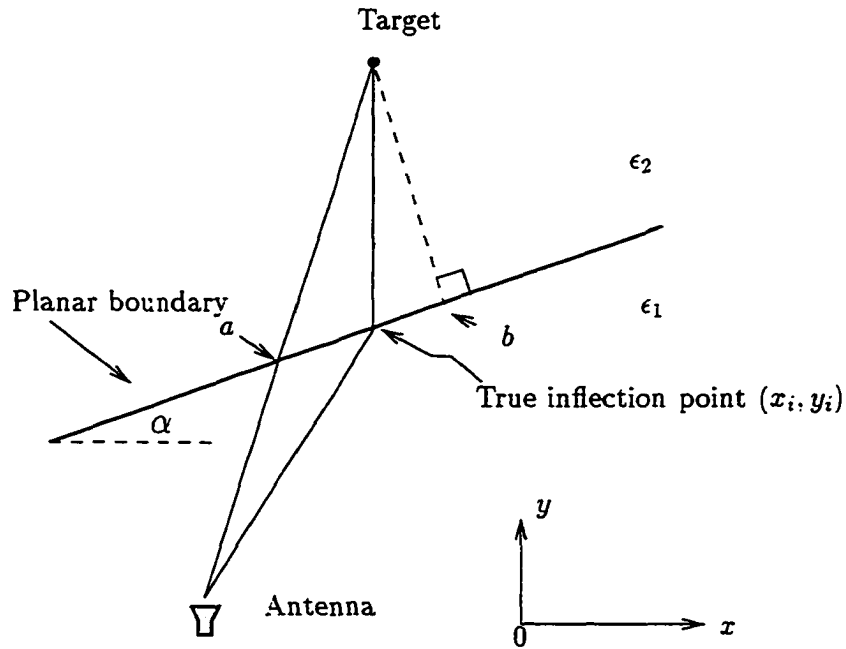


Figure 9.8 Two extreme paths and true path.

mation method is compared against that of the bending method. Details were presented in [22]. It is concluded there that the results of the approximation method are not satisfactory on the whole. It is seen that this method strongly depends on the geometry, and it can be expected that in some situations the result might be far away from truth, despite the claim in [73] that “ We have experimented extensively with this approximation; it is quite fast and it yields excellent result.”

In all the related algorithms where inflection point calculation is required, we use the bending method for its convenience in programming and relative quickness in convergence.

CHAPTER 10 SAR IMAGING OF OBJECTS IN HOMOGENEOUS MEDIUM

The simplest SAR imaging case is that objects and the antenna lie in the same homogeneous medium, usually in the air. The study of this also constitutes the foundation for the investigation of objects buried in one dielectric material while the antenna in the other. The geometry of our study is shown in Fig. 10.1. The antenna moves along its baseline from x_1 to x_{N_x} , going through N_x positions. At each position, the antenna transmits and receives signals at different frequencies, from f_1 to f_{N_f} , a total of N_f frequencies. Hence, when the measurement process finishes, $N_x \times N_f$ data points are recorded, each of them is a complex number. When expressed in matrix form it is

$$\begin{bmatrix} d_{11} & d_{12} & \cdots & d_{1N_f} \\ d_{21} & d_{22} & \cdots & d_{2N_f} \\ \vdots & \vdots & \ddots & \vdots \\ d_{N_x 1} & d_{N_x 2} & \cdots & d_{N_x N_f} \end{bmatrix} \quad (10.1)$$

where, $d_{mn} = d(x_m, f_n)$ $\{1 \leq m \leq N_x, \text{ and } 1 \leq n \leq N_f\}$ represents the data measured at the m th antenna position for the n th frequency. Thus, the data set contains information regarding both temporal-frequency-domain f and space-domain x . If we further define ϕ to represent the spatial-spectrum-domain and t the time-domain, the arrangement of x , ϕ , t and f produces four different combinations, namely, $f - x$, $t - x$, $f - \phi$, and $t - \phi$. However, only the first three provide nontrivial imaging methods. The reason that $t - \phi$ does not form a distinct method will be explained after the first three are elucidated. In

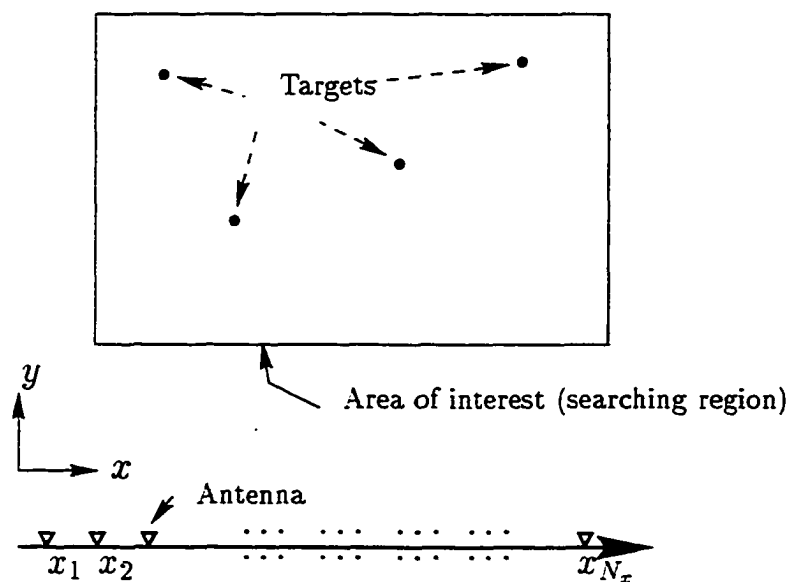


Figure 10.1 Geometry for SAR imaging when targets and antenna are in the same medium.

words, we have here three different approaches in forming an image, namely, the $f - x$ Method, the $t - x$ Method, and the $f - \phi$ Method. The other two approaches, $f - x - \phi$ Method and the $t - x - \theta$ Method will be discussed in Chapter 11.

10.1 $f - x$ Method

For $f - x$ Method we extend (9.10) to the data set defined in (10.1). The first step is to assume that a target existing at an image pixel located at (x_0, y_0) , which is within the searching region, and its distance to x_m is r_m , then the value we assign to this pixel is

$$A = \sum_{m=1}^{N_x} \sum_{n=1}^{N_f} d_{mn} H(m, n) \quad (10.2)$$

where, $H(m, n)$ is the transfer function defined in (9.9) and rewritten here again as

$$H(n, m) = e^{j2k_n \cdot r_m}$$

To analyze this algorithm in detail, we first consider the summation with respect to n , for some fixed m and (x_0, y_0) moving inside the searching region. That is, for each antenna position x_m , the matched filtering process is carried out in the f -domain. The image thus obtained consists of bands of arcs of different values.

Then, one more set of data at x_{m+1} is added, giving rise to another group of bands of arcs. This second image is superimposed upon the previous one and produces an improved image. Physically, what really happens here is that with each inclusion of a new data set, the image gets modified — values around pixels where targets exist are strengthened and at the rest of the pixels weakened or altered very little. This is due to the phase correction which the matched filter is supposed to perform. When we go through all possible N_x locations, we would get the final desired image.

10.2 $t - x$ Method

The $t - x$ Method processes data in t - and x -domain. The preprocess is required to transform the data in the form (10.1) into the following form through discrete Fourier transform performed column-wise on the matrix to produce,

$$\begin{bmatrix} d'_{11} & d'_{12} & \cdots & d'_{1N_t} \\ d'_{21} & d'_{22} & \cdots & d'_{2N_t} \\ \vdots & \vdots & \ddots & \vdots \\ d'_{N_x1} & d'_{N_x2} & \cdots & d'_{N_xN_t} \end{bmatrix}$$

where, $d'_{mn} = d'(x_m, t_n)$ $\{1 \leq m \leq N_x, \text{ and } 1 \leq n \leq N_t\}$ N_t is the number of data points in t -domain for any antenna position. N_t does not have to be the same as N_f . To save the burden of interpolation in our later calculations, we choose $N_t > N_f$. This can be easily achieved by using FFT and zero-padding to augment N_f to N_t by appending $N_t - N_f$ zeros.

The imaging process with the $t - x$ Method is summarized as follows:

- Step 1: Assume a target exists at a pixel designated by coordinates (x_0, y_0) , and its distances to different antenna locations can be calculated. (Whether this assumption is true does not really matter in that the imaging algorithm would do the job.)
- Step 2: Convert distances to the corresponding lapses in time.
- Step 3: Interpolate data with respect to time to get the value for each antenna position. (This depends on the value of N_t and the discretization step-size of the searching area.)
- Step 4: Add up N_x data point, each one corresponding to one antenna position, and obtain the value for the pixel.
- Step 5: Go back to Step 1 and move onto the next pixel.

The evolution of the image is basically the same as that with $f - x$ Method.

10.3 Recovering Observable Signals

10.3.1 Basic Concept

All signals implemented in practice can either be represented as a function of time $s(t)$ or as a function of frequency $S(f)$. These two representations are related through the *Fourier transform pair* [71]

$$s(t) = \int_{-\infty}^{\infty} S(f)e^{-i2\pi ft}df \quad (10.3)$$

$$S(f) = \int_{-\infty}^{\infty} s(t)e^{i2\pi ft}dt \quad (10.4)$$

It is customary to denote $s(t)$ as the signal or wave form and $S(f)$ as the frequency spectrum, although both representations can be called the signal.

The Fourier transform pair is valid without the assumption as which signal is real and which is complex. In real life we normally constrain $s(t)$ to be real. The spectrum of a real signal consists of positive and negative frequencies. Any spectrum not possessing this symmetry must necessarily belong to a signal which is either complex or purely imaginary. Thus, the complex conjugate of (10.4) is

$$S^*(f) = \int_{-\infty}^{\infty} s(t)e^{-i2\pi ft} df \quad (10.5)$$

As a result, we have

$$S^*(f) = S(-f) \quad (10.6)$$

This is an important property of a real signal. If we take the absolute value as

$$|S(-f)| = |S^*(f)| = |S(f)|$$

we observe that whatever shape the envelope has for positive frequencies, it is exactly reflected for negative frequencies. That is, one-half of the real signal spectrum uniquely specifies the signal.

We now remanipulate (10.4) by using (10.6) to get

$$\begin{aligned} s(t) &= \int_{-\infty}^{\infty} S(f)e^{-i2\pi ft} df = \int_0^{\infty} S(f)e^{-i2\pi ft} df + \int_{-\infty}^0 S(f)e^{-i2\pi ft} df \\ &= \int_0^{\infty} [S(f)e^{-i2\pi ft} + S^*(f)e^{i2\pi ft}] df = \text{Re} \left\{ \int_0^{\infty} 2S(f)e^{-i2\pi ft} df \right\} \end{aligned} \quad (10.7)$$

This tells us that when we transform the frequency signal, which is only defined for positive frequency, into time domain signal, and make sure that the latter is real, we only need to take the real part of the transformed data multiplying by some constant. Since it is valid to assume our SAR data to be real when viewed in time-domain, the real part of $\mathcal{F}^{-1}\{S(f)\}$ should really be used. The following simulation shows the necessity of this modification.

10.3.2 Simulation Examples

Based on the foregoing analysis we reconstruct a point target image using the $t - x$ Method. The temporal frequency bandwidth used is 35 GHz. The resultant images are shown in Fig. 10.2. Figure 10.2 (a) represents the image formed with complex data, and Fig. 10.2 (b) with real part of the data. For the sake of comparison we include two more images — one based on the imaginary part of the time-domain signal (Fig. 10.2(c)), and the other based on the magnitude of the time-domain signal (Fig. 10.2(d)). It is seen that both of them result in very distorted images. Among all the four choices the image formed by using the real part of the transformed signal shows the best resemblance to the original target.

A two point targets scenario is next simulated. The targets are separated in y direction by 5 mm. Since we know from the above analysis that the magnitude data and the imaginary part of the data do not work well, we only compare the results from the complex data with that from the real part of the data. In the former case the two targets cannot be told apart, while in latter case they are obviously distinguishable. The images are shown in Fig. 10.3.

10.4 $f - \phi$ Method

The $f - \phi$ Method deals with data in f - and ϕ - domain. The preprocess is required to transform the data in the form in (10.1) row-wise via FFT. The procedure for forming the corresponding image is described below.

- Step 1: Transform data in the x -domain into the ϕ -domain for each and every f .
- Step 2: Assume that there is a target at a pixel designated by coordinates (x_0, y_0) .
- Step 2: Calculate its spatial spectrum for all the frequencies.
- Step 3: Do matched filtering (correlation) on the data obtained in Step 1. Repeat this for every frequency, and add up the results.

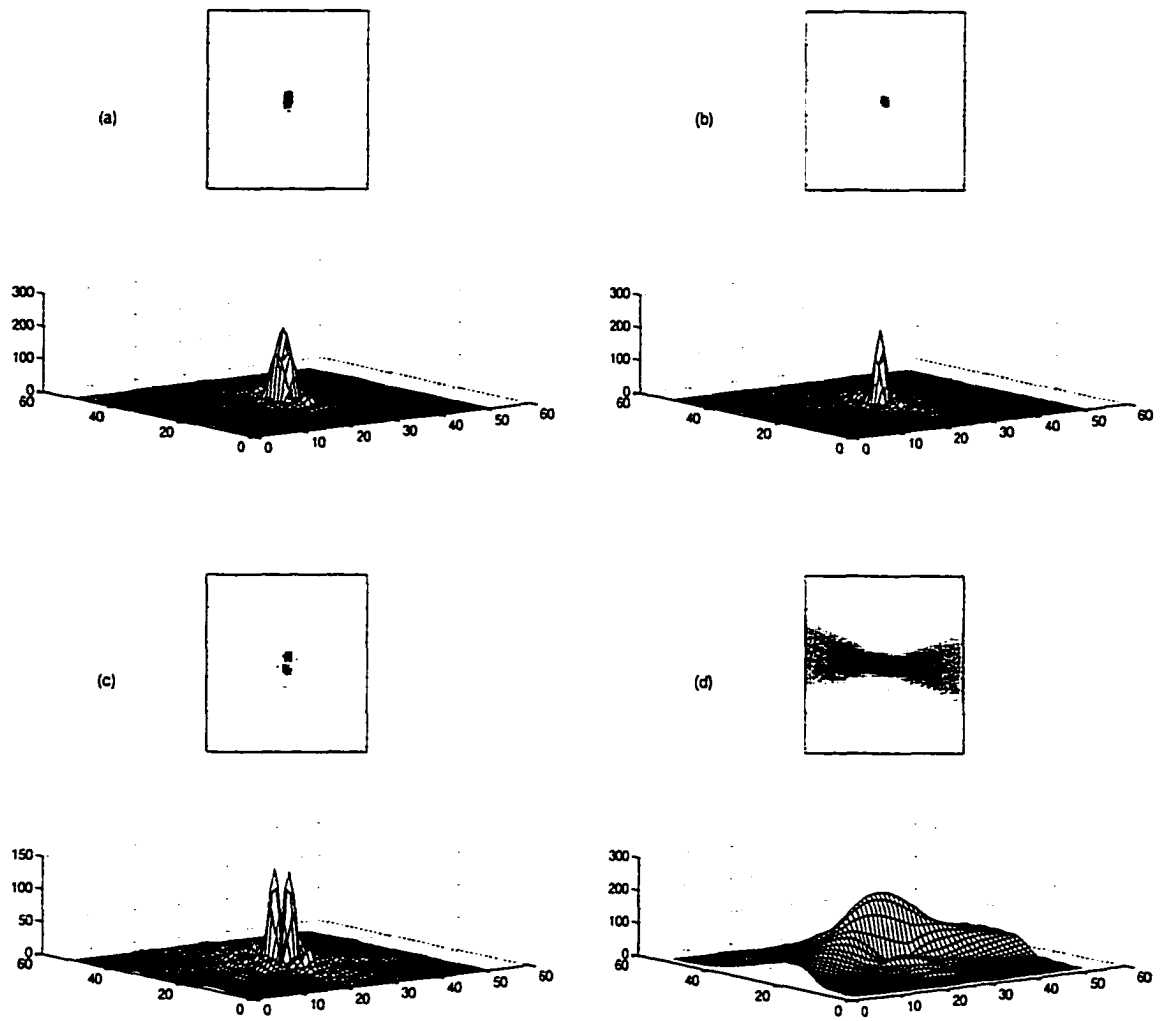


Figure 10.2 Images of one target formed by using different data attributes: (a) complex data, (b) real part of the data, (c) imaginary part of the data, and (d) magnitude of the data.

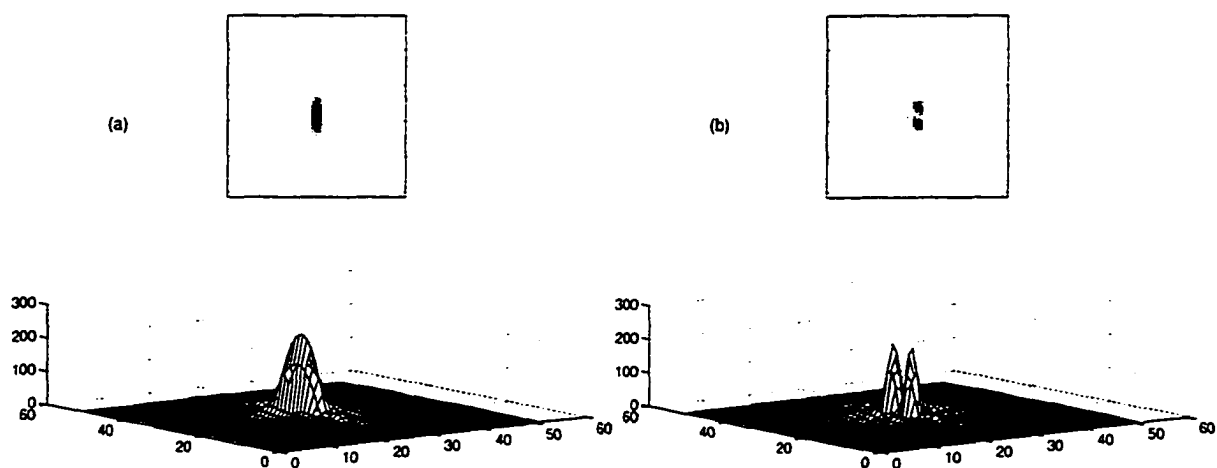


Figure 10.3 Images of two targets formed by using different data attributes:
(a) complex data, and (b) real part of the data.

- Step 4: Go back to Step 2 and move onto the next pixel.

Now, an explanation is ready for the reason that the combination of t and ϕ does not form a distinct method unless it is a trivial one. First, one can always transform t -domain data into f -domain data and ϕ -domain data into x -domain data, and then resort to one of the three methods presented above. However, this is trivial in a sense that nothing new is created. Second, when this trivial case is excluded, the combination of t and ϕ contradicts with each other: In the t -domain the information for f is completely lost; ϕ -domain data, on the other hand, has inextricable link to f . It is concluded hence that the combination of t and ϕ does not form a distinct imaging method.

Through various simulations with different geometry and different distributions of targets, it is verified that all the three methods turn out virtually the same images. Therefore, these three imaging algorithms are equivalent in terms of the final imagery. Figure 10.4 show how an image looks like during the formation process. The parameters used are:

The target is at (60,300); the frequency range is 75 – 110 GHz; (a) through (f) correspond to antenna baselines of lengths 2, 8, 16, 32, 64, and 128 mm. The starting position is always at (1,0) along the x -axis.

10.5 Comparison of Different Methods

Since all the three methods are equivalent in terms of the final resultant imagery, we need to compare their behavior so that they can be selectively applied.

- $f - x$ Method

This method is the fundamental method in our analysis as our data collection is done in $f - x$ domain. Also, the concept of phase correction (matched filtering or correlation) is straightforward. The drawback is its long computation time, which is more salient when the searching region size is large or 3-D image is studied.

- $t - x$ Method

In the $f - x$ Method the distance between the antenna and the target is converted to the phase delay (modular 2π), while in the $t - x$ Method this distance information is converted to the time delay. This change greatly improves computational speed. At each antenna position only one FFT is needed to convert data as a function of frequency f into a function of time t ; this is done once for all regardless of the imaging size. Thus, comparing with the $f - x$ Method, the $t - x$ Method is magnitudes faster while providing the same resolution of the imagery.

- $f - \phi$ Method

This method is basically like the $f - x$ Method in terms of computation time. However, as we will see in later chapters, some physical phenomena become more obvious when looked at from the ϕ -domain. When the searching region contains multi-layer media this method is a little cumbersome in that an analytical expression does not exist to relate the spatial spectra to the geometry.

For most cases, we tend to use the $t - x$ Method. Nevertheless, the other two methods may also be used to bring certain features into surface when circumstances dictate.

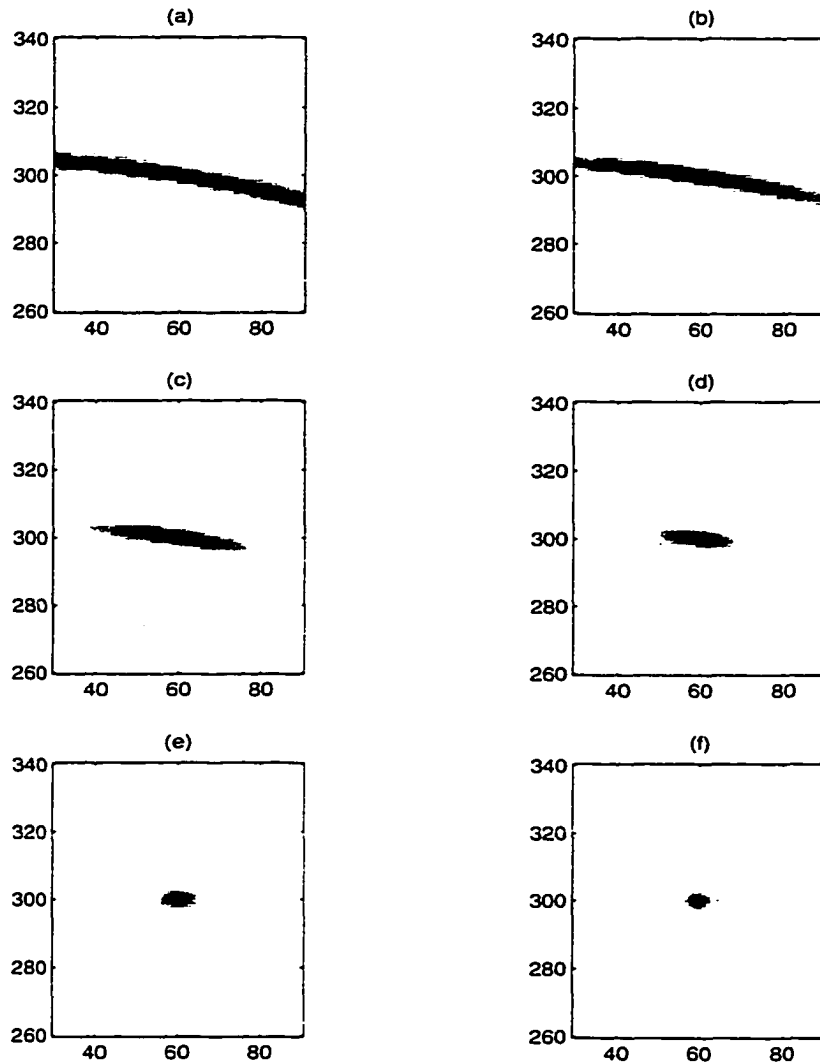


Figure 10.4 Evolution of an image when more antenna length is added.
(Description is in the text.)

CHAPTER 11 STFT AND $t - x - \theta$ METHOD

In this chapter short-time Fourier transform (STFT) is applied to link the spatial spectrum to antenna looking angles at different antenna positions. Although the “uncertainty principle” of signal processing indicates that good resolution can not be achieved simultaneously in both the space domain and the spatial-frequency domain, within this resolution we are able to improve SAR imaging algorithms by spatial/spatial-frequency analysis. As a particular example, when there exists only a single point target, the $t - x - \theta$ Method can be utilized to identify the target with super accuracy, even under the condition of zero temporal-frequency bandwidth.

Besides STFT other time-frequency methods have also been used in SAR imaging. In [76] the Wigner-Ville distribution is applied to deal with the situation when the lack of knowledge of the target motion does not allow a correct coherent processing, the useful energy spreads out over a wider region, thus causing a lower detection capability and a lower recognition capability. The proposed approach is based on a combined space-time and time-frequency processing. The space-time processing makes use of a linear array antenna and exploits the radar motion for filtering the receiver echos in order to improve as much as possible the signal-to-disturbance ratio. The signal is then mapped to the time-frequency domain, by computing its Wigner-Ville distribution, for a further filtering and for estimating its instantaneous frequency, necessary for the formation of a high resolution image of the moving object. In [77] a time-varying Hartley representation of radar signal was studied. The author argued that its advantage over STFT is that no complex operation is required, thus saving computer memory. We are going to use STFT

because its properties are by far the most widely studied.

A very promising method, the wavelet analysis, may turn out to be a good candidate for SAR imaging. This is because of its time-frequency and multiresolution properties. Some good sources on wavelet analysis in this regard are listed in the REFERENCES [78]-[84].

11.1 STFT Technique

The strength of Fourier analysis lies in its ability to decompose a signal into individual frequency components and establish the relative intensity among all the components. However, the information as to when those frequencies occurred is totally lost. This does no harm if the signal under study is stationary. Stationarity implies that the frequency content does not change with time. On the other hand, if the frequency contents of the signal change comparatively slowly, we may assume the signal to be quasi-stationary in a short period of time and Fourier analyze the signal within this period and compare the result with that within another period of time to find out the frequency content shifts between these two time periods. This is the basic concept behind STFT. Although there exists the inherent tradeoff between time and frequency resolution, the STFT and its variations remain the prime methods for the analysis of signals whose spectral content is varying [85]. The successful applications of STFT technique can be found in a wide scope of engineering branches [86, 87, 88, 89, 90, 91, 92, 93, 94, 95, 96].

11.1.1 Continuous Time STFT

If our interest lies at a particular time, t , we simply take a small portion of the signal centered around t and calculate its energy spectrum. This can be done for any time of interest. Formally, the STFT for the continuous signal $s(t)$ is defined as [97]

$$S_t(\omega) = \int e^{-j\omega t'} s(t') w(t' - t) dt' \quad (11.1)$$

where $w(t)$ is a window function centered at t . The energy density spectrum (*spectrogram*) is then defined as

$$P_s(t, \omega) = |S_t(\omega)|^2 \quad (11.2)$$

which can be considered as the energy density at t and ω . On the other hand, we may also think of STFT in terms of Fourier transform of the signal $S(\omega)$ and window $W(\omega)$, i.e.,

$$S_t(\omega) = \frac{1}{2\pi} e^{-j\omega t} \int e^{j\omega' t} S(\omega') W(\omega - \omega') d\omega' \quad (11.3)$$

which studies the behavior of the properties around the frequency point ω .

Physically, the window function is used to control the relative weight imposed on different parts of the signal. To assign larger weight to the portion of the signal around the point of interest allows us to estimate local quantities. Normally, the spectrogram is represented by a two-dimensional projection where the intensity is represented by different shades of gray.

From the behavior of window function and the Fourier transform property we readily see that the more compact we make the window in the time domain, the more time resolution is achieved. i.e.. the ambiguity in locating time is small. Similarly, if a narrow window is picked in the frequency domain, then high frequency resolution is obtained. However, because of the “uncertainty principle” [98, 99], both $w(t)$ and $W(\omega)$ can not be made arbitrarily narrow – there is an inherent tradeoff between time and frequency resolutions.

11.1.2 Discrete Time STFT

The discrete STFT can be extended from the above analysis [100]: Let $s(n)$ be a signal defined for all n , and let $S_n(e^{j\omega_k})$ be the STFT of $s(n)$ evaluated at time index n and frequency ω_k . The discrete STFT is then defined as

$$S_n(e^{j\omega_k}) = \sum_{m=-\infty}^{\infty} w(n-m)s(m)e^{-j\omega_k m} \quad (11.4)$$

which is the discrete equivalence of (11.1). In practice, (11.4) is realized through FFT.

11.2 $f - x - \phi$ Method and $t - x - \theta$ Method

With the tool of STFT we develop a new approach which we call the $t - x - \theta$ Method. Our SAR data is in the x - and f -domain. STFT is used to obtain the ϕ component for every given f for x -domain data. This $f - x - \phi$ Method already has all the advantages of the $t - x - \theta$ Method except that it is very time consuming. It was seen in Chapter 10 that the conversion of f -domain into t -domain information will speed up the imaging formation process. It was also mentioned there that because ϕ is closely dependent of temporal frequency, f , it is not possible to separate ϕ from f . However, as looking angle θ is solely a geometrical concept, if we can somehow use it as a parameter, the decoupling between ϕ and f will be realizable. The process of deriving the $t - x - \theta$ Method from the $f - x - \phi$ Method is as follows: For a given looking angle θ , at some x , we scan through the whole temporal frequency range. At each f the corresponding value of $\theta = \theta(f, \phi)$ is calculated. This is done for an interested range of looking angles. When this is finished, a final conversion using FFT is performed to change f into t . Thus obtaining the $t - x - \theta$ domain data.

The advantage of $t - x - \theta$ Method lies in its ability to approximately tell the origin of the signal in terms of arrival direction, even though physically the signal the antenna receives is the mixture of signals coming from all the directions within the antenna beam width and the time ranges. The latter is taken care of in the time-domain. The third domain, the x -domain, decides the location of the antenna when the signal is received.

The new data set, $D(t, x, \theta)$, being 3D, is very huge, thus requiring a large computer memory. However, corresponding to each θ only a narrow band of ϕ -domain signal (a subband) is used. Assuming that the original antenna movement stepsize is small enough

such that aliasing is of no problem, we now can down-sample the x -domain data to relieve the memory burden. This is shown in Fig. 11.1.

11.3 Single Target Identification With Zero Bandwidth

Although in our setup of SAR imaging there exists no relative motion between the targets and the antenna during measurement, the relative geometry between the targets and the antenna does change. This provides some meaningful two-dimensional information in ϕ - and x -domains. In Chapter 9 we derived the relationship between the target location and its spatial-frequency for some fixed temporal frequency. Here, we are going to further exploit this relationship for target identification under zero temporal-frequency bandwidth.

When a one-to-one correspondence is found between the spatial spectra and the antenna looking angles, the target coordinates can easily be obtained through simple geometrical calculation. In Fig. 11.2 STFT windows at x_1 and x_2 are shown together with the looking angles, θ_1 and θ_2 . A looking angle is defined to be the angle between the y -axis and the line connecting the antenna position to the target. Positive angle is formed if this line is to the right of the y -axis and negative angle is formed if this line is to the left of the y -axis. The target position (x_0, y_0) can be obtained geometrically in terms of $\theta_1, \theta_2, x_1,$ and x_2 as

$$\begin{cases} x_0 = \frac{x_2 \cos \theta_2 + x_1 \cos \theta_1}{\cos \theta_1 + \cos \theta_2} \\ y_0 = \frac{x_2 - x_1}{\tan \theta_1 + \tan \theta_2} \end{cases} \quad (11.5)$$

A simulation example is provided to show the use of $t - x - \theta$ Method to pinpoint a target. Suppose there is a target at $x_0 = 50$ mm, and $y_0 = 300$ mm. The antenna baseline is along the $y = 0$ axis with antenna going from -17.5 mm to 200 mm at a stepsize of 0.5 mm. The frequency used is chosen 100 GHz.

First, the signal relating to each antenna position is generated. The STFT is used for a

window size of 64 data points of Hamming type. 95% overlap of the windows is considered and 64-point FFT used. Thus, each FFT frame only includes 3 new samples. In fact, the overlap can be reduced depending on the antenna step size. A large overlap is chosen here because we would like to collect data points for analyzing the target coordinates statistically. The signal so generated is in the x -domain. We also Fourier transform it into spatial spectrum domain. Both of them are plotted in Fig. 11.3 together with the two-dimensional representation of signal content as functions of space and spatial spectrum obtained via STFT. The change of spectral content with respect to antenna positions is obvious. Second, simple ridge detection is applied to extract the peak for different locations in this $x - \phi$ 2-D representation. This is legitimate due to our prior assumption of the existence of a single target. The result is shown in Fig. 11.4. For the sake of easy comparison the theoretical relationship is plotted along. Third, ϕ is converted to θ based on (9.14). Last, (11.5) is used to calculate target coordinates as a function of window centers. The results are shown in Fig. 11.5. The mean and the variance of x_0 and y_0 are given in Table 11.1.

Table 11.1 Mean and Variance for x_0 and y_0

Coordinate (mm)	Mean (mm)	Variance	True value (mm)
x_0	49.95	0.027	50.0
y_0	299.91	1.124	300.0

It is seen that good accuracy in terms of target coordinates' mean and variance has been obtained under zero bandwidth condition. Obviously, the algorithm proposed here needs further study before being applied to multiple targets identification. However, the potential of its immediate application can not be ignored. For example, this algorithm can be used to identify a flying object in the sky or some dominant target under the water with little modification.

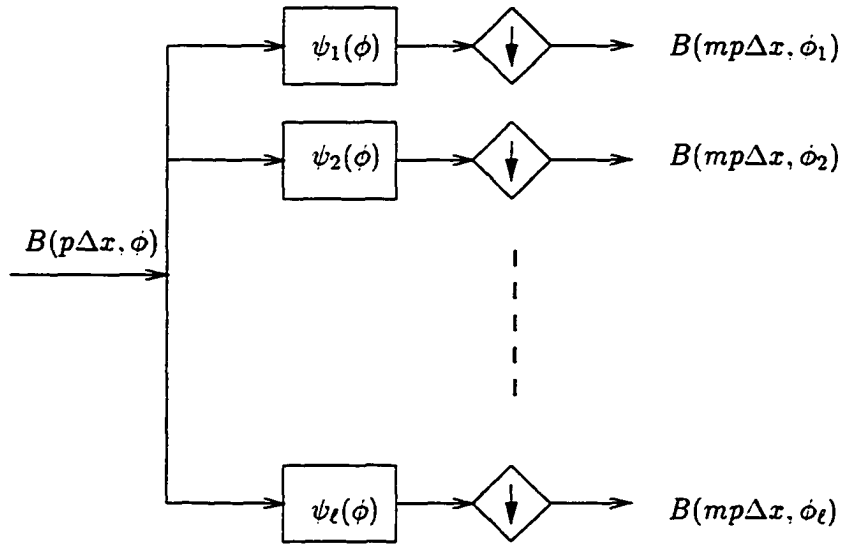


Figure 11.1 Filter banks and down-sampling by a factor of m .

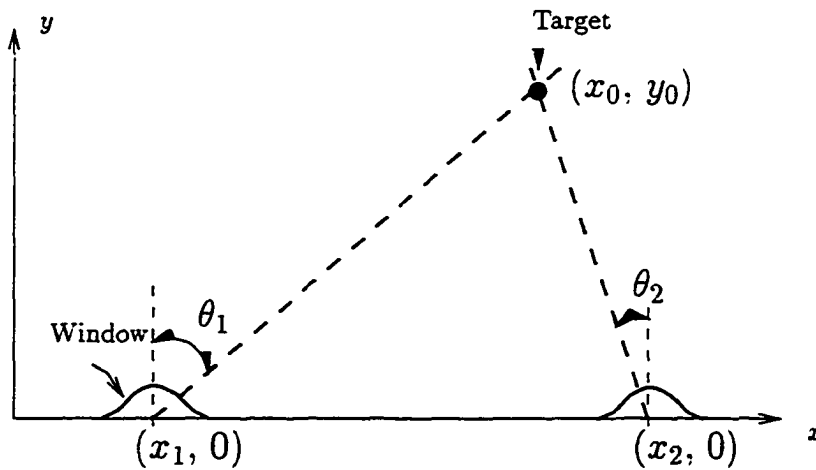


Figure 11.2 STFT windows and the corresponding looking angles.

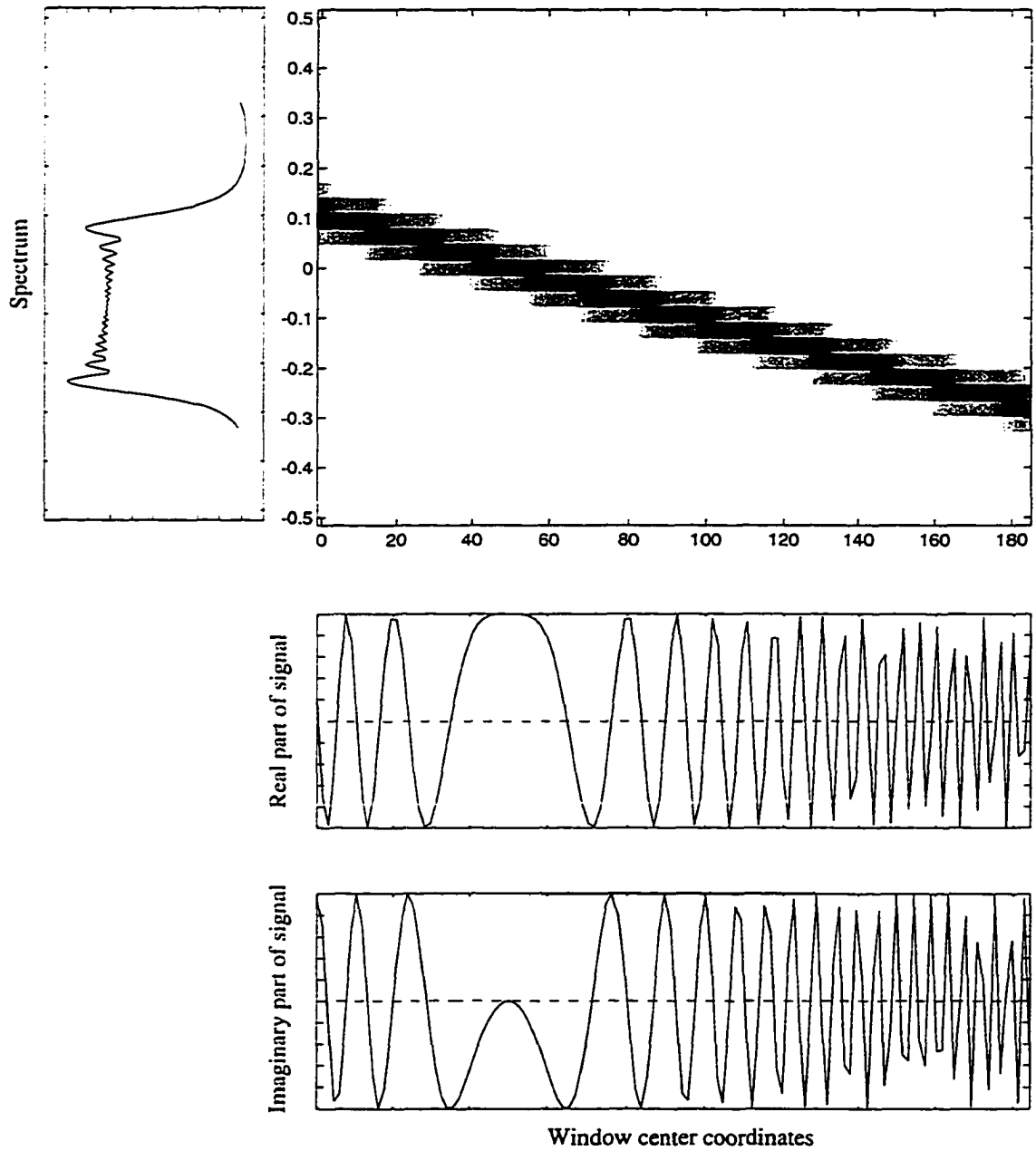


Figure 11.3 $x - \phi$ relationship for a single target case.

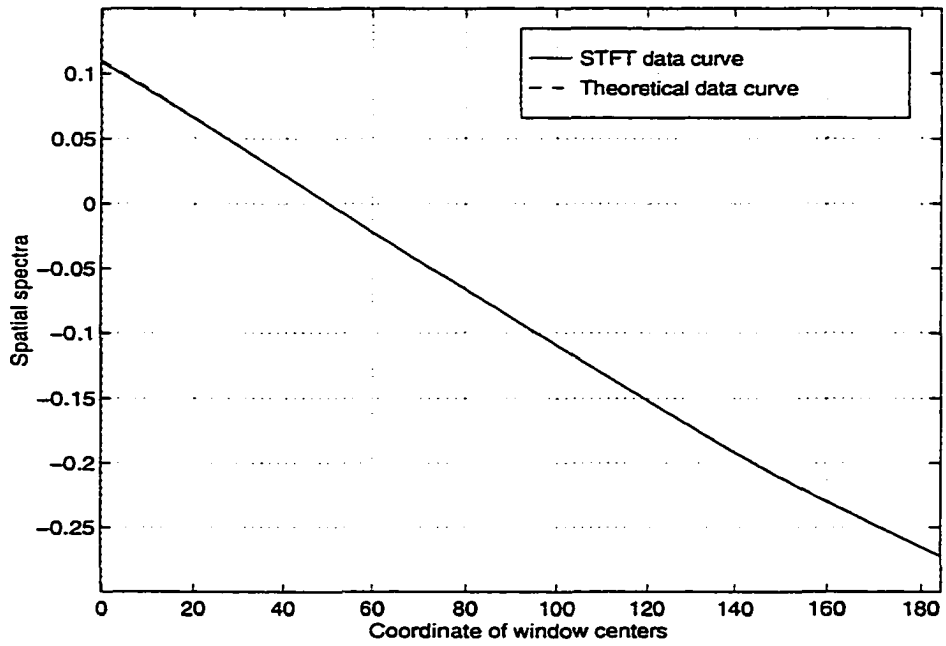


Figure 11.4 $x - \phi$ relationship after edge detection is performed.

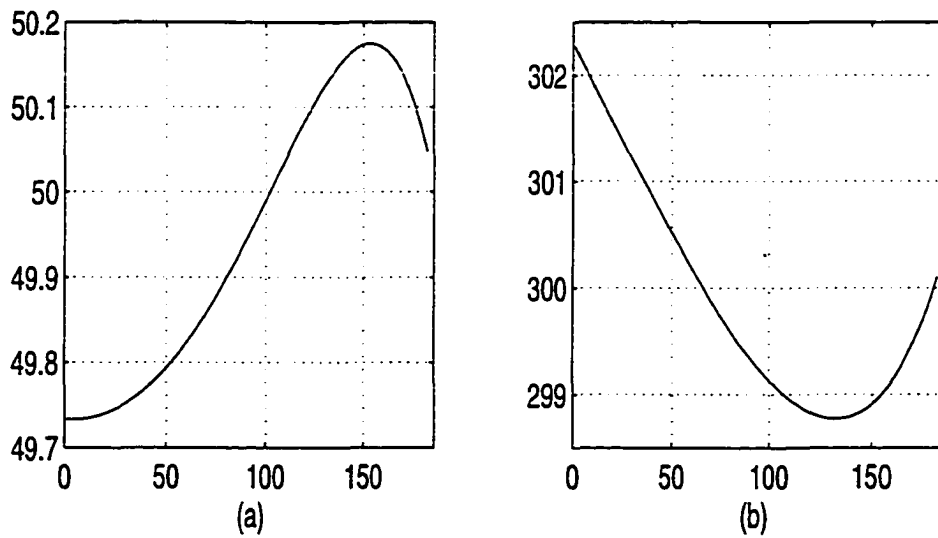


Figure 11.5 Target coordinates retrieved from different antenna locations:
(a) x -coordinates, and (b) y -coordinates.

CHAPTER 12 EXPERIMENTAL CASE STUDIES

The theory and the related algorithms for imaging buried objects inside dielectric materials have been validated by conducting experiments to obtain the images of objects attached both to the front and the back of a Plexiglas slab. Although the experimental setup represents the worst case possible in that the strongest specular reflection from the surfaces of the Plexiglas slab is received by the antenna, the resultant images formed thereby successfully demonstrate the effectiveness of the algorithms.

12.1 Background

One of the difficulties in imaging buried objects inside dielectric materials is the strong specular reflection, which, if not removed properly, will surely submerge signals from the targets. Thus a means is necessary to get rid of this uncalled-for part. We may choose to do this filtering in time domain. However, a little bit of careful thinking makes it a poor choice. This is so because a filter has certain width. When targets are located close to the interface such that the time difference for the EM wave to travel between the surface and the targets is not much larger than the filter width, it is impossible to remove the specular reflection part without harming the part from the targets significantly.

On the other hand, SAR is possible merely as a result of the system geometry without resort to the Doppler effect. It is pointed out in [101] the variation in phase from pulse to pulse is a consequence of the geometry of the imaging scenario, not necessarily of the difference in velocity between the antenna and the targets during pulse transmission and reception. This is exactly what is in our situation except that we use CW mode

instead the pulse mode. References [102] and [103] elucidated and successfully applied the concept that although no relative motion during measurement between the antenna and the sample, Fourier transform of the data as a function of antenna positions for each and every given temporal frequency into spatial-spectrum domain, the ϕ -domain does facilitate the analysis under certain circumstances. It is in this ϕ -domain that we found the specular reflection energy tends to concentrate in a very narrow region, while the spectrum of point-target signals scatter in a comparatively large span. A computer simulation is used to clarify this concept.

Suppose we have a half-space material with a certain refractive index n compared to n_0 of air. A point target is placed at the interface of the two media. If we assume that the signals due to the surface reflection and the point target can be separately obtained, we can then transform the corresponding signals for a given temporal frequency into the ϕ -domain normalized to $[-0.5, 0.5]$. If $d_0 = 300$, $f = 100$ GHz, $x_s = 1$ mm, $x_e = 256$ mm, and the point target is at (100, 300) mm, we obtain the spatial spectra for the two signals as shown Fig. 12.1 (a) and (b). The relative magnitudes are of no consequence here, and are therefore normalized to unity. While the spectrum of the surface reflection is spike-like, that of the point target spreads out, covering a much wider range. If a narrow band of it is destroyed, most of the information at other locations is still intact, allowing the formation of reliable imagery. The concept here is, in a sense, analogical to the *spread-spectrum technique* in communications [104]. The energy from the specular reflection is somewhat like the jamming noise there. The whole scheme is therefore jamming resistant.

12.2 Experimental Setup

Figure 12.2 shows the experimental setup for a SAR imaging system. Among the many experiments we conducted two are represented here. The only difference between the two experiments is that Experiment II has one more target, a metallic washer, added. The placement of the targets are shown in Fig. 12.3 (a) and (b), respectively. The Plexiglas slab

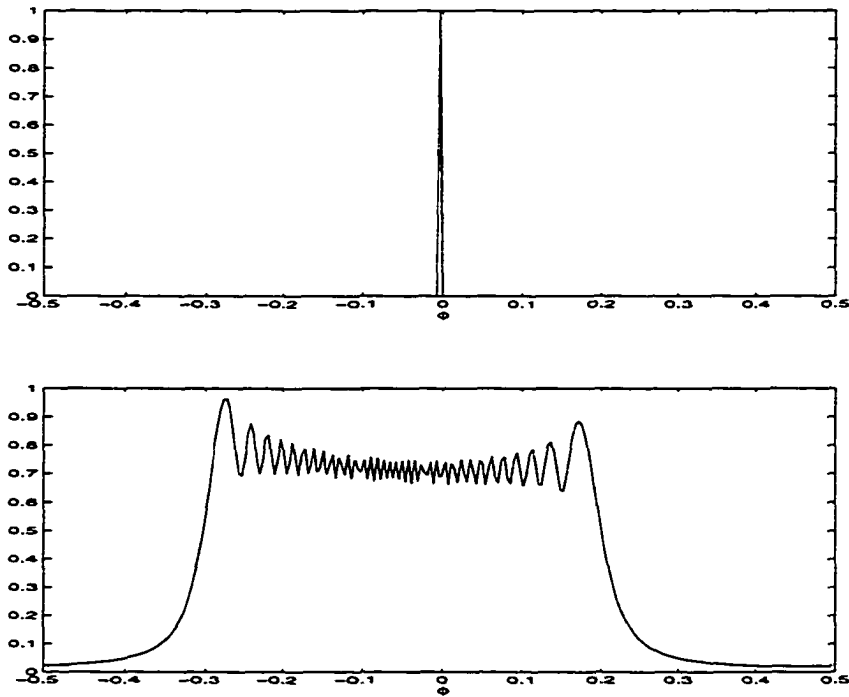


Figure 12.1 Spatial spectra: (top) specular reflection; (bottom) point-target scattering.

is mounted on a 3-D linear scanner controlled by a personal computer. Several metallic objects are attached to the front and the back surfaces of the slab to simulate imaging buried objects inside a dielectric slab. A single horn antenna (not seen in this figure) is positioned roughly 420 mm away from the front surface of the slab. The broadside of the antenna beam is so arranged as to make it perpendicular to the slab surface. This arrangement consequently yields the strongest specular reflection from the slab, which certainly tends to submerge the wanted image. The experiment is done basically as follows: At each antenna position, the network analyzer makes measurements by sweeping over the entire 75 – 110 GHz bandwidth in 801 discrete steps. Then the scanner, carrying the Plexiglas slab, moves a step by 1 mm in the direction parallel to the antenna baseline. This same process is repeated until the scanner reaches its end position. We chose a total of 128 steps, producing the data set of size 128×801 , occupying 3.4 Mb in ASCII file on UNIX.

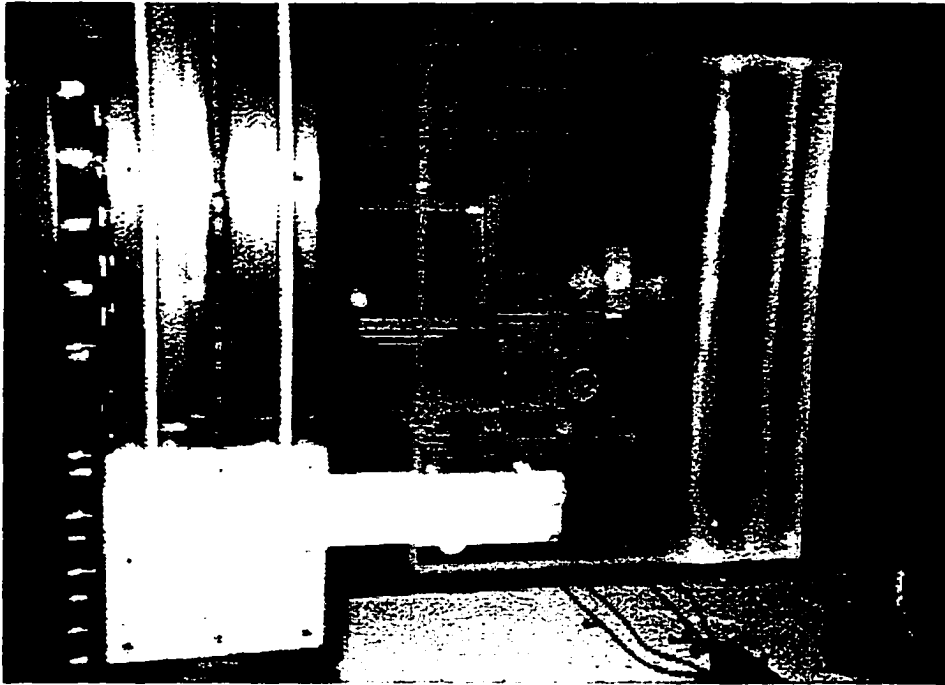


Figure 12.2 Experimental setup.

12.3 Data Preprocessing

When data set is obtained, pre-processing is necessary not only for better image but also for extracting rich information.

12.3.1 Specular Reflection Removal

Notch filter is first used to remove the specular reflection. In our setup the specular reflection sits at $\phi = 0$ as the antenna baseline and the slab surface are in parallel. Generally, the specular reflection could be either at $\phi < 0$ or at $\phi > 0$ depending on how the slab is tilted with respect to the antenna baseline orientation and whether the convention $e^{-j\omega t}$ or $e^{i\omega t}$ is chosen.

Figure 12.4 shows the spatial spectrum at all temporal frequencies, from 75 to 110 GHz. It is seen that a black narrow band at $\phi = 0$. We single out a particular frequency, $f = 95$ GHz, and show it in Fig. 12.5(a). Next, we choose a notch filter

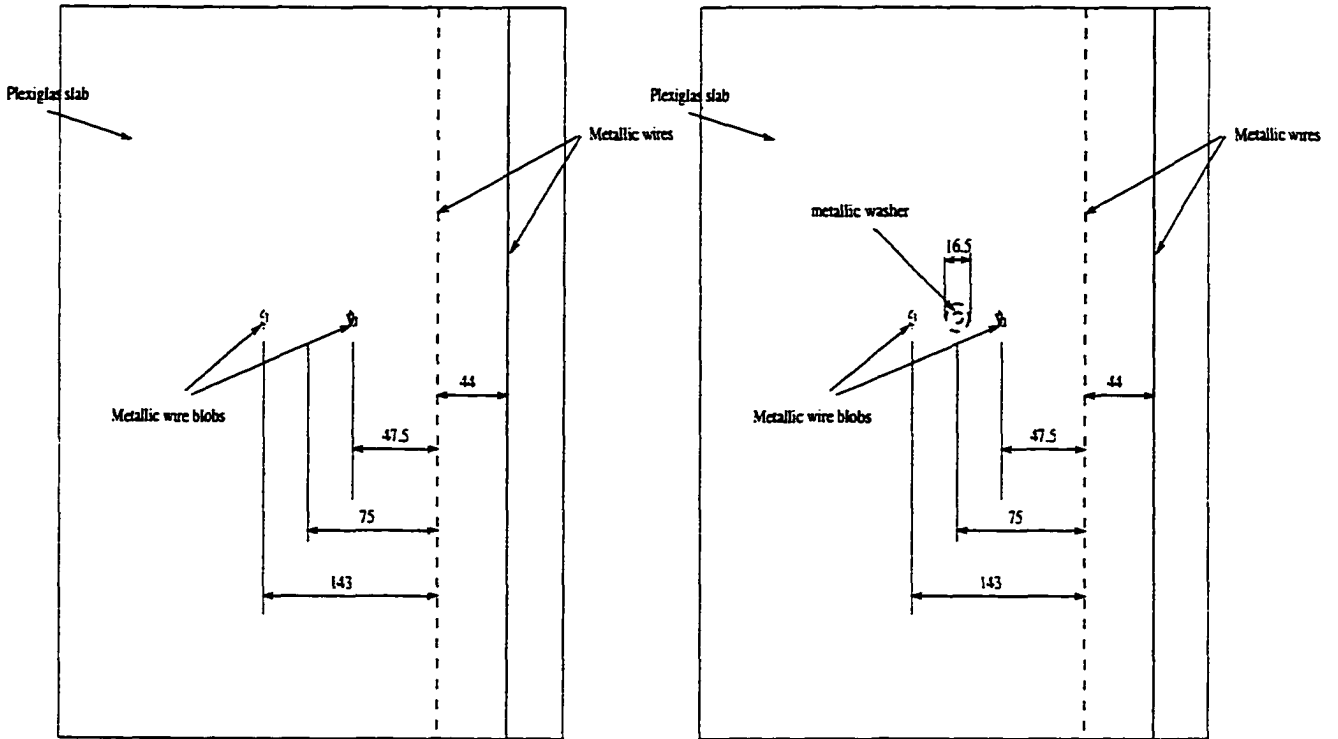


Figure 12.3 Targets arrangement on Plexiglas slab: (left) for Experiment I, and (right) for Experiment II.

$$F_{\text{notch}} = \left| \frac{m^2 - m_0^2}{(m - i\xi m_0)^2 - m_0^2} \right| \quad (12.1)$$

The parameter ξ is a small positive number used to control the width of the notch. This filter will remove a narrow region around some fiducial location $m_0 > 0$. Figure 12.6 shows the notch filter shape for different ξ values. We chose to be $m = [1 : 128]$, $m_0 = 65$, and $\xi = 0.05$. Fig. 12.5(b) is the same spectrum as in Fig. 12.5(a) after the notch filter with $\xi = 0.05$ has been applied. This filtering process is done for all the temporal frequencies.

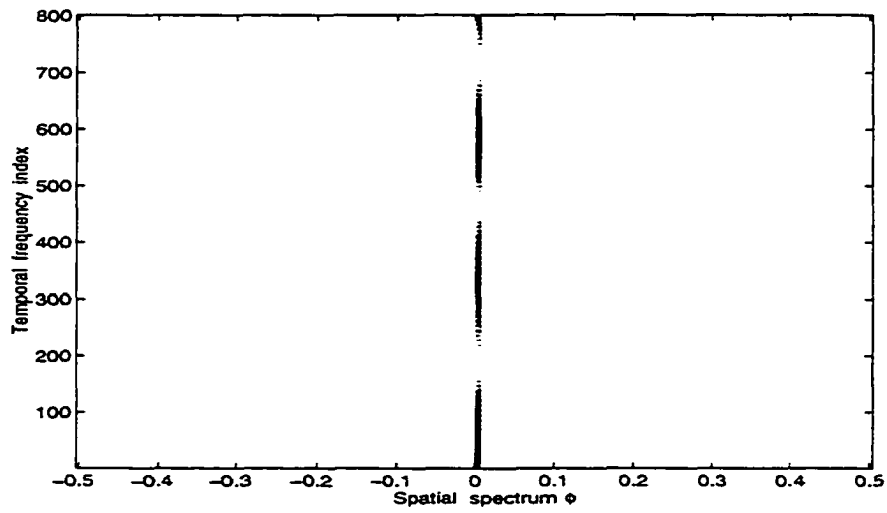


Figure 12.4 Spatial spectrum for all temporal frequencies.

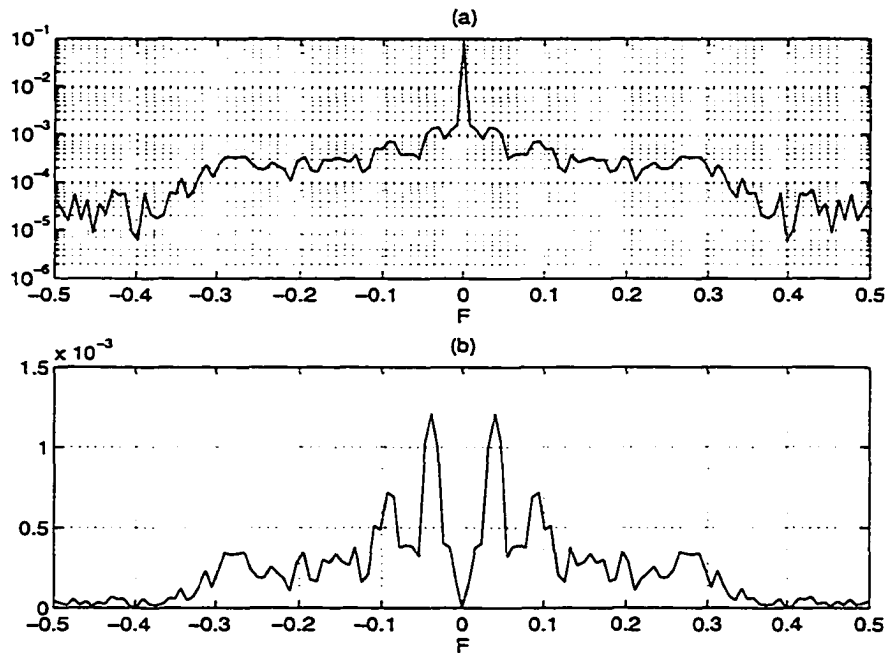


Figure 12.5 Spatial spectrum at 95 GHz: (a) before specular reflection is removed, and (b) after specular reflection is removed.

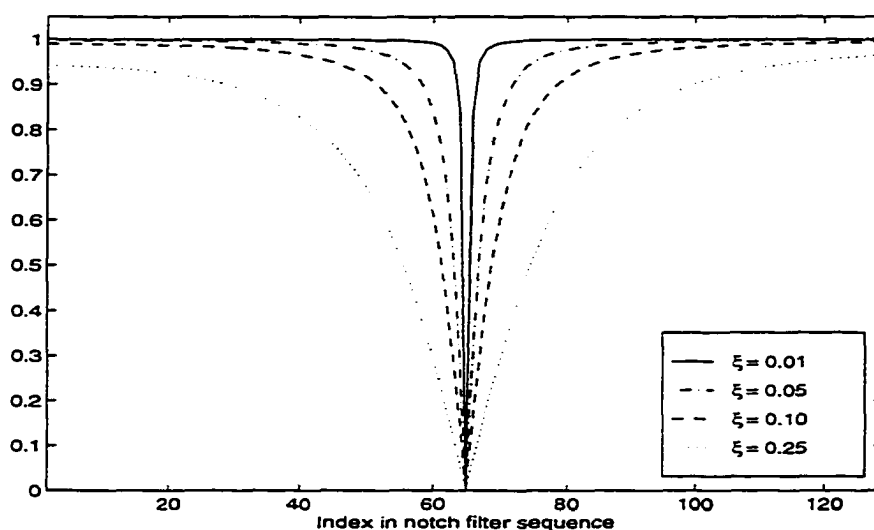


Figure 12.6 Notch filter shapes for different values of ξ .

12.3.2 Horn Antenna Mismatch Removal

Horn antenna mismatch causes multiple reflections in the horn producing strong signals. This is seen in Fig. 12.7 as dark strips close to $t = 0$. The strength of the signal due to horn mismatch can be evaluated at each antenna location. Fig. 12.8 shows the signal obtained at $x = -70$ mm. There are two strong peaks whose separation is about 12.5 mm and the distance from the father peak is about 21.5 mm. We sketch of the antenna horn with its dimensions in Fig. 12.9. We can approximately locate this portion of signal. For example, the farther peak corresponds to Plane *A* and the near peak Plane *B*. Furthermore, the horn reference point can be roughly estimated to be the intersection of horn sides, Point *C*. It is also noted that mismatch signal also appears at $\phi = 0$. Therefore, the notch filter used to remove the specular reflection also removes horn antenna mismatch implicitly. Thus, Fig. 12.8 becomes Fig. 12.10 after notch filtering. Although the experimental setup with antenna baseline parallel with dielectric slab interface produces the strongest specular reflection, the good trade-off is that the horn mismatch signal and the specular reflection signal can be eliminated all at once.

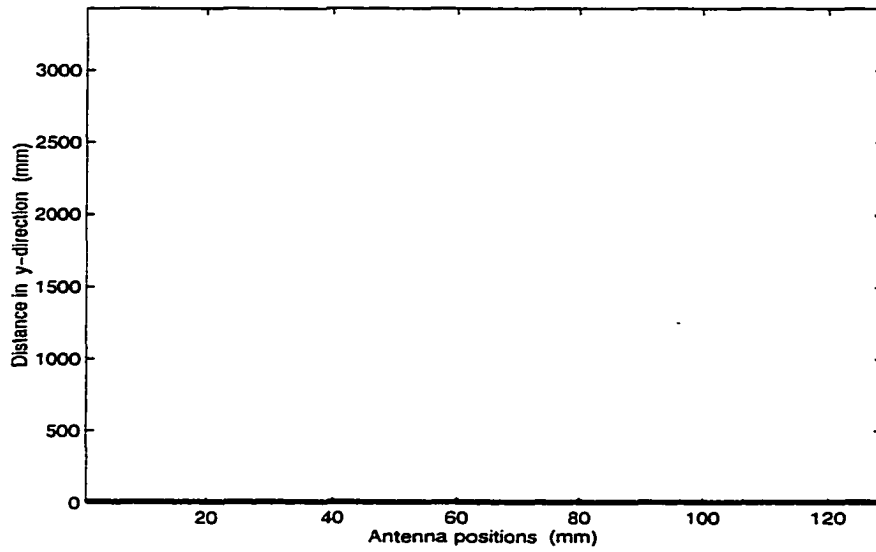


Figure 12.7 Distance domain image showing horn antenna mismatch which corresponds to the dark bands near the bottom.

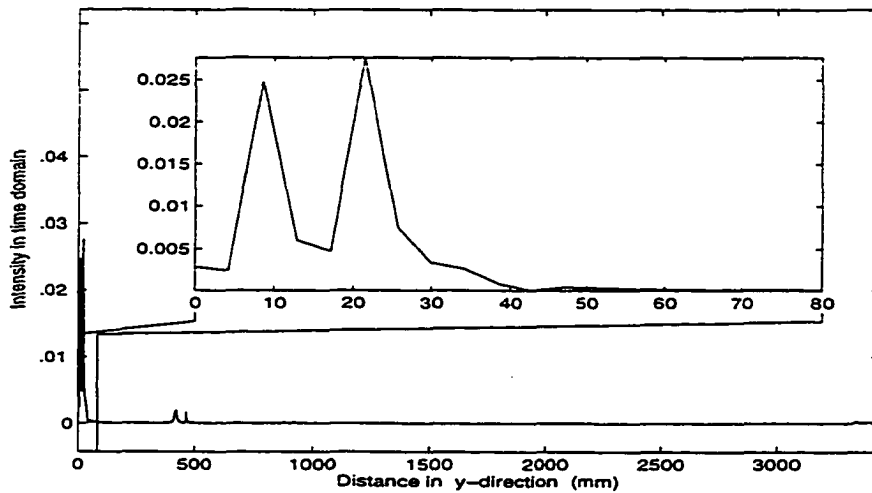


Figure 12.8 Signal part due to horn antenna mismatch ($x = -70$).

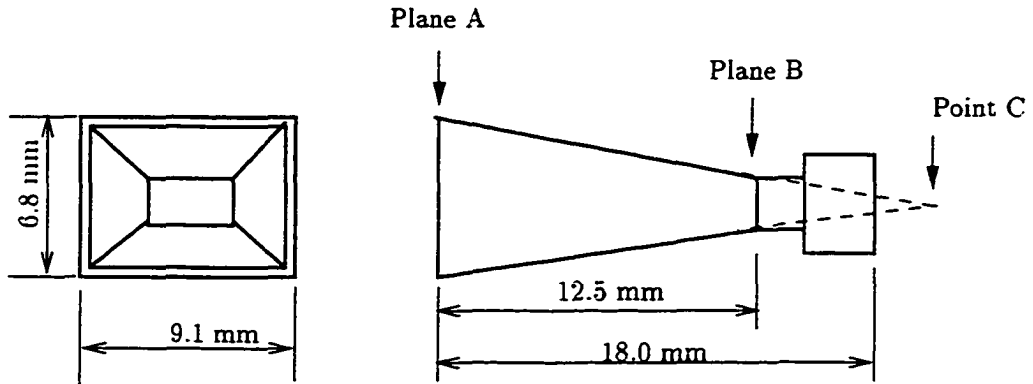


Figure 12.9 Dimensions of antenna horn used for experiment.

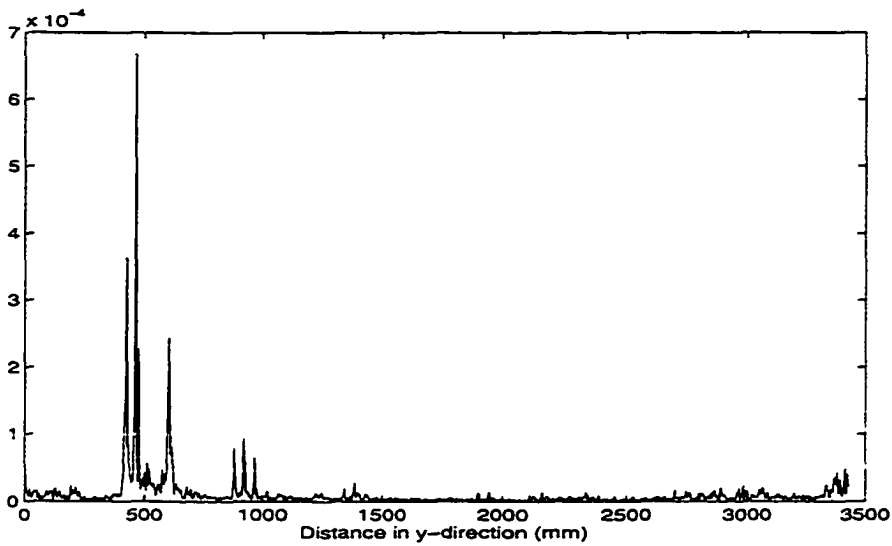


Figure 12.10 Signal part showing little antenna horn mismatch after specular reflection removal ($x = -70$).

12.3.3 Distance Determination

The distance between the slab front surface and the antenna is needed in forming the image because of the difference in refractive index before and after the interface. This parameter can quickly be calculated in distance (or time) domain. For example, in

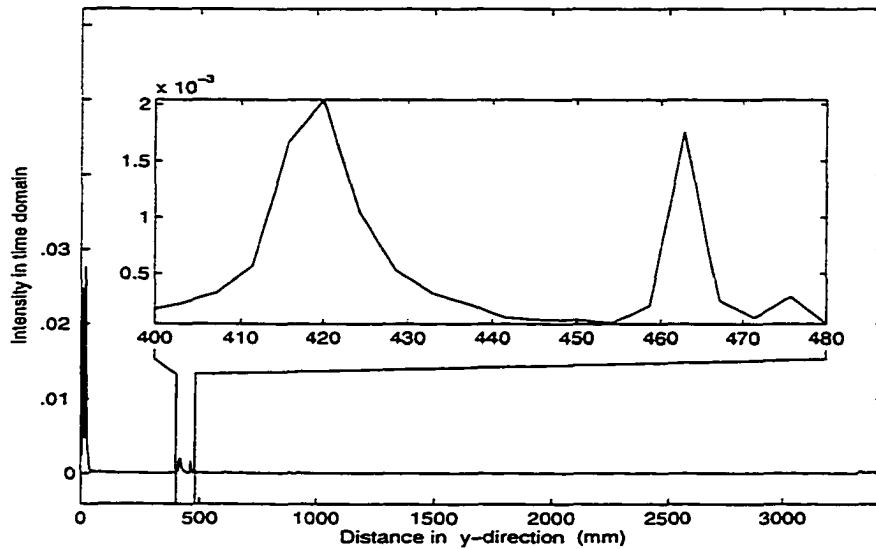


Figure 12.11 Signals due to interface specular reflections ($x = -70$).

Fig. 12.11 we plot the signal as a function of distance for antenna at $x = -70$ mm. We see that the front surface is approximately at 420 mm. This is further confirmed in Fig. 12.12 for four different antenna positions. In this figure, (a), (b), (c), and (d) correspond to $x = -70$, $x = -30$, $x = 10$, and $x = 50$ mm, respectively. The plots also prove that our assumption of the parallelism between the antenna baseline and the slab surface is valid.

12.3.4 Refractive Index Estimation Based On Distance Domain Signal

The distance domain signals can also be used to estimate the relative refractive index of the slab if the thickness is known. We again resort to Fig. 12.11. If we assume the two peaks correspond to the front and the back surfaces of the slab, the distance between the two peaks is obtained as $463.6 - 420 = 43.6$ mm. However, this distance is calculated with the hidden assumption that EM wave propagates at speed c . Since we do have the prior knowledge of the thickness of the Plexiglas slab, which is 27.3 mm, we estimate the relative refractive index readily as

$$n = \frac{43.6}{27.3} \approx 1.597$$

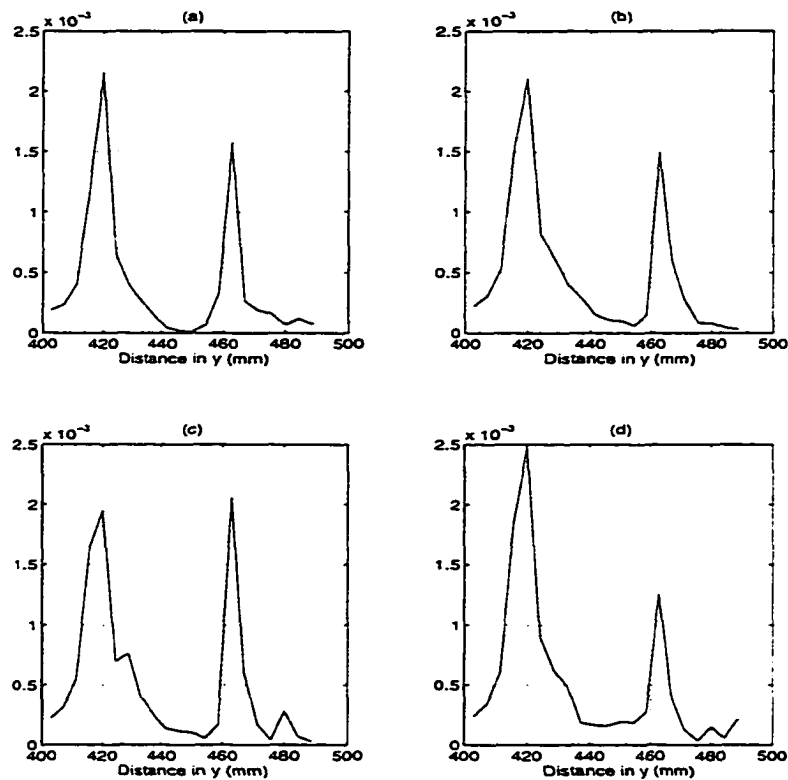


Figure 12.12 Signals due to interface specular reflections at four different antenna positions: (a) $x = -70$ mm, (b) $x = -30$ mm, (c) $x = 10$ mm, and (d) $x = 50$ mm.

12.4 Image Formation and Processing

Before forming the image the relative refractive index of the host material is required. For our purpose here, we assume that this parameter is known *a priori*, i.e., $n = 1.6$. Figure 12.13 shows different images due to different widths of the notch filter used. The value of ξ is vital in the quality of the final image. If ξ is too small, the specular is not removed enough and the interface will dominate or some spurious objects may appear in the image; if ξ is too large, then signals from the real targets are affected such that the resultant image is also severely distorted.

In Fig. 12.13(d) we only see the two stronger targets while the two weaker ones are almost invisible. This is due to the contrast of the image. One simple way is to split the

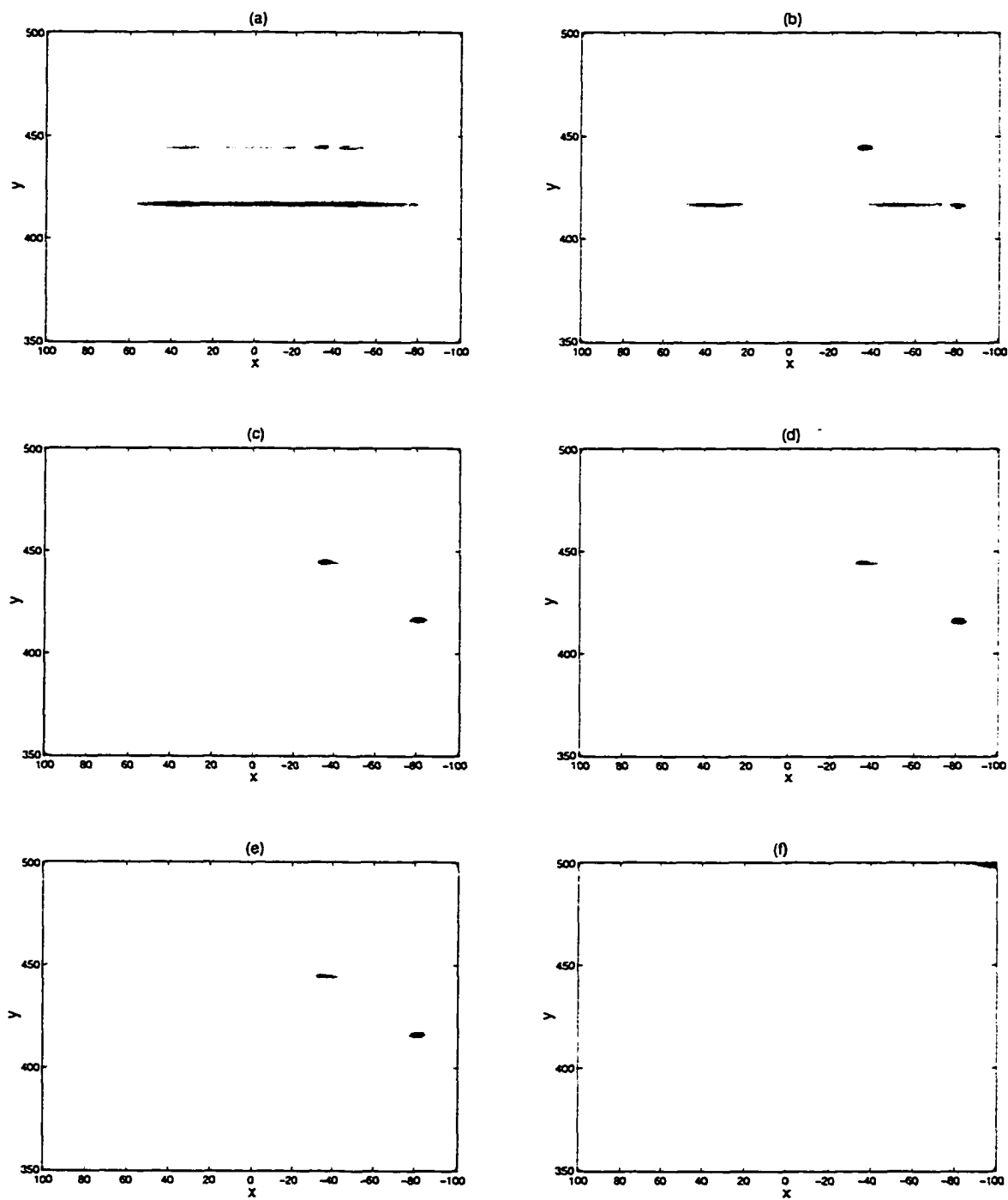


Figure 12.13 Images from Experiment I with different widths of notch filters. (a) $\xi = 0$, (b) $\xi = 0.005$, (c) $\xi = 0.01$, (d) $\xi = 0.05$, (e) $\xi = 0.08$, and (f) $\xi = 0.15$.

image into several sub-domains so that the dynamic range of pixel values in each sub-domain becomes moderate. In our case we split the image into two, the left and the right. The maximum pixel values are drastically different in the the two images as indicated by colorbars in the same figure. Now, after splitting, we do see some objects in the left image which were not observable originally. It is also noticed that this left image is somewhat distorted. Probably it is due to the sidelobes of the strong targets in the right image, which motivates us to seek better methods of revealing the weak targets.

Figure 12.15 shows two images of Experiment I. Figure 12.15 (a) corresponds to positive looking image, and (b) to negative looking image. It is seen that now the two originally weak targets can clearly been seen in the positive looking image. The submerging effect from the strong targets is reduced. Judging from these two images would provide a whole picture about the number of objects, their distributions, and their relative strength.

Going through the same process we form the image for Experiment II. It is mentioned that the only difference between the two experiments is that a metallic washer is included in Experiment II. Fig. 12.16 shows the images before and after the specular reflection is removed. Fig. 12.16(a) shows the image formed directly via raw data. It is noticed that the strong specular reflection obscures the whole image. What is basically seen in this image is the front and the back surface of the slab, with the former much stronger than the latter. On the other hand, Fig. 12.16(b) exhibits effect of specular reflection removal, which is twofold: better reveal of the targets and suppression of the ringing effects associated the strong specular reflection, making the region in front of the slab much cleaner. For the sake of comparison, we further pinpoint the objects in Fig. 12.16(b) and re-plot it in Fig. 12.17. The numerical data shown on the top of the image are targets dimensions (2D) both calculated from the image and physically measured (putting in parentheses) from the experimental setup.

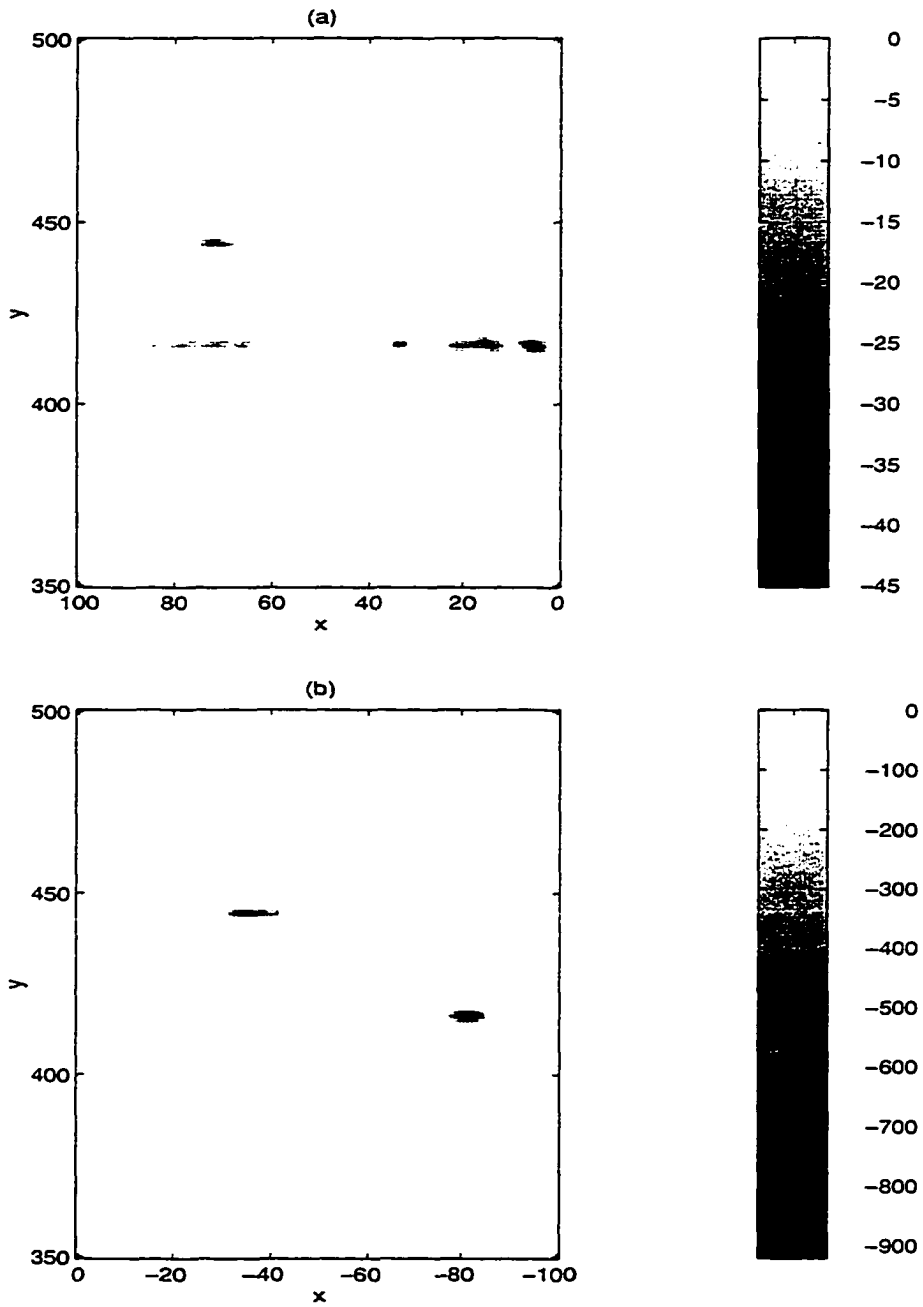


Figure 12.14 Split images to reveal weak targets.

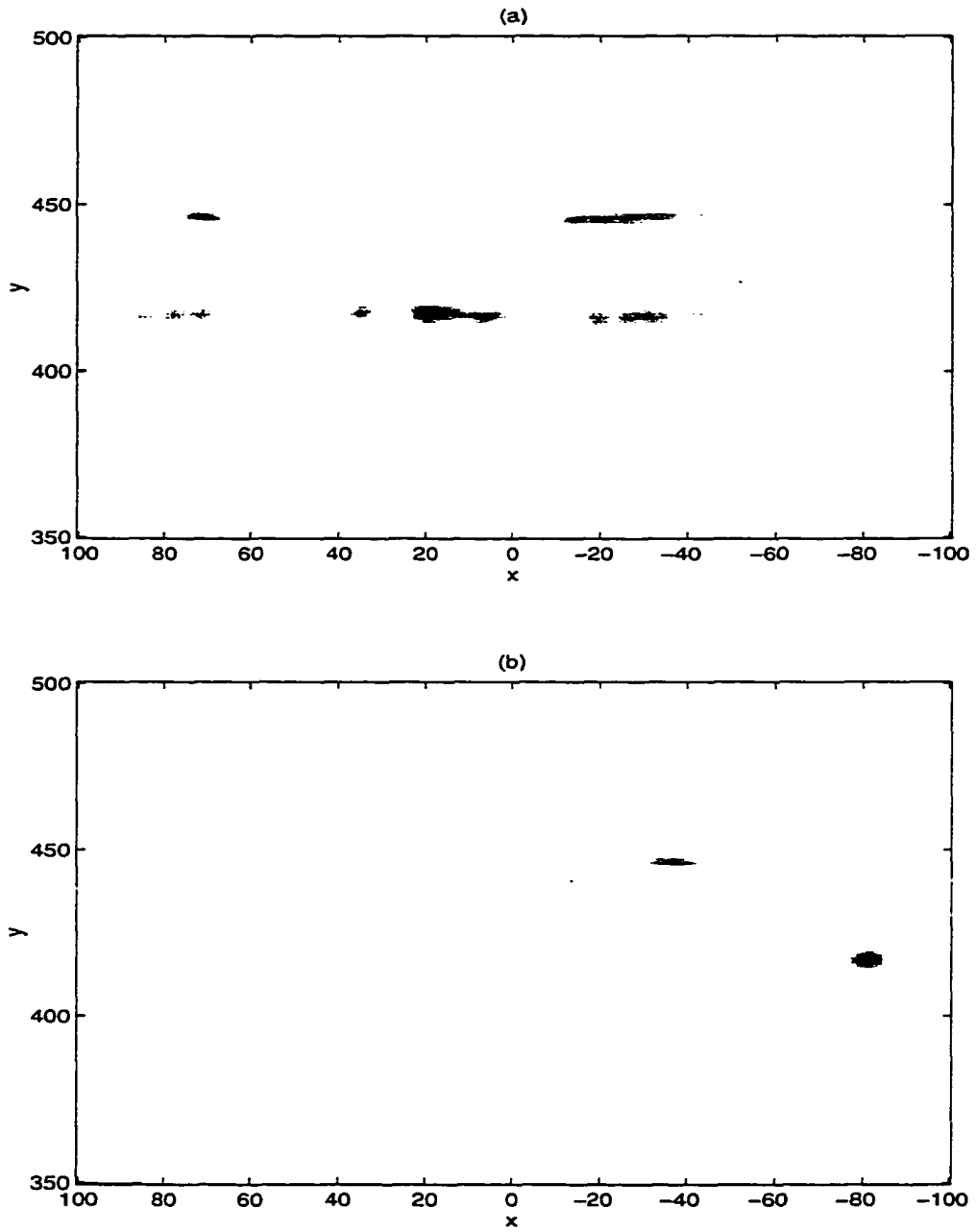


Figure 12.15 Positive and negative looking images to reveal weak targets.
(a) positive looking image, and (b) negative looking image.

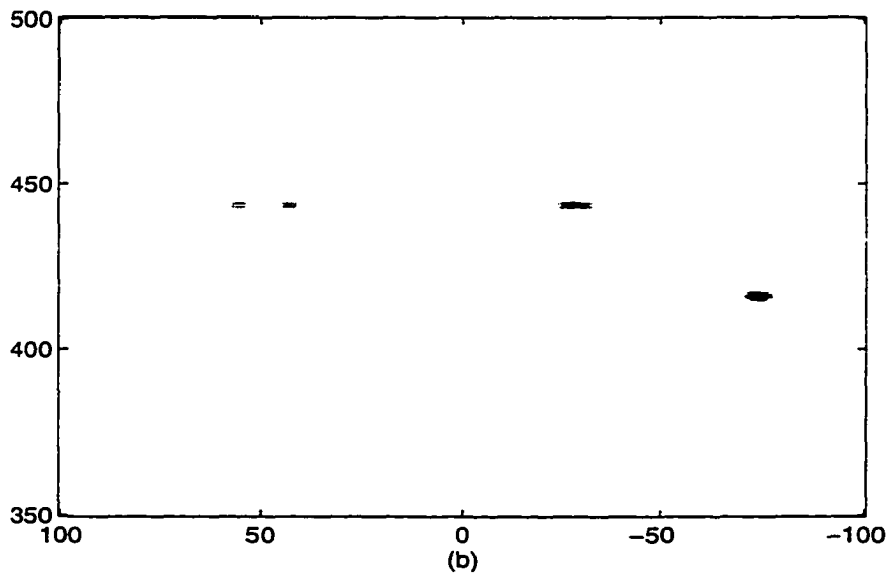
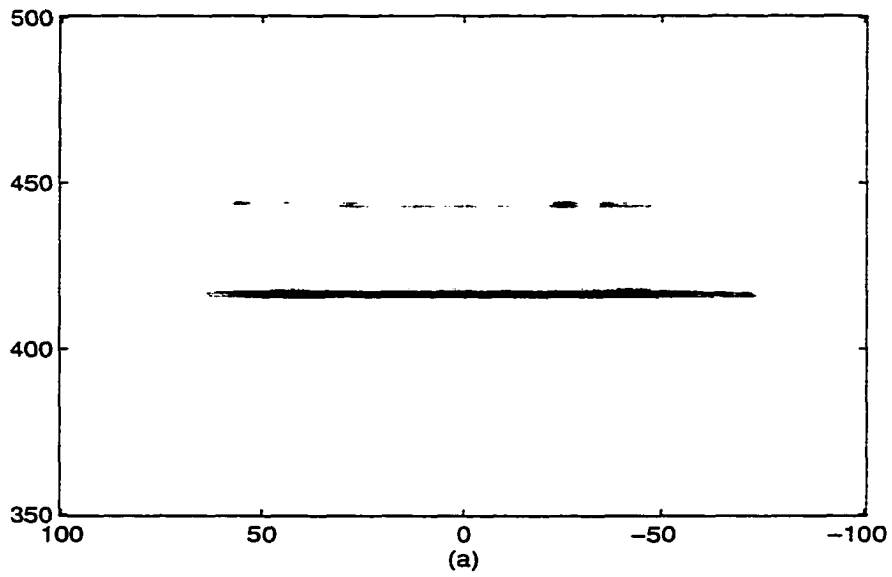


Figure 12.16 Images for Experiment II: (a) without specular reflection removal ($\xi = 0$), and (b) with specular reflection removal ($\xi = 0.05$).

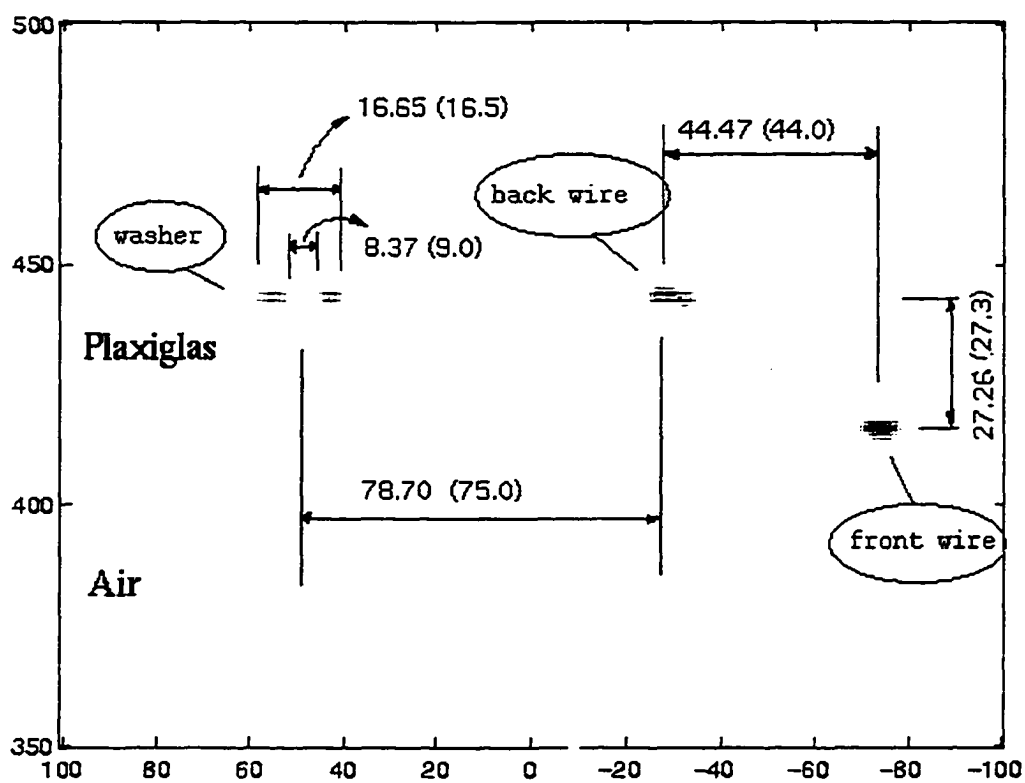


Figure 12.17 SAR image for Experiment II with dimensions denoted.

CHAPTER 13 DIELECTRIC PERMITTIVITY ESTIMATION

Dielectric permittivity ϵ is related to refractive index n by $n = \sqrt{\epsilon}$. As n changes so is the EM wave propagation speed. Consequently, the radar return signal phase also changes given that the target location is the same. In Part I, several algorithms were proposed allowing us to obtain n . Here, we propose another approach to estimating n by means of two images corresponding to different looking angles and cross-correlation of the images. Then, we will demonstrate that the algorithms developed in Part I could also be applied at no cost of extra effort for imaging process while obtaining n .

13.1 Background

In the last chapter it was shown that through FFT we could form images using signal portions from different looking angles. The parameter estimation algorithm in this chapter is developed based on the idea. The algorithm starts with the formation of two images. one corresponds to the positive looking image, and the other to the negative looking image. If the targets are point-like, the two images would be rather similar provided that the material parameter is correct. The more the estimated n deviates from its true value, the farther apart these two images. Then, it is through some similarity comparison that the refractive index n is estimated. In our study we simply use the normalized two-dimensional cross correlation as the mathematical criterion for refractive index estimation. For this purpose we define $r_m(\ell_x, \ell_y)$ and $r_i(\ell_x, \ell_y)$ for magnitude image and intensity image, respectively, as

$$r_m(\ell_x, \ell_y) = \frac{\sum_p \sum_q M_+(p, q) M_-(p - \ell_x, q - \ell_y)}{\sqrt{\sum_p \sum_q M_+^2(p, q)} \sqrt{\sum_p \sum_q M_-^2(p, q)}} \quad (13.1a)$$

$$r_i(\ell_x, \ell_y) = \frac{\sum_p \sum_q I_+(p, q) I_-(p - \ell_x, q - \ell_y)}{\sqrt{\sum_p \sum_q I_+^2(p, q)} \sqrt{\sum_p \sum_q I_-^2(p, q)}} \quad (13.1b)$$

where, M_+ and M_- represent positive looking and negative looking magnitude images, and I_+ and I_- represent positive looking and negative looking intensity images. It is implicitly understood that indices p , q , $p - \ell_x$, and $q - \ell_y$ are defined. Also, for our purpose here we only consider the situation where both lags in x and y are zeros, i.e., $r_m(0, 0)$ or $r_i(0, 0)$.

13.2 Simulation Examples

In order to verify our proposed algorithm for estimating the refractive index of the dielectric material through imaging, we perform some simulations. The geometry of the simulation is as follows: The antenna baseline is in parallel with the interface of the two media with $n_{r0} = 1$ and $n_r = 2.0$. The distance between the interface and the antenna baseline is 200 mm. The searching area is bounded by $x_{\min} = 30$, $y_{\min} = 200$, $x_{\max} = 120$, and $y_{\max} = 300$. Seven different point-target distributions are simulated. They are so arranged as to be representative of various combinations and are described in the following table.

Altogether nine different values for n_r are used to form images. These values are 1.6, 1.7, 1.8, 1.9, 2.0, 2.1, 2.2, 2.3, and 2.4. The two-dimensional cross correlation results are displayed in Fig. 13.1. It is seen that except in Case 5 and Case 6, the rest curves show maximum at $n_r = 2$. This supports the proposed algorithm. On the other hand, the reason that Case 5 and Case 6 do not show obvious peaks at $n_r = 2$ is that the targets are arranged at the same y -coordinate and the multiplication of the two images may not tell the true story. Both magnitude and intensity images reveal the same trend.

We can estimate the refractive index to within 10%. This is not possible by judging

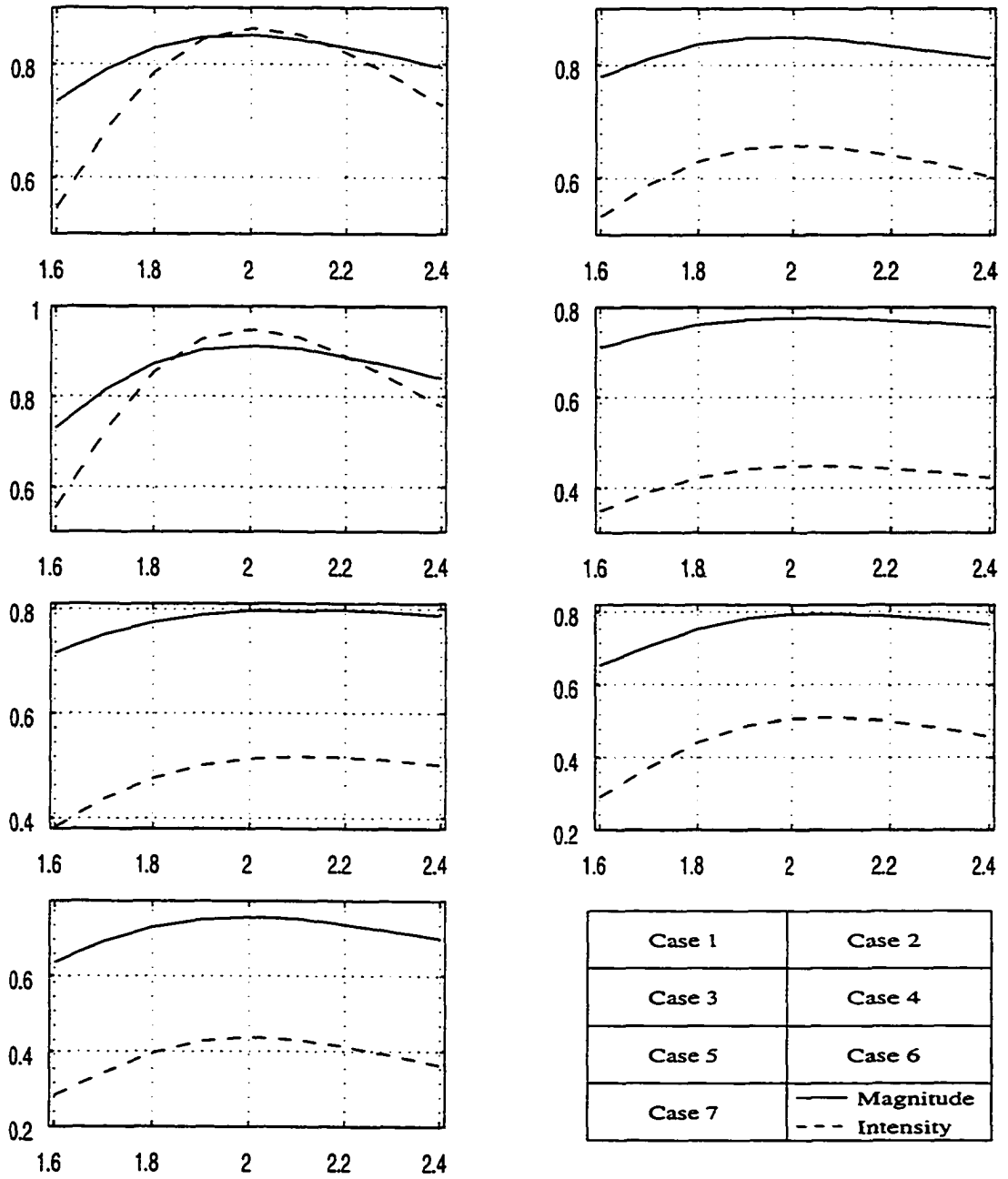


Figure 13.1 2-D cross-correlation results for seven different cases.

Table 13.1 Seven different cases of target distributions

Case	Number of targets	Target(s) coordinates
1	One	(80, 250)
2	Two	(50, 215), (80, 250)
3	Two	(70, 260), (70, 230)
4	Three	(40,220), (80, 250), (90, 230)
5	Four	(50, 230), (65, 230), (80, 230), (95, 230)
6	Four	(50, 250), (65, 250), (80, 250), (95, 250)
7	Five	(50, 220), (100, 220), (75, 250), (50, 280), (100, 280)

solely from the images. In fact, the images do not get blurred even when n_r deviates by over 20%. In Fig. 13.2 we show the images for Case 4 with $n_r = 1.6, 2.0, 2.4$, respectively. From these images all the targets have similar compactness (or sprawling); we do observe deviations of the target locations when n_r is incorrect. Unfortunately, this knowledge on location is not known to us in practice.

13.3 Application of Algorithm II from PART I

Algorithm II developed in Part I can be used to retrieve the permittivity of the host material, which is, in turn, used in forming the corresponding image. The process is shown in Fig. 13.3 and described in words as: Data D_1 is obtained from SAR imaging experiment. Then IFFT is applied at every given antenna position x to transform f into t , resulting in data D_2 . A window in time domain, $w(t; x)$, is applied to D_2 such that the effect of antenna horn mismatch and the scattering from distant objects are removed. The processed data is now D_3 , to which FFT is applied with respect to t to get data D_4 , which is the counterpart of D_1 . D_4 is FFTed with respect to space x for each fixed f . This produces D_5 . To single out data at $\phi = 0$, a filter, $H(\phi; f) = \delta(\phi)$, is adopted to convert D_5 into D_6 . When IFFT is used with respect to ϕ we obtain D_7 . It is known from the DFT property that for a given f , the magnitude of D_7 does not change with x . Thus a

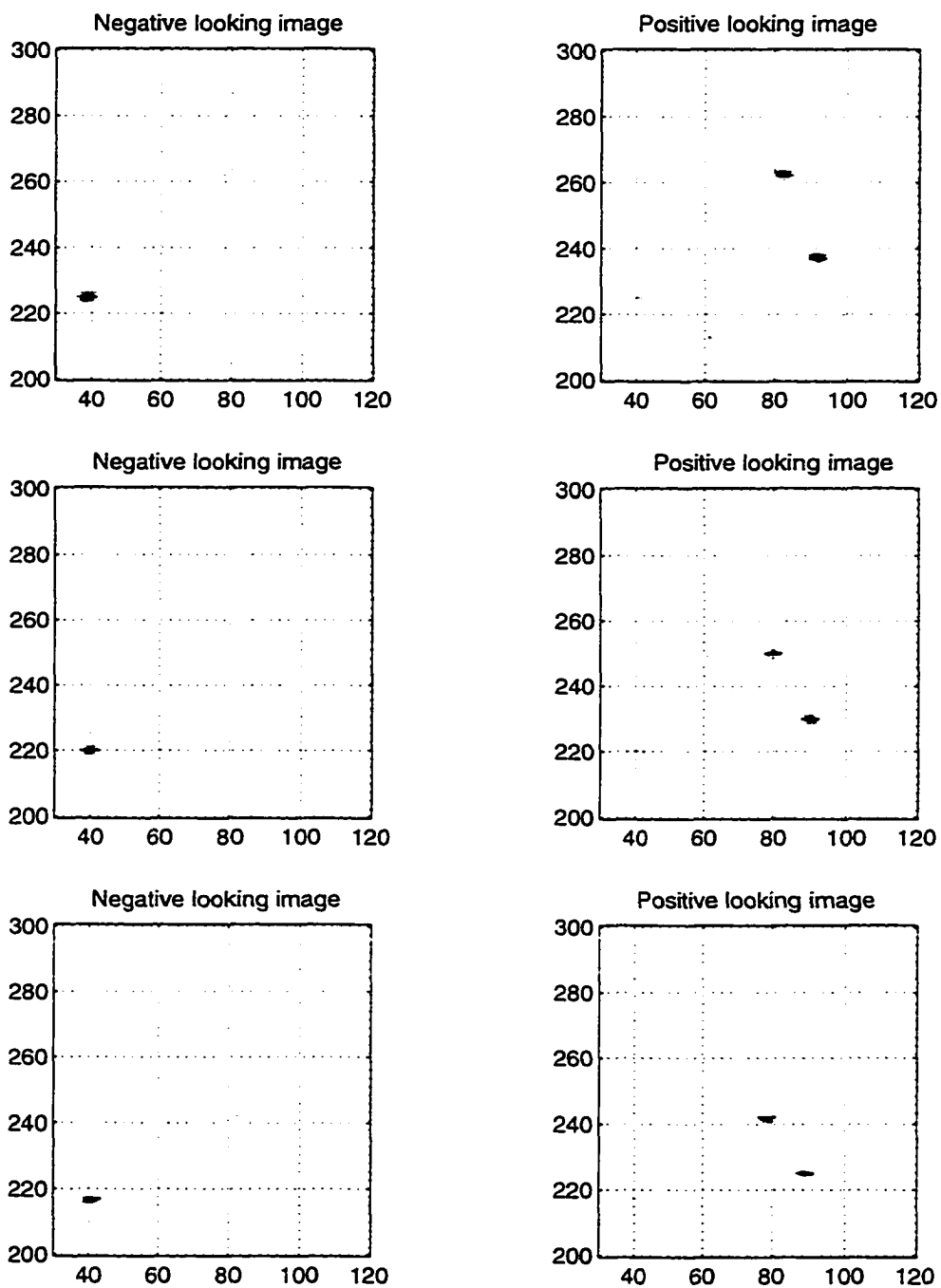


Figure 13.2 Images for different values of n_r for Case 4 (three targets). Top row is for $n_r = 1.6$, middle row is for $n_r = 2.0$ (true value), and bottom row is for $n_r = 2.4$.

value is chosen for any x_0 , ($x_1 \leq x_0 \leq x_{N_x}$), and only keep its magnitude (i.e., discarding its phase). When this is done for all the temporal frequencies, we get $|R(f)|$ spectrum.

To use inversion Algorithm II proposed in Part I, we need to correct $|R(f)|$ due to two reasons. First, the distance effect should be taken into account. This is readily accomplished using (6.1). The second reason for correction is as follows: when converting D_6 to D_7 we ascribe the magnitude at $\phi = 0$ to specular reflection exclusively. In fact, noise and signal not connected to specular reflections will also contribute energy at $\phi = 0$. In Part I it was shown that $|R(f)|$ spectrum has all its minima at zero, assuming the dielectric slab to be lossless. Hence, at those frequencies where $|R(f)|$ reaches minima we assign zero values to them, arguing that the nonzero value is due totally to noise, we call this process *null-point correction*. On the other hand, at maxima of $|R(f)|$ noise may be added to the real signal constructively or destructively, or anything in between. This makes the decision of not altering these values at the corresponding temporal frequencies seem more appropriate. All the values in between a minimum and its neighboring maximum are scaled according to the following operation, applied one half of a period at a time.

$$|R(f)|^2 = \frac{|R'(f)|^2 - \min\{|R'(f)|^2\}}{\max\{|R'(f)|^2\} - \min\{|R'(f)|^2\}} \times |R'(f)|^2 \quad (13.3)$$

where $|R'(f)|$ is the reflection coefficient before null-point correction.

To see how these algorithms work we did three experiments, each is a modification of the previous one. For each experimental data set, the $t-x-\theta$ Method is used to form the corresponding image. The permittivity of the Plexiglas slab is estimated by Algorithm II proposed in Part I and by cross-correlation method with two distinct images of the same scene corresponding to positive and negative spectra, i.e., $+\phi$ and $-\phi$ (or $-\theta$ and $+\theta$). The frequency range is from 75 to 110 GHz, which is increased in 800 steps. The antenna baseline is approximately set in parallel with the Plexiglas surface. The horn antenna moves in stepsize 1 mm. Thus, a synthesized aperture of 128 mm is formed.

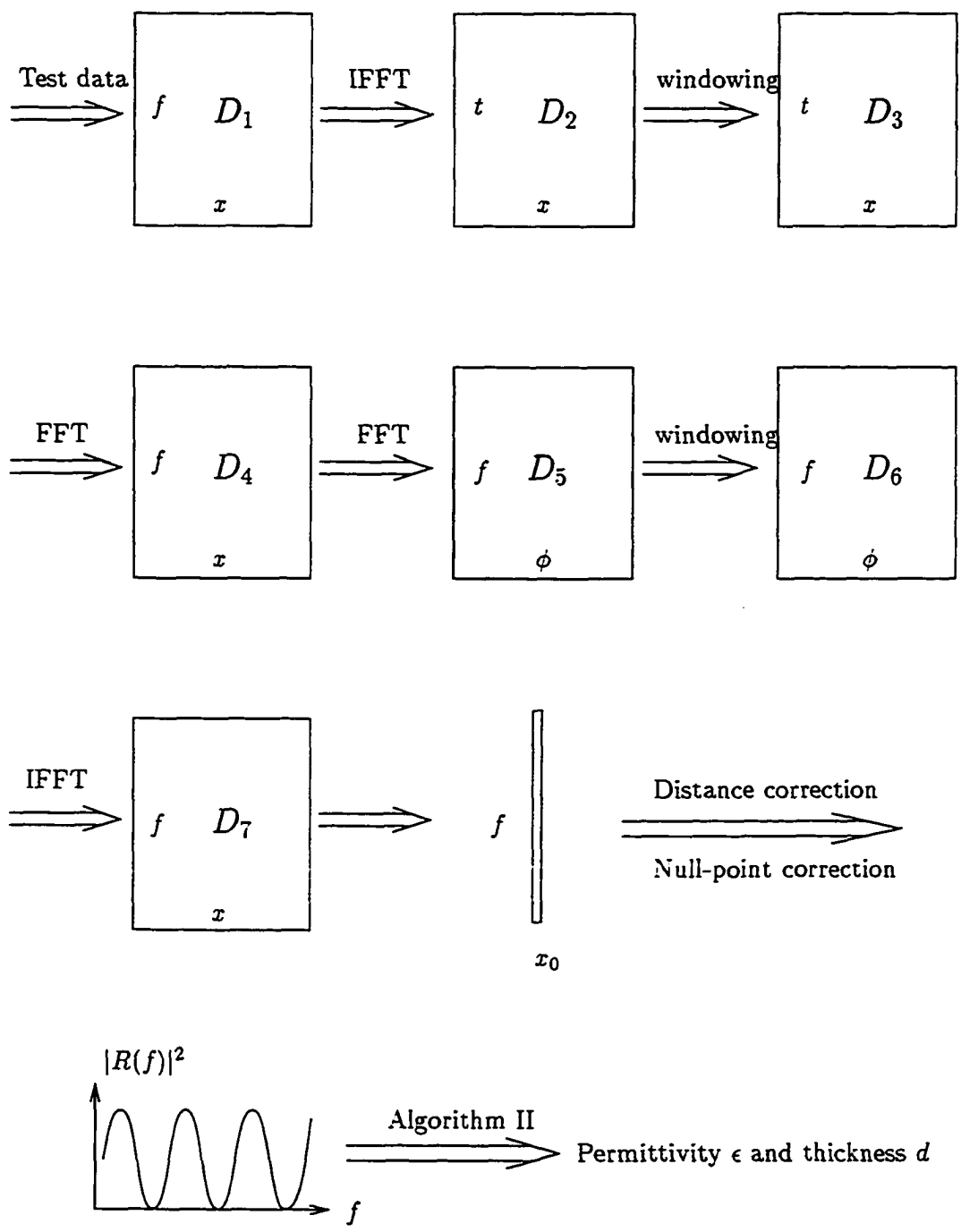


Figure 13.3 Flowchart showing the process for obtaining ϵ and d from SAR imaging data using Algorithm II developed in Part I.

13.4 Experimental Verification

13.4.1 Single Wire Experiment

The experimental setup for a single metallic wire is shown in Fig. 13.4. The wire is attached to the back surface of the Plexiglas slab.

First, we use Algorithm II and follow Fig. 13.3 to obtain the relative refractive index n_r . Using (3.19), (3.20), (3.15a), (3.15b), and (3.5) through (3.11) we obtain

$$f_0(\beta, \delta) = 0.065695, \quad f_1(\beta, \delta) = -0.051261, \quad \text{and} \quad n_r = 1.5967.$$



Figure 13.4 Experimental setup for single wire experiment.

We can then get the contour plot of the cross-correlation between two images of the same scene for $n_r = 1.2, 1.4, 1.6, 1.8,$ and 2.0 . This is shown in Fig. 13.5. And we obtain $n_r \approx 1.55$. The resultant gray level intensity image using $n_r = 1.6$ is shown in Fig. 13.6. The peak center in y -direction is approximately $348.3 (=321+27.3)$ mm.

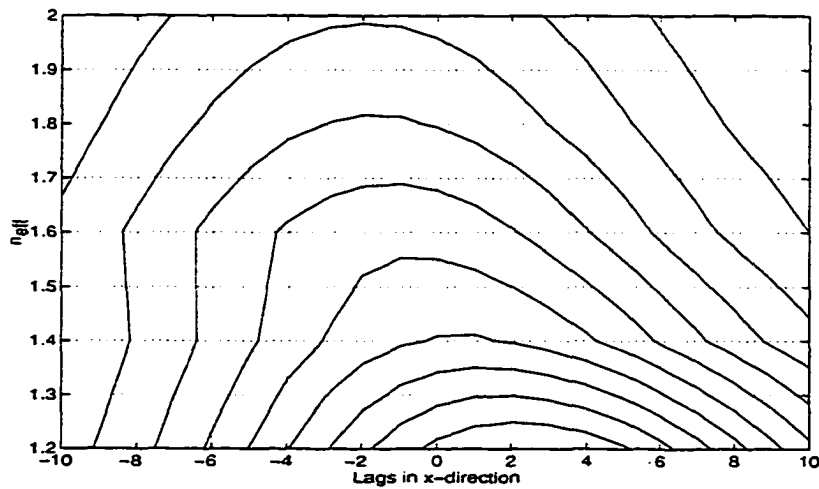


Figure 13.5 Cross-correlation result of two images at different refractive indices for single wire experiment.

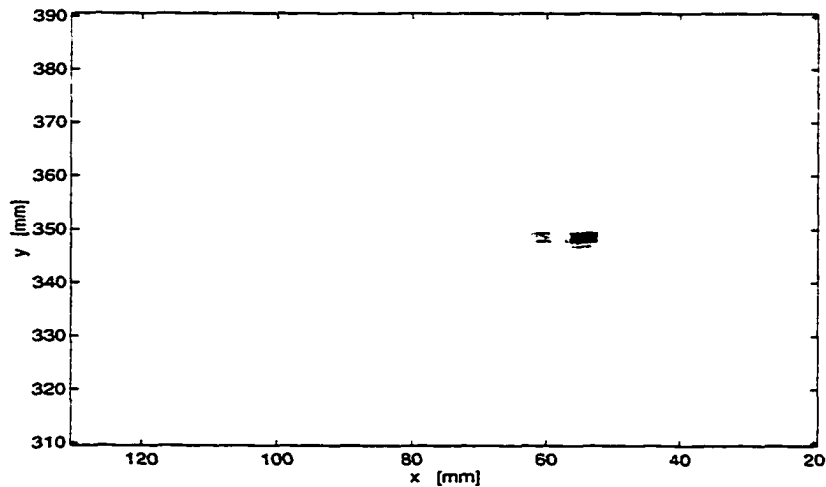


Figure 13.6 Image for single wire experiment with $n_r = 1.6$.

13.4.2 Double Wire Experiment

The experimental setup is the same as shown in Fig. 13.4, except that now two metallic wires are attached to the back surface of the Plexiglas slab. The separation between the two wires is 1 inch (25.4 mm).

Using (3.19), (3.20), (3.15a), (3.15b), and (3.5) through (3.11) we obtain

$$f_0(\beta, \delta) = 0.066344, \quad f_1(\beta, \delta) = -0.060865, \quad \text{and} \quad n_r = 1.5352.$$

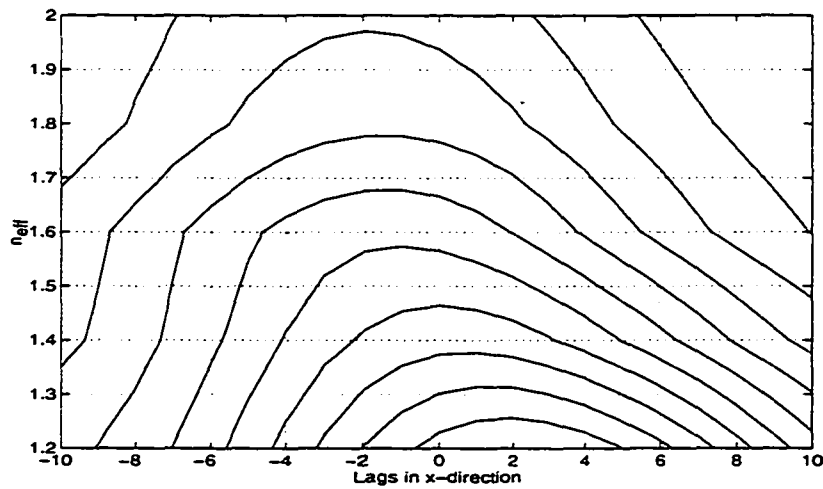


Figure 13.7 Cross-correlation result of two images at different refractive indices for double wire experiment.

Using auto-focusing technique we get the contour plot of the cross-correlation shown in Fig. 13.7. The relative refractive index thus obtained is about 1.51. The resultant gray level intensity image using $n_r = 1.6$ is shown in Fig. 13.8. The centers of the peaks in y -direction are approximately 348.3 ($=321+27.3$) mm. The separation between the two peak centers is indeed approximately 25.4 mm.

13.4.3 Triple Wire Experiment

The experimental setup is the same as shown in Fig. 13.4, except that now three metallic wires are attached to the back surface of the Plexiglas slab. The separation

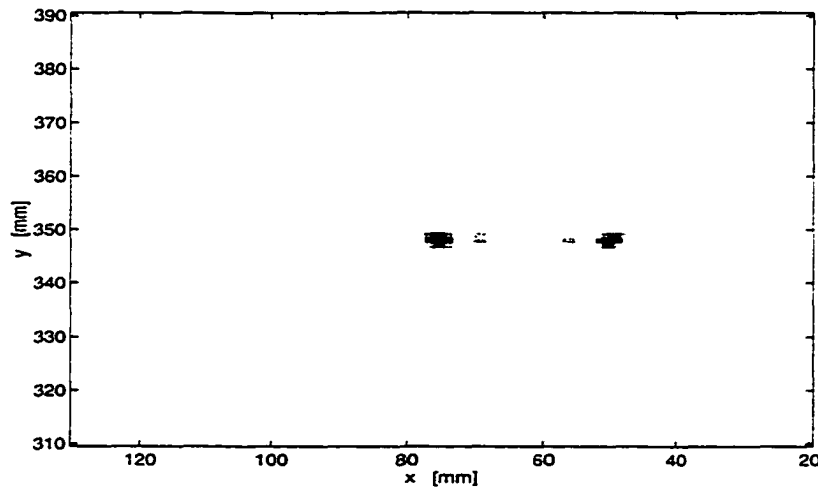


Figure 13.8 Image for double wire experiment with $n_r = 1.6$.

between the two neighboring wires is 1 inch (25.4 mm).

Using (3.19), (3.20), (3.15a), (3.15b), and (3.5) through (3.11) we obtain

$$f_0(\beta, \delta) = 0.065278, \quad f_1(\beta, \delta) = -0.061292, \quad \text{and} \quad n_r = 1.5107.$$

Using auto-focusing technique we get the contour plot of the cross-correlation shown in Fig. 13.9. The relative refractive index thus obtained is about 1.50. The resultant gray level intensity image using $n_r = 1.6$ is shown in Fig. 13.10. The centers of the peaks in y -direction are approximately 348.3 ($=321+27.3$) mm. The separation between the two neighboring peak centers is approximately 25.4 mm.

13.5 Summary of Results

To compare the results we put together the estimated refractive indices in Table 13.2. From the table we see that the more targets the less precise is the estimated refractive index. However, even for the worst case the error is still tolerable from engineering point of view. The reference value for n_r is chosen to be 1.597, obtained in Chapter 12.

Table 13.2 Comparison of n_r obtained via different methods

Experiments	n_r (Algorithm I)	n_r (Auto-focusing & cross-correlation)
Single wire	1.5967	1.55
Double wire	1.5352	1.51
Triple wire	1.5107	1.50

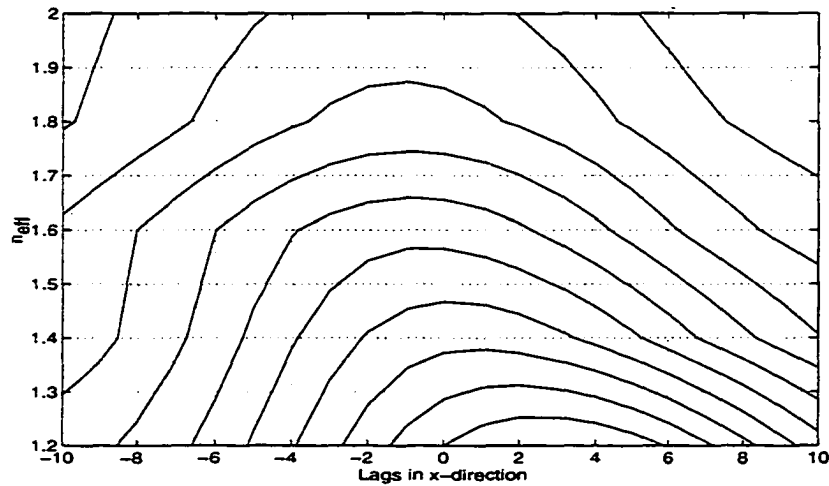
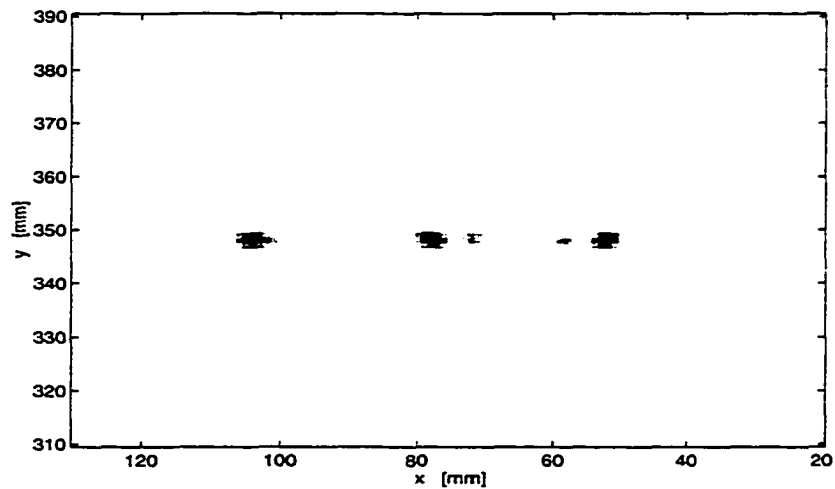


Figure 13.9 Cross-correlation result of two images at different refractive indices for triple wire experiment.

Figure 13.10 Image for triple wire experiment with $n_r = 1.6$.

CHAPTER 14 CONCLUSION TO PART II

It is demonstrated in this part that our algorithms for SAR imaging of embedded objects inside dielectric materials not only work well with theoretical simulation, but also with real experimental data. The SAR collected data are viewed in different domains, making possible the post-processing of the data during image formation stage more flexible and ensures better image quality. The host material permittivity has been successfully estimated through different algorithms. All this is done in one single experimental scan.

PART III

**PRELIMINARY INVESTIGATION ON
THREE-DIMENSIONAL IMAGING VIA InSAR**

CHAPTER 15 INTERFEROMETRIC SAR 3-D IMAGING

15.1 Introduction

Synthetic aperture radar provides an all-weather means of imaging objects for many purposes. However, the conventional SAR is only able to form two-dimensional images, i.e., the down-range (y) vs. cross-range (x). Two targets with the same distance from the antenna but different elevation angles will be interpreted as having the same elevation angle but different down-ranges as well as cross-ranges. The addition of elevation information makes possible the 3-D imaging, which is necessarily required in many situations.

3-D radar imaging is at an exploratory stage of development. Due to the difficulty of obtaining full 3-D data sets in operational conditions, results in this area have largely been obtained in opportunistic or laboratory situations [105]. However, there are some exceptions, especially the interferometric SAR, or InSAR (and sometimes also called IF-SAR), which has successfully generated contour maps of continuously varying terrain. Other methods of forming a 3-D image include (1) synthesizing a two-dimensional filled radar aperture [73]. This increases the complexity of the experiment and the requirement on post-data processing. The problem of constructing aperture synthesis systems which cover a given rectangular domain of spatial frequencies was considered to reach minimum redundancy in [106]. However, the complexity is only lessened to some degree. Another attempt is through stereo SAR. In [107] curvilinear aperture was used. The data set is projected in three orthogonal directions. Because the projected space contains data which are undersampled, the high sidelobes present in such images may be larger than the main response of other significant scatterers thus veiling their appearance. In [108] height

computation is presented in the spotlight stereo SAR mode.

On the other hand, in our process of SAR data, one of the final steps involves converting the complex image to the intensity image, thus throwing away part of the information contained in the phase of the complex image. Graham first demonstrated that InSAR, which uses phase information, can achieve the status that range can be resolved to less than the wavelength [109, 110]. In the spotlight mode SAR, there exists a simple derivation which shows, through 3-D Fourier transform without utilizing reference to Doppler concepts, the fundamentals of InSAR as well as the easily-seen link between image domain phase difference and terrain elevation height [111].

15.2 Basic Theory of InSAR

The basic theory of InSAR processing is as follows. The received signals from both antennas are independently processed to form two complex images. The two images may be formed simultaneously, or at different times. Then the interferogram of two co-registered images is computed. Through the interferogram can the information about targets elevation be retrieved [112].

In Fig. 15.1 it is seen that the signal phase difference at a given frequency, f , is

$$\phi_{12} = \phi_1 - \phi_2 = (-4\pi f/c \cdot r_1) - (-4\pi f/c \cdot r_2) \approx \frac{8\pi f z_0}{c} \cdot \frac{z_t}{y_t} \quad (15.1)$$

Hence, the elevation of the target is approximately

$$z_t = \frac{y_t \phi_{12} c}{8\pi f z_0} \quad (15.2)$$

It is noted that only the principal value for ϕ_{12} is known, which by definition satisfies $-\pi < \phi_{12} \leq \pi$. However, in using (15.2) the unwrapped value should be used. This makes necessary the process of phase unwrapping. To unwrap the phase we must assume that the variation of the targets elevation between adjacent pixels, added to the unavoidable noise, is not so high to produce phase variations greater than π . With real data this assumption

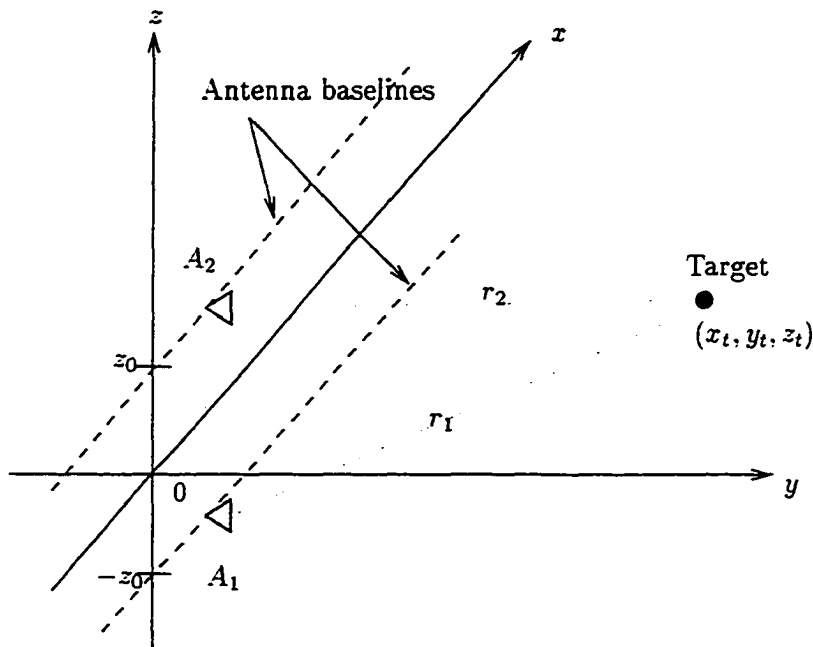


Figure 15.1 One possible geometry for InSAR: two antennas are separated only by a vertical (z -direction) distance.

is seldom satisfied because of loss of coherence or phase aliasing [113]. References about phase unwrapping can be found in [114]-[121]. On the other hand, it is possible sometimes for ϕ_{12} to be restricted to within $-\pi$ to π . This condition can be derived from (15.2) as

$$|z_t| \leq \frac{y_t \lambda_{min}}{8z_0} \quad (15.3)$$

Hence, the larger the z_0 , the smaller the vertical range of the targets for which no concerns should be felt about phase unwrapping. The trade-off is from another fact that the larger the z_0 , the better the vertical resolution.

ϕ_{12} in the above analysis is, in fact, the phase difference between the two returned signals. Its relationship to the the phase difference in the corresponding complex images is not straightforwardly seen. Here, a simple derivation is carried out so that this relationship should be clear. Also, attention has to be paid to the resultant phase by either CFT or DFT. To see the difference between the two, we assume a simple return signal $s(f)$ has

the form

$$s(f) = \exp(-j2\pi t_0 f)$$

The continuous Fourier transform from f -domain to t -domain yields

$$S(t) = \int_{f_{\min}}^{f_{\max}} S(f) \exp(j2\pi t f) = \exp[j2\pi(t - t_0) f_c] \cdot \Delta f \cdot \text{sinc}[(t - t_0)\Delta f] \quad (15.4)$$

where, f_c designates the center frequency defined as $f_c = (f_{\min} + f_{\max})/2$. Δf is the frequency bandwidth defined as $\Delta = (f_{\max} - f_{\min})$.

The discrete counterpart is

$$S(m) = \frac{1}{N} \sum_{n=0}^{N-1} s(n) \exp(j2\pi \frac{mn}{N}) = \frac{1}{N} \exp(-j2\pi t_0 f_{\min}) \cdot \sum_{n=0}^{N-1} \exp(j2\pi \frac{m - t_0 \delta f N}{N} n) \quad (15.5)$$

where, $s(n)$ is the sampled version of $s(f)$. N is the total data points. δf is the frequency stepsize.

Observing (15.4) and (15.5) it is seen that at $t = t_0$ (the peak position) the phases from the two derivations are very different. For the continuous case, the phase is zero, while for discrete case, the phase is $-j2\pi t_0 f_{\min}$. This will guide us to design the corresponding algorithms to extract the useful information.

15.3 InSAR Imaging Experimental Examples

In this section two experiments and their imaging results are presented.

15.3.1 Experiment I

Figure 15.2 shows the sample used for the experiment. There are two holes in the metallic plate, which was installed on the scanner 25° with respect to the vertical. The experiment consists of two scans, each one by itself is no different than the those experiments described earlier in the thesis. After the first scan, the scanner was lower by 10 mm, equivalent to raising the antenna by 10 mm. Thus, the separation of the two apertures

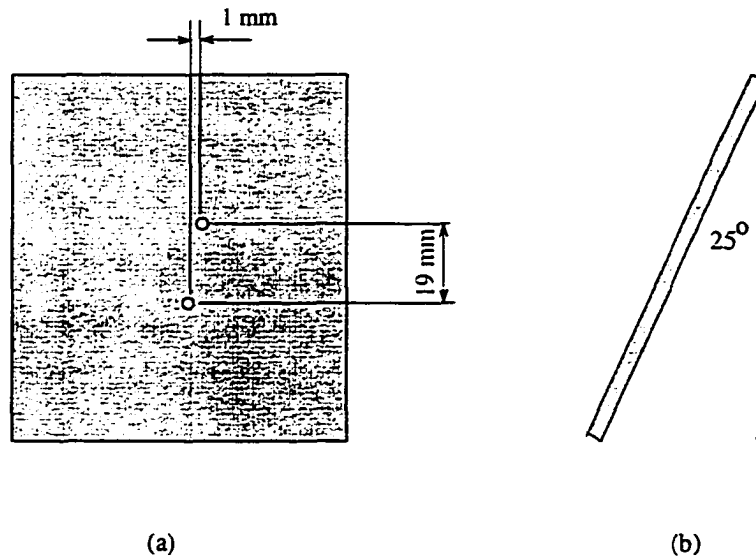


Figure 15.2 Setup for InSAR Experiment I: (a) a metallic plate with two holes in it, and (b) experimental setup with the plate tilted by 25° to reduce specular reflection.

is 10 mm, i.e., $z_0 = 5$ mm. Two data sets were obtained, which are used to form two complex images. The corresponding intensity images are shown in Fig. 15.3.

Zoomed-in images are shown in Figs. 15.4 (a) and (b), and it is seen that registration is needed before interferograms can be calculated. First of all, simple shift is necessary to align the images in the x direction. We choose to shift the image corresponding to the upper antenna in the x direction. The reason for this shift is as follows: The antenna is stepped through 127 steps, with increment being nominally 1 mm. However, the actual increment is about 0.99 mm. When the first scan is finished, the antenna is moved back by 127×1 mm. The scanner travels this larger distance more accurately. Hence, the antenna is brought approximately to -1.27 ($= -0.01 \times 127$) with respect to the starting position, which makes the targets at relatively more positive x coordinates. The shifted-back image is shown in Fig. 15.4 (c). Second, scaling is required. This is due to the relative angle change from the antenna to the targets. We stretched the upper image locally by 11.4%. The

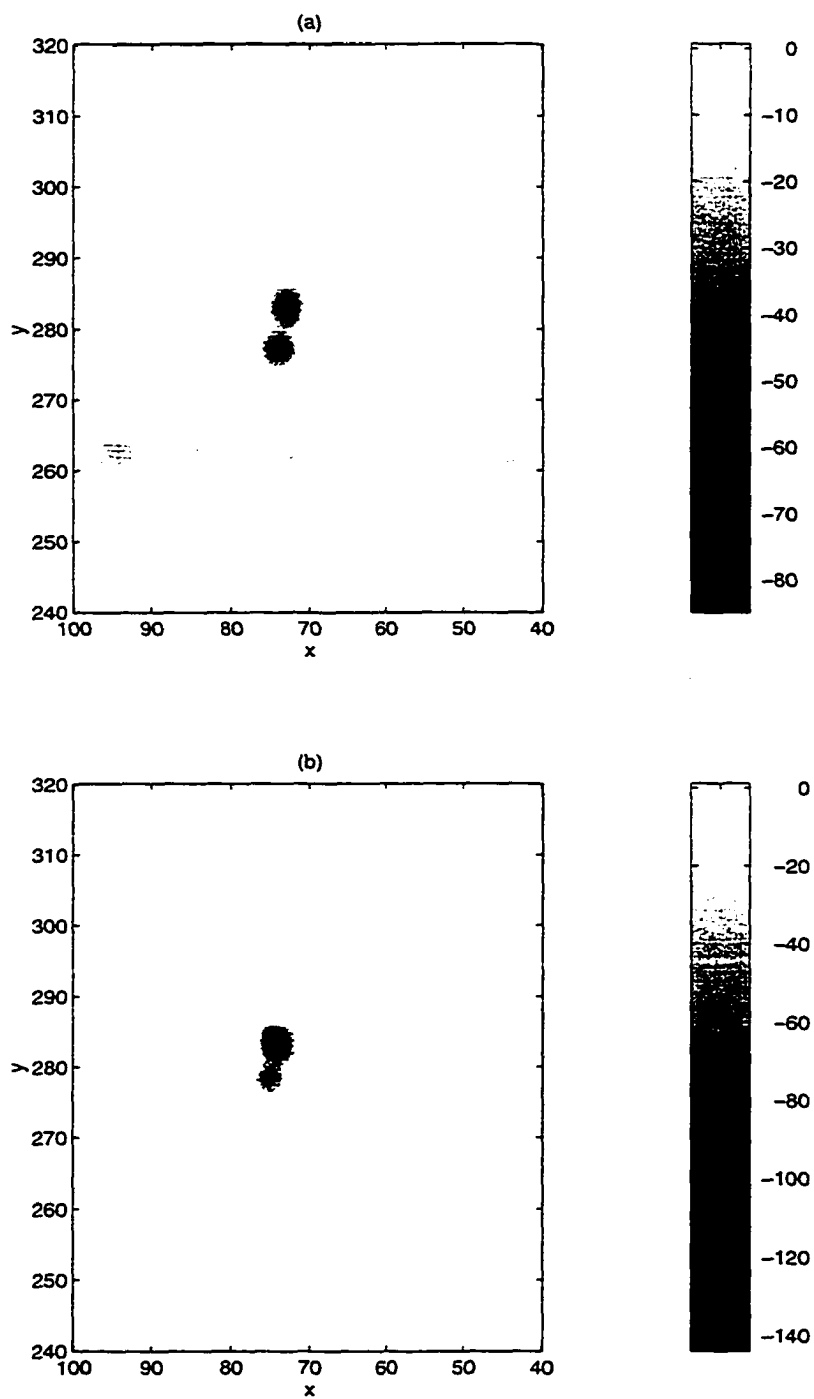


Figure 15.3 Intensity images formed using data collected from antennas at different elevations: (a) image corresponding to lower antenna, and (b) image corresponding to upper antenna.

final registered image for upper antenna is shown in Fig. 15.4 (d).

Once the images are co-registered, phase differences at each pixel can be calculated. This allows us to form the interferogram, which is displayed in Fig. 15.5 (b), together with the interferogram prior to registration shown in (a). The problem of phase unwrapping is not come across thanks to the specific experiment setup and targets geometry.

From Fig. 15.3 and Fig. 15.5 we can extract the range as well as elevation information. It can be estimated from the images that the distances from the antennas' mid-point along the vertical separation to the targets are 283.5 and 277.5 mm, respectively for Target 1 and Target 2. The phase difference for Target 1 at the center of the target is 1.3624 rad, and the average phase difference around the center with 7×7 pixels² (1.4×1.4 mm²) is 1.3736 rad. The phase difference for Target 2 at the center of the target is -0.4268 rad, and the average phase difference around this center is -0.4185 rad. Hence, the elevations for Targets 1 and 2 are, respectively, 12.294 and -3.770 mm using the phase difference at the centers, and are 12.395 and -3.696 mm using the average difference. Therefore, the separation between the two targets is 16.064 mm (using center phase difference) or 16.091 mm (using averaging phase difference). From the experimental setup, it is known that the vertical separation of the two holes is about 17.22 mm ($=19 \times \cos(25^\circ)$).

15.3.2 Experiment II

The setup for the second InSAR experiment is shown in Fig. 15.6. The experimental process is the same as in Experiment I.

After processing the data we obtain two complex images. The corresponding intensity images are shown in Fig. 15.7. Because of the relative position of the antenna and the wires, some wires are more visible in one image and less so in the other. Before the phase differences are extracted the two complex images must be properly registered. Here, as a preliminary study, we apply the method proposed in [122].

To properly register two complex SAR images, we want to minimize the average fluc-

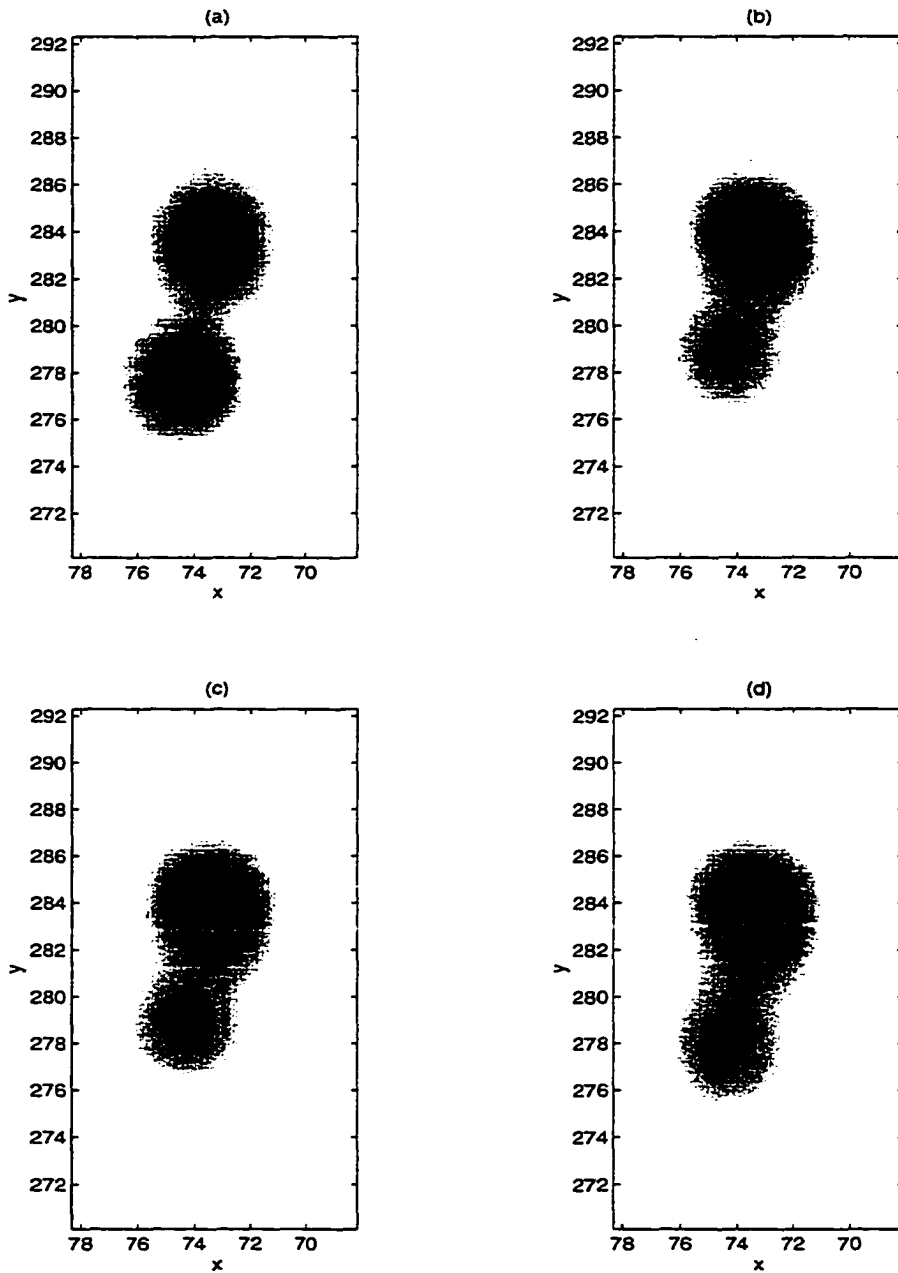


Figure 15.4 Zoomed-in intensity images showing simple image registration: (a) image related to lower antenna data, (b) image related to upper antenna data, (c) image in (b) shifted in x -direction by 6 pixels (1.2 mm), (d) image in (c) scaled up by 11.4%.

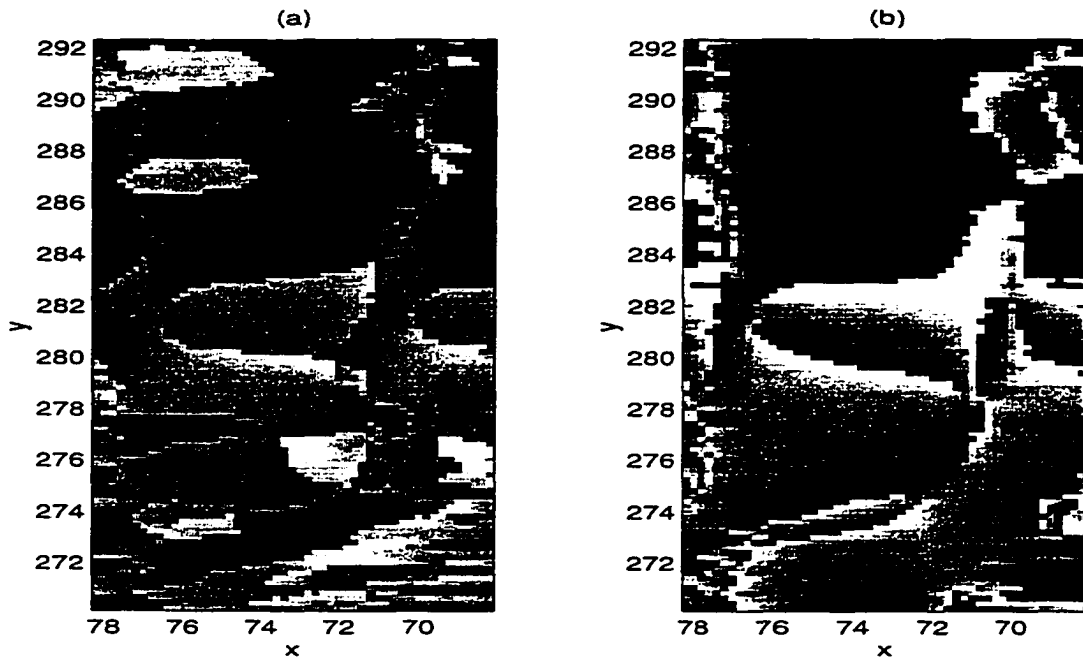


Figure 15.5 Zoomed-in interferograms. (a) before registration, (b) after registration.

tuation in the phase difference image defined as

$$g = \sum_p \sum_q (|P(p+1, q) - P(p, q)| + |P(p, q+1) - P(p, q)|) \quad (15.6)$$

where, $P(p, q)$ is the phase difference at pixel (p, q) . The summation is performed over all pairs of adjacent pixels in the image.

Fig. 15.8 shows the result by using (15.6). It is noticed that the minimum occurs at offset in y is 0 and in x is 2 pixels (1 mm). Figure 15.8(a) is the 3-D mesh plot and (b) is the contour plot. The corresponding phase difference (the interferogram) is shown in Fig. 15.9, together with the one before registration.

Elevations are calculated from the interferogram. For the purpose of visualization, a 2-D color image can be adopted to show 4-D data set, i.e., the x, y, z coordinates plus intensity. To this end the horizontal axis is used to represent the cross-range, and the

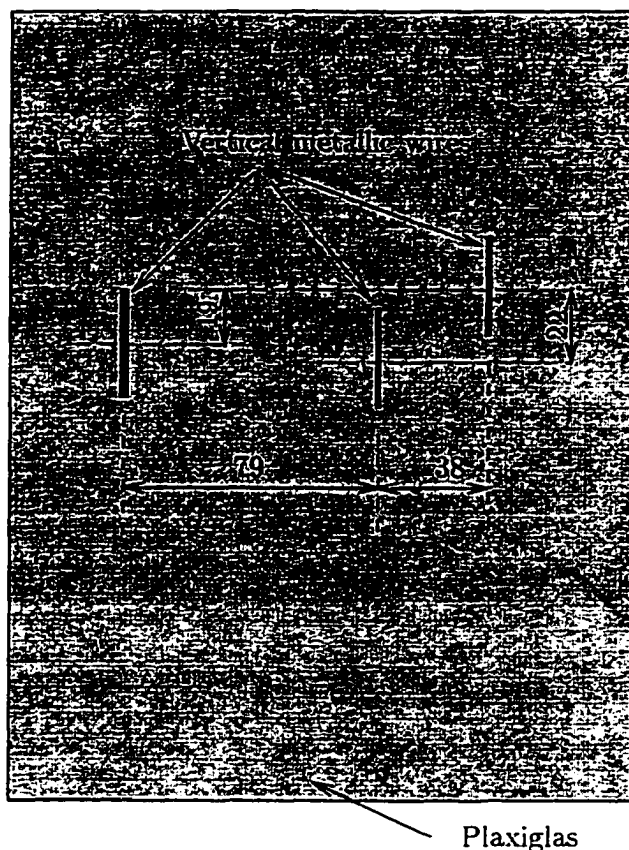


Figure 15.6 Setup for InSAR Experiment II: three short vertical metallic wires (about 20 mm in length) are attached to the front of a Plexiglas board.

vertical axis the down-range. The elevation of the targets can be represented by the *hue* component of the color, and the intensity by the *saturation* component of the color. To ensure the good visual effect the *value* component is set to its maximum number.

This 4-D color image is not included here because of thesis requirements. Instead, we resort to Table 15.1 to show separations obtained from experimental data in the x and z between the wires together with the directly measured ones. In the table, $s1_x$, $s2_x$, $s1_z$, and $s2_z$ represent the separation in x between left and middle wires, the separation in x between middle and right wires, the separation in z between left and right wires, and the separation in z between middle and right wires, respectively.

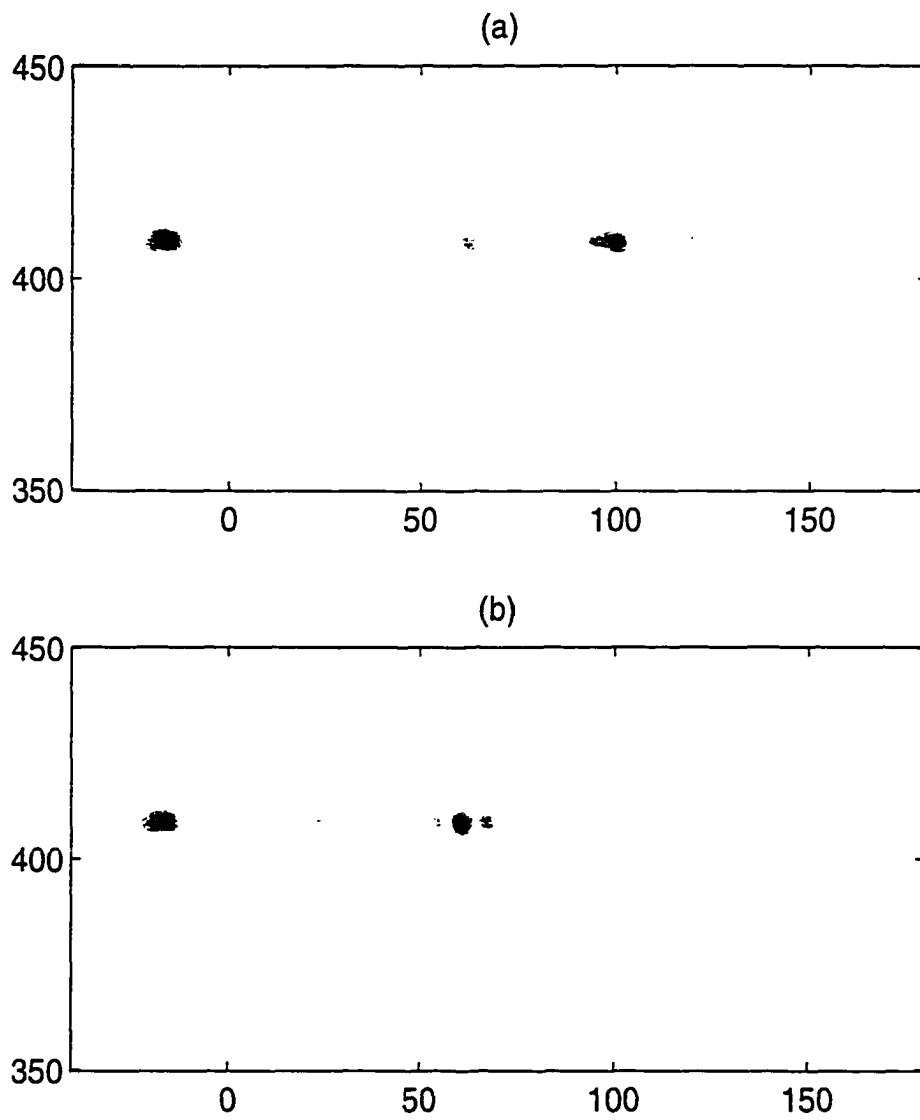


Figure 15.7 Two intensity images corresponding to (a) upper antenna, and (b) lower antenna.

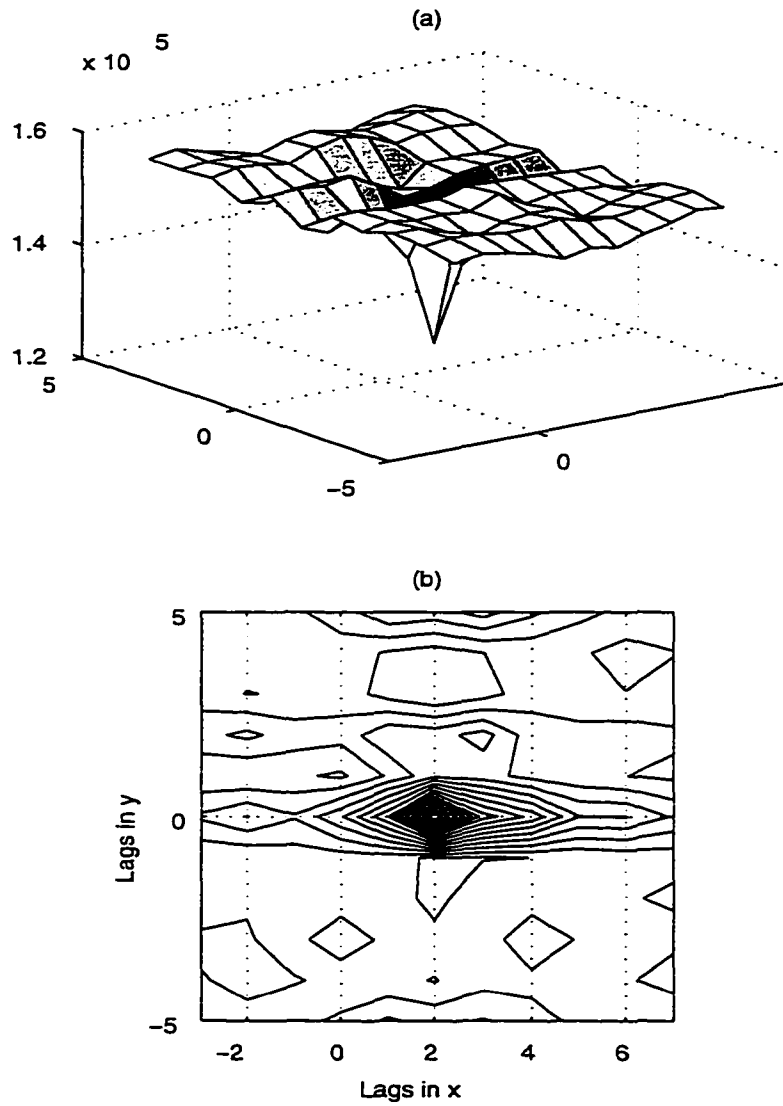


Figure 15.8 Registration through minimizing function g .

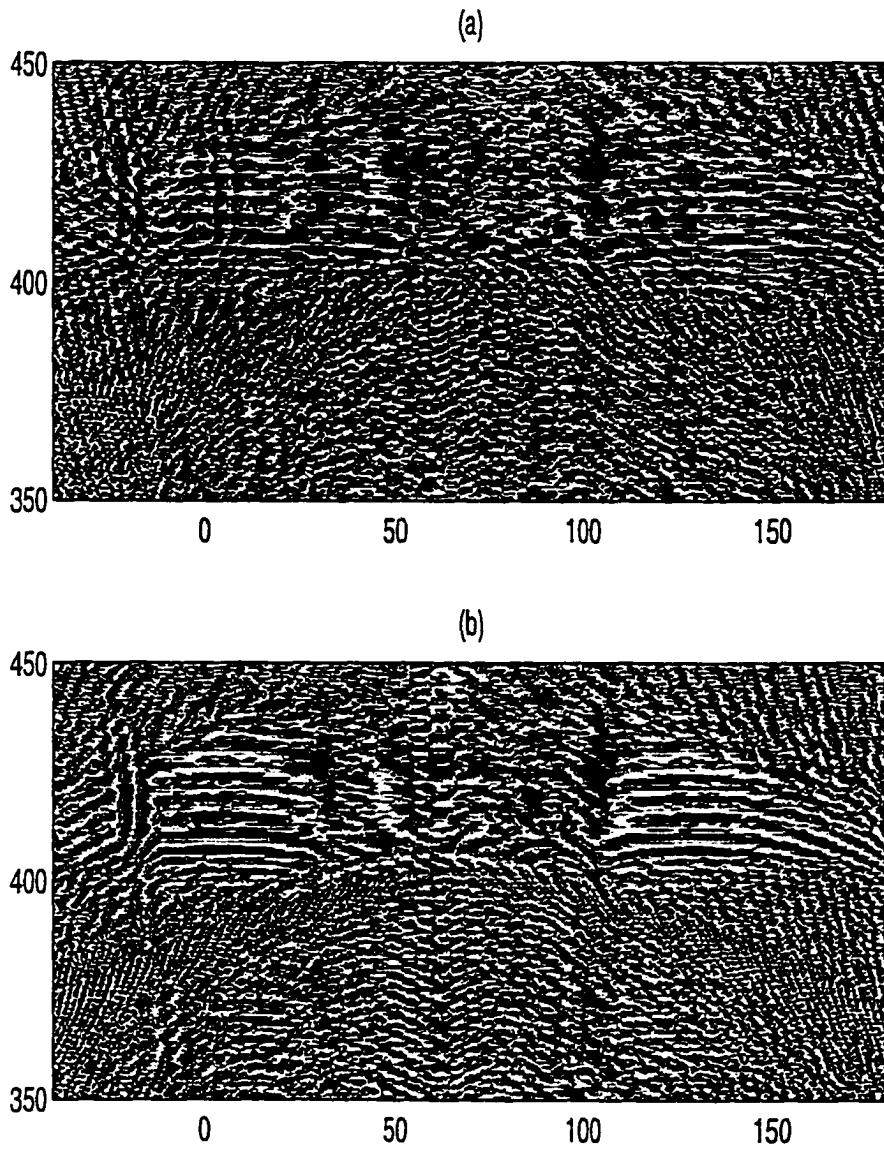


Figure 15.9 Interferograms: (a) before image registration, and (b) after image registration.

Table 15.1 Comparison of separations between wires

	$s1_x$	$s2_x$	$s1_z$	$s2_z$
From InSAR Image	79	38	20.96	23.37
From Measurement	79	38	19	22

GENERAL CONCLUSIONS

Summary of Major Results

A new approach for imaging embedded objects inside dielectric media has been developed. The approach is composed of several algorithms which can be either used independently for forming images or for determining dielectric permittivity, or used jointly for forming images without the prior knowledge the dielectric permittivity of the host material. Thanks to the appropriate data conversion among different domains, one is able (1) to minimize the effect of the specular reflections from the surfaces of the host material and to eliminate the effect of antenna horn mismatch; (2) to relate antenna physical looking angles to spatial spectra, thus reducing the interference from regions of no interest; and (3) to accelerate the image formation process by appropriately selecting one approach under given circumstances. Furthermore, the removed signal part due to specular reflections is not simply discarded. Information is instead extracted from this part and processed via algorithms proposed in Part I to provide permittivity for correct imaging. Another complimentary approach to obtaining the permittivity is from cross-correlating the positive and negative looking images based on an iterative process. Last, preliminary research in InSAR shows very promising potential for 3-D imaging.

All the algorithms developed are not only verified with simulation, but also by experiments. The experimental results show good agreements with simulations.

Future Research

The general problem of imaging embedded objects inside dielectric materials is rather complex. A lot of work lies ahead despite some achievements made here.

One area for future work is to improve the present experiments. A great deal of knowledge can be gained through experiments with more samples possessing different thicknesses, permittivities, and target distributions.

The second area for future work is to deepen the study of 3-D SAR imaging, particularly through interferometric SAR technique. This technique was briefly studied in Part III with some hopeful results. However, to really employ this technique we need to address the problems such as, among others, image registration and phase unwrapping.

The third area for future work is to modify imaging algorithms such that we can solve problems in which the host material is lossy and/or inhomogeneous.

The fourth area for future work is to incorporate fully polarimetric SAR. Results obtained in [123] indicate that better performance was achieved when using polarimetric whitening filter than when using a single-polarization channel.

The fifth area for future work is to use advanced signal/image processing techniques to relate the image to the nature of the targets, for example, their sizes, shapes, material composition, and so on.

REFLECTION COEFFICIENT CALCULATION FOR LINEAR PERMITTIVITY PROFILES

Reflection Coefficient

Closed form solution of EM fields in an inhomogeneous medium is only available for a restricted number of cases of $\epsilon(z)$ profiles. One of them is the linear profile, which is to be considered here. Assume we have a two-layered medium, with Region 1 being an inhomogeneous slab whose permittivity profile is linear, and Regions 0 and 2 being homogeneous and extending to infinity. The relative permittivity profile of the model is shown in Fig. A.1, where

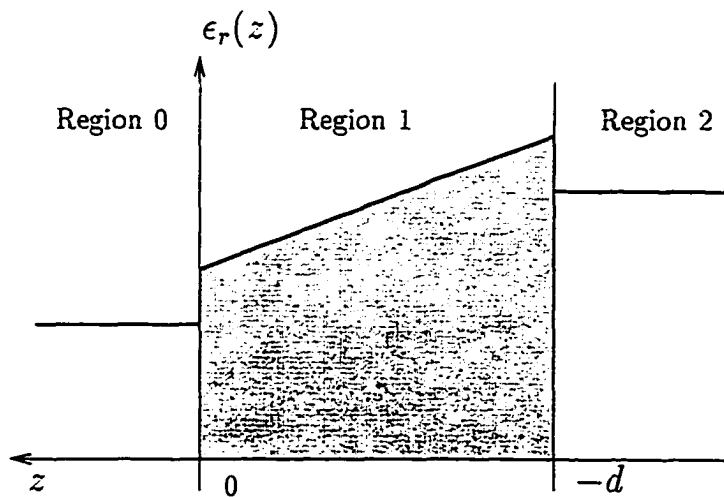


Figure A.1 Relative permittivity profile.

$$\begin{cases} \epsilon_{r0}(z) = 1, & z > 0 \\ \epsilon_{r1}(z) = \epsilon_r(0) + [\epsilon_r(0) - \epsilon_r(-d)]\frac{z}{d}, & 0 \geq z \geq -d \\ \epsilon_{r2}(z) = \epsilon_{r2}, & z < -d \end{cases} \quad (\text{A.1})$$

In Region 1, it is assumed that $\bar{E}^1 = \hat{y}E(z)e^{ik_x x}$, and the corresponding wave equation is [18]

$$\frac{d^2 E(z)}{dz^2} + k_{1z}^2 E(z) = 0 \quad (\text{A.2})$$

where, $k_{1z}^2 = \epsilon(z)\mu\omega^2 - k_x^2$. Let

$$A = [\epsilon_r(0) - \sin^2 \theta]k^2$$

and

$$B = \frac{[\epsilon_r(0) - \epsilon_r(-d)]}{d}k^2$$

then, (A.2) becomes

$$\frac{d^2 E(z)}{dz^2} + \{A + Bz\}E(z) = 0. \quad (\text{A.3})$$

Changing variables by denoting

$$\eta = B^{1/3}\left(z + \frac{A}{B}\right)$$

we end up with

$$\left(\frac{d^2}{d\eta^2} + \eta\right)E(z) = 0. \quad (\text{A.4})$$

This is the Airy equation, whose solution is

$$E(z) = \{C_1 A_i(-\eta) + C_2 B_i(-\eta)\}E_0 \quad (\text{A.5})$$

where $A_i(-\eta)$ and $B_i(-\eta)$ are Airy functions.

Now, from (A.5) we are able to set up four linear equations by virtue of continuity of tangential components of both electric and magnetic fields at $z = 0$ and $z = -d$, viz.,

$$1 + R = C_1 a_1 + C_2 a_2 \quad (\text{A.6})$$

$$T e^{ik_2 z d} = C_1 a_3 + C_2 a_4 \quad (\text{A.7})$$

$$ik_z(1 - R) = B^{1/3}[C_1 a_5 + C_2 a_6] \quad (\text{A.8})$$

$$ik_{2z} T e^{ik_2 z d} = B^{1/3}[C_1 a_7 + C_2 a_8] \quad (\text{A.9})$$

where

$$\left\{ \begin{array}{l} a_1 = A_i \left(-\frac{A}{B^{2/3}}\right) \\ a_2 = B_i \left(-\frac{A}{B^{2/3}}\right) \\ a_3 = A_i \left(-B^{1/3} \left(\frac{A}{B} - d\right)\right) \\ a_4 = B_i \left(-B^{1/3} \left(\frac{A}{B} - d\right)\right) \\ a_5 = A'_i \left(-\frac{A}{B^{2/3}}\right) \\ a_6 = B'_i \left(-\frac{A}{B^{2/3}}\right) \\ a_7 = A'_i \left(-B^{1/3} \left(\frac{A}{B} - d\right)\right) \\ a_8 = B'_i \left(-B^{1/3} \left(\frac{A}{B} - d\right)\right) \\ b_1 = \frac{ik_{2z}}{B^{1/3}} a_3 - a_7 \\ b_2 = a_8 - \frac{ik_{2z}}{B^{1/3}} a_4 \end{array} \right. \quad (\text{A.10})$$

where, " ' " indicating derivative with respect to z .

There are four unknown coefficients. However, we are only interested in one of them, namely, R . The solution is obtained as

$$R = \frac{\gamma_1 - \gamma_2}{\gamma_1 + \gamma_2} \quad (\text{A.11})$$

in which

$$\left\{ \begin{array}{l} \gamma_1 = \left(b_2 + \frac{b_1 a_2}{a_1}\right) \frac{ib_1 k_z}{B^{1/3} a_5} \\ \gamma_2 = \left(b_2 + \frac{b_1 a_6}{a_5}\right) \frac{b_1}{a_1} \end{array} \right. \quad (\text{A.12})$$

Programming

In order to calculate the reflection coefficient based on the foregoing solution, Airy functions are expressed in terms of Bessel functions in the following manner [29]

$$\begin{cases} A_i(-z) = \sqrt{z}/3 [J_{1/3}(\xi) + J_{-1/3}(\xi)] \\ B_i(-z) = \sqrt{z}/3 [J_{-1/3}(\xi) - J_{1/3}(\xi)] \\ A'_i(-z) = -z/3 [J_{-2/3}(\xi) - J_{2/3}(\xi)] \\ B'_i(-z) = z/\sqrt{3} [J_{-2/3}(\xi) + J_{2/3}(\xi)] \end{cases} \quad (\text{A.13})$$

where J is the Bessel function of the first kind, ξ is defined as $\xi = \frac{2}{3}z^{3/2}$.

MATLAB is used to take the advantage of the supplied Bessel functions. However, as negative order is prohibited in MATLAB, relations between different kinds of Bessel functions are used, providing

$$Y_\nu = \frac{J_\nu \cos(\nu\pi) - J_{-\nu}(z)}{\sin(\nu\pi)}. \quad (\text{A.14})$$

where Y is the Bessel function of the second kind, and ν is a real number.

Simulations

Two examples are simulated here to compare the exact solution with that of the multi-layer model. In both cases the frequency range is 75 – 110 GHz.

- Case 1: The parameters are $d = 8$ mm, $\epsilon_r(0) = 2$, $\epsilon_r(-d) = 4$, $\epsilon_{r2} = 1$.
- Case 2: The parameters are $d = 8$ mm, $\epsilon_r(0) = 2$, $\epsilon_r(-d) = 20$, $\epsilon_{r2} = 1$.

The results are given in Figs. A.2 and A.3. It is seen from the figures that multi-layer model works well when enough number of layers is used, which is dependent upon the permittivity profile, the thickness of the slab, and the frequency range being considered. The advantage of multi-layer model is that it needs far less computation time and can approach basically any profile with good accuracy.

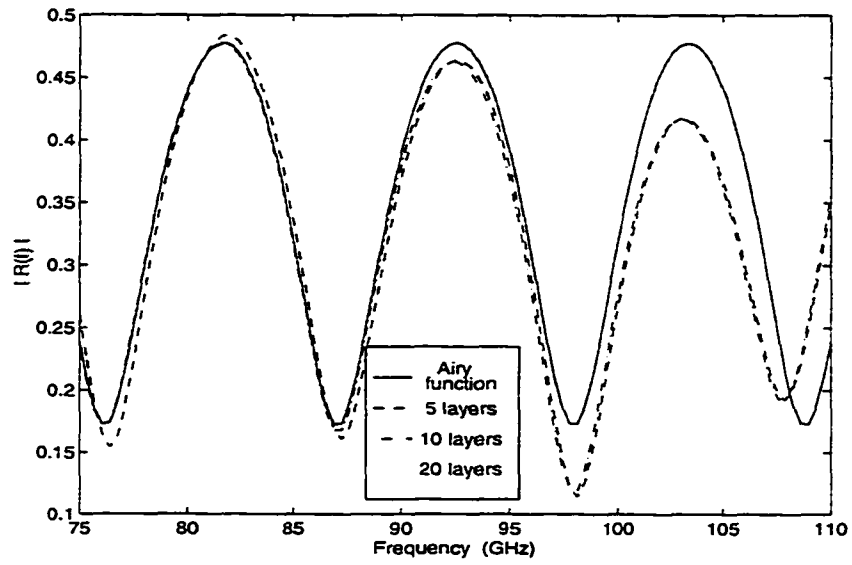


Figure A.2 Magnitudes of reflection coefficients for Case 1.

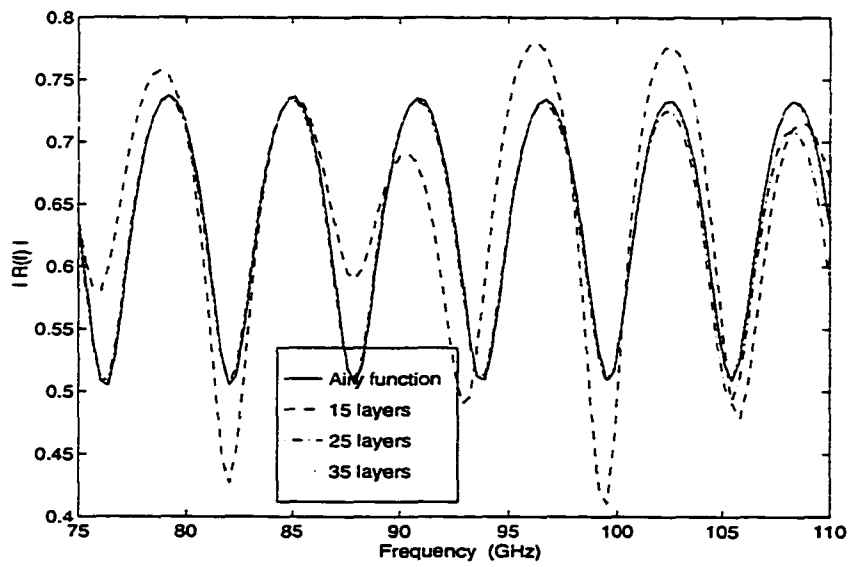


Figure A.3 Magnitudes of reflection coefficients for Case 2.

REFERENCES

- [1] J. J. Xia, *Electromagnetic Inverse Methods and Applications for Inhomogeneous Media Problems and Synthesis*, Ph.D. Thesis, M. I. T., 1992.
- [2] I. Kay, "The inverse scattering problem," Research Report EM-74, New York University, New York, 1955.
- [3] A. K. Jordan and H. N. Kirtikos, "An application of one-dimensional inverse scattering theory for inhomogeneous region," *IEEE Trans. Antenna and Propagation*, AP-22, p. 737, 1973.
- [4] A. K. Jordan and H. D. Ladouceur, "Renormalization of an inverse-scattering theory for discontinuous profiles," *Physics Review A*, Vol.36, No. 9, pp. 4245-4253, Nov., 1987.
- [5] D. L. Jaggard and Y. Kim, "Accurate one-dimensional inverse scattering using a nonlinear renormalization technique," *J. Opt. Soc. Am. A*, Vol.2, No. 11, pp. 1922-1930, Nov., 1985.
- [6] L. Rayleigh (J. W. Strutt), "On the reflection of light from a regularly stratified medium," *Proc. R. Soc. London A93*, pp. 565-577, 1917.
- [7] M. Born, "Quantenmechanik der Stossvorgange," *Z. Phys.* 37, pp. 803-827, 1926.
- [8] T. M. Habashy, E. Y. Chow and D. G. Duley, "Profile inversion using the renormalized source-type integral equation approach," *IEEE Trans. on Antennas and Propagation*, Vol. AP-38, pp. 668-682, May, 1990.
- [9] I. M. Gel'fand and L. S. Levitan, "On the determination of a differential equation by its spectral function," *Izv. Akad. Nauk SSSR Ser. Mat.*, Vol. 15, pp. 309-366, 1951. (Translation in *Amer. Math. Soc. Transl.*, Vol. 2, pp. 253-304, 1955.)
- [10] V. A. Marchenko, "The construction of the potential energy from the phases of the scattered waves," *Dokl. Akad. Nauk SSSR*, Vol. 104, pp. 695-698, 1955; also *Math. Rev.*, Vol. 17, p.740., 1956.
- [11] S. A. Schekunoff, "Remarks concerning wave propagation in stratified media." *The Theory of Electromagnetic Waves*, M. Kline, ed., New York: Interscience, pp. 181-192, 1951.

- [12] E. F. Bolinder, "Fourier transforms and tapered transmission lines," Proc. IRE 44, pp. 557-562, 1956.
- [13] D. B. Ge, D. L. Jaggard, and H. N. Kritikos, "Perturbation and high frequency profile inversion," IEEE Trans. on Antennas and Propagation, AP-31, pp. 804-808, 1983.
- [14] H. D. Ladouceur and A. K. Jordan, "Renormalization of an inverse scattering theory for inhomogeneous dielectrics," J. Opt. Soc. Am. A2, pp. 1916-1921, 1985.
- [15] T. M. Habashy and R. Mittra, "Review of some inverse methods in electromagnetics," J. Opt. Soc. Am. A, pp. 281-291, 1987.
- [16] K. I. Hopcraft and P. R. Smith, "Geometrical properties of backscattered radiation and their relation to inverse scattering," J. Opt. Soc. Am. A 6, pp. 508-516, 1989.
- [17] K. Sato, T. Manabe, J. Polivka, T. Ihara, Y. Kasashima, and K. Yamaki, "Measurement of the complex refractive index of concrete at 57.5 GHz," IEEE Trans. on Antennas and Propagation, Vol. 44, No. 1, pp. 35-40, January, 1996.
- [18] W. C. Chew, *Waves and Fields in Inhomogeneous Media*, New York: VRR, 1990.
- [19] J. A. Kong, *Electromagnetic Wave Theory*, New York: Wiley, 1990.
- [20] C. A. Balanis, *Advanced Engineering Electromagnetics*, New York: Wiley, 1989.
- [21] T. J. Cui and C. H. Liang, "Nonlinear differential equation for the reflection coefficient of an inhomogeneous lossy medium and its inverse scattering solutions," IEEE Trans. Antennas Propagat., Vol.42, No.5, pp. 621-626, 1994.
- [22] J. Zhang, *Synthetic Aperture Radar Imaging of Buried Objects in Dielectric Slabs*, Research Prospectus for Ph.D. Dissertation, Iowa State University, Oct, 1996.
- [23] J. E. Freund, *Mathematical Statistics*, Upper Saddle River, NJ: Prentice Hall, Inc., Fifth Edition, 1992.
- [24] HP 8510C Network Analyzer, *Operating and Programming Manual*, Cupertino, CA: Hewlett Packard, 1991.
- [25] R. Chatterjee, *Advanced Microwave Engineering*, New York: Halsted Press, 1988.
- [26] J. F. Nye and W. Liang, "Theory and measurement of the field of a pyramidal horn," Vol. 44, No. 11, pp. 1488-1498, Nov., 1996.
- [27] C. A. Balanis, *Antenna Theory: Analysis and Design*, New York: Wiley, 1982.
- [28] K. H. Breeden and A. P. Sheppard, "A note on the millimeter and submillimeter wave dielectric constant and loss tangent value of some common materials," Radio Science, Vol. 3 (New Series), No. 2, p. 205, 1968.
- [29] M. Abramowitz and I. A. Stegun, *Handbook of Mathematical Functions*, New York: Dover, 1972.

- [30] C. W. Sherwin, J. P. Ruina and R. D. Rawcliffe, "Some early developments in synthetic aperture radar systems," IRE Trans. on Military Electronics, Vol.MIL-6, No.2, pp. 111-115, April, 1962.
- [31] C. A. Wiley, "Synthetic aperture radar," IEEE Trans. on Aerospace and Electronic Systems, Vol.AES-21, No.3, pp. 440-443, May, 1985.
- [32] N. Ida, *Microwave NDT*, Dordrecht, The Netherlands: Kluwer Academic Publishers, 1992.
- [33] B. L. Burns and J. T. Cordaro, "A SAR image-formation algorithm that compensates for the spatially-variant effects of antenna motion," SPIE Vol. 2230, pp. 14-24, 1994.
- [34] B. R. Hunt and T. M.Cannon, "Nonstationary assumptions for Gaussian models of images," IEEE Trans. on Syst., man, and Cybernetics, pp. 876-881, December, 1976.
- [35] I. S. Reed and X. Yu, "Adaptive multiple-band CFAR detection of an optical pattern with unknown spectral distribution," IEEE Trans. on Signal Processing, Vol.38, pp. 1760-1770, October, 1990.
- [36] J. Li and E. G. Zelnio, "Target detection with synthetic aperture radar and coherent subtraction," SPIE Vol.2230, pp. 315-326, April, 1994.
- [37] L. M. Novak, M. C. Burl, and W. W. Irving, "Optical polarimetric processing for enhanced target detection," IEEE Trans. on Aerospace and Electronic Systems, Vol.29, pp. 234-244, January, 1993.
- [38] R. D. Chaney, A. S. Wukksy, and L. M. Novak, "Coherent aspect-dependent SAR image formation," SPIE Vol.2230, pp. 256-274, April, 1994.
- [39] T. Ozdemir, S. Roy, and R. Berkowitz, "Imaging of shallow subsurface objects: An experimental investigation," IEEE Trans. on Geoscience and Remote Sensing, Vol. 30, No. 3, pp. 472-481, May, 1992.
- [40] J. G. Proakis and D. G. Manolakis, *Introduction to Digital Signal Processing*, Chapter 6, New York: Macmillan, 1988.
- [41] G. Gilbert, M. Braunstein and J. Ralston, "Characterizing and correcting media-induced focus errors in synthetic aperture radar imagery," SPIE Vol. 2230, pp. 87-104, 1994.
- [42] S. R. DeGraaf, "SAR imaging via modern 2-D spectral estimation methods," SPIE Vol. 2230, pp. 36-47, 1994.
- [43] J. Walker, "Range-Doppler imaging of rotating objects," IEEE Trans. on AES, Vol. AES-16, No. 1, pp. 23-52, 1980.
- [44] M. Soumekh, "A system model and inversion for synthetic aperture radar imaging," IEEE Trans. on Image Proc., Vol. 1, No. 1, pp. 64-76, 1992.

- [45] E. E. Hilbert and C. F. Chang, "Bayesian neural network ATR for multifeature SAR," SPIE Vol. 2230, pp. 344-355, 1994.
- [46] L. I. Perlovsky, W. H. Schoendorf, B. J. Burdick, and D. M. Tye, "Model-based neural network for target detection in SAR images," IEEE Trans. on Image Processing, Vol. 6, No. 1, pp. 203-216, January, 1997.
- [47] A. W. Rihaczek, *Principles of High-Resolution Radar*, New York: McGraw-Hill, Inc., 1969.
- [48] J. C. Curlander and R. N. McDonough, *Synthetic Aperture Radar*, New York: John Wiley & Sons, Inc., 1991.
- [49] C. Elachi, *Spaceborne Radar Remote Sensing: Applications and Techniques*, New York: IEEE Press, 1988.
- [50] S. L. Johnston, "Target model pitfalls (illness, diagnosis, and prescription)," IEEE Trans. on AES, Vol. 33, No. 2, pp. 715-720, April, 1997.
- [51] R. P. Flaw, D. J. Farina and J. M. Liu, "Detection/location of small flaws in composite structures using microwaves," Review of Progress in Quantitative Nondestructive Evaluation, Vol. 15, pp. 679-685, New York: Plenum Press, 1996.
- [52] J. A. Sheer and J. L. Kurtz, (editors) *Coherent Radar System Performance Estimation*, Dedham, MA: Artech House, 1993.
- [53] Y. Yamagnchi, M. Mitsumoto, M. Sengoku, and T. Abe, "Synthetic aperture FM-CW radar applied to the detection of objects buried in snowpack," IEEE Trans on Geoscience and Remote Sensing, Vol. 32, No. 1, pp. 11-18, Jan., 1994.
- [54] A. W. Rihaczek, "Radar resolution of ideal scatters," IEEE Trans. on AES, Vol. 32, No. 2, pp. 842-845, April, 1996.
- [55] D. L. Mensa, *High Resolution Radar Imaging*, Dedham, MA: Artch House, Inc., 1981.
- [56] J. P. Fitch, *Synthetic Aperture Radar*, New York: Springer-Verlag Inc., 1988.
- [57] K. Tomiyasu, "Tutorial review of synthetic-aperture radar (SAR) with applications to imaging of the ocean surface," Proc. of the IEEE, Vol.66, No.5, pp. 563-584, May, 1978.
- [58] R. Voles, "Resolving revolutions: imaging and mapping by modern radar," IEE Proc. - F, Vol.140, No. 1, pp. 1-11, February, 1993.
- [59] L. J. Cutrona, E. N. Leith, L. J. Porcello and W. E. Vivian, "On the application of coherent optical processing techniques to synthetic-aperture radar," Proc. of the IEEE, Vol.54, No.8, pp. 1026-1032, Aug., 1966.

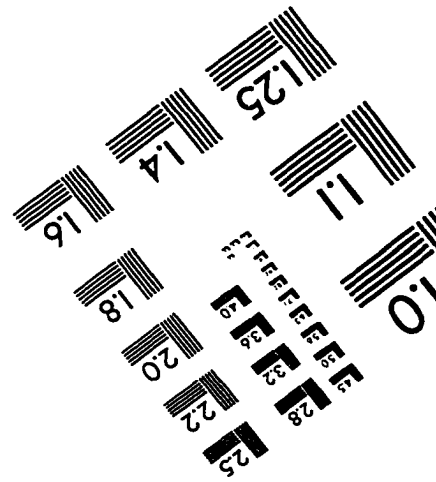
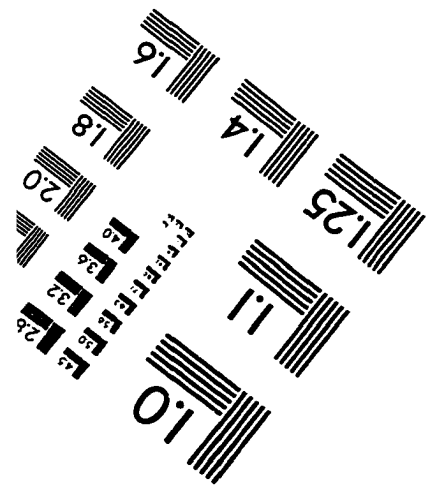
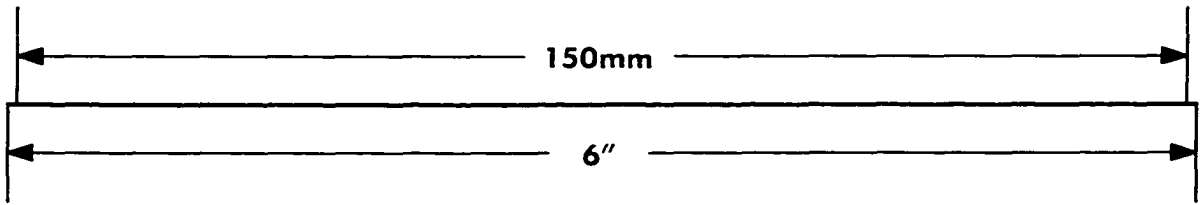
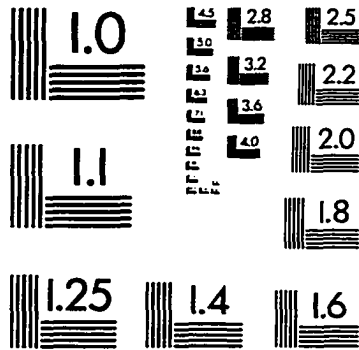
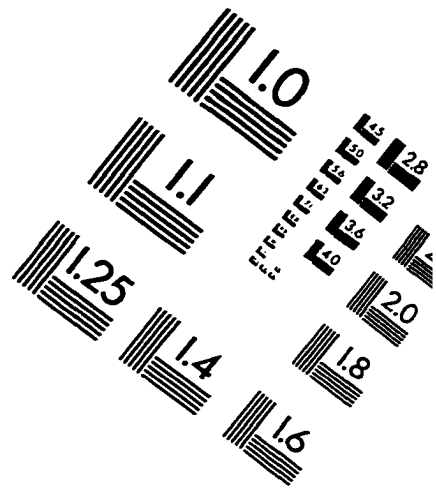
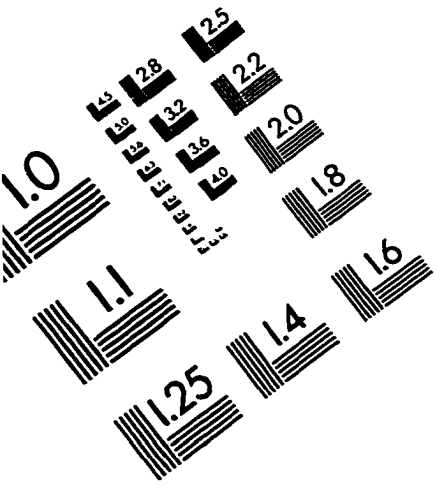
- [60] D. E. Wall, P. H. Eichel, D. C. Ghiglia, and C. V. Jakowatz, Jr., "Phase gradient autofocus – a robust tool for high resolution SAR phase correction," *IEEE Trans. on AES*, Vol. 30, No. 3, pp. 827-834, July, 1994.
- [61] D. O. North, "An analysis of the factors which determine signal-noise discrimination in pulsed carrier system," RCA Lab. Rept. PTR-6C, June, 1943.
- [62] P. M. Woodward, *Probability and Information Theory, with Application to Radar*, New York: Pergamon Press, 1953.
- [63] A. D. Whalen, *Detection of Signals in Noise*, New York: Academic Press, 1971.
- [64] A. Langman and M. R. Inggs, "Improving the resolution of a stepped frequency CW ground penetrating radar," *SPIE Vol.2275*, pp. 146-155, 1994.
- [65] C. Elachi, *Introduction to the Physics and Techniques of Remote Sensing*, New York: John Wiley & Sons, Inc., 1987.
- [66] W. G. Carrara, R. S. Goodman and R. M. Majewski, *Spotlight Synthetic Aperture Radar*, MA: Artch House, Inc., 1995.
- [67] D. E. Newland, *Random Vibrations, Spectral and Wavelet Analysis*, New York: John Wiley & Sons, Third Edition, 1993.
- [68] J. G. Proakis and D. G. Manolakis, *Digital Signal Processing — Principles, Algorithms, and Applications*, Upper Saddle River, NJ: Prentice Hall, 1996.
- [69] F. J. Harris, "On the use of windows for harmonic analysis with the discrete Fourier transform," *Proc. of the IEEE*, Vol.66, No.1, pp. 51-83, Jan., 1978.
- [70] H. C. Stankwitz, R. J. Dallaire, and J. R. Fienup, "Nonlinear apodization for side-lobe control in SAR imagery," *IEEE Trans. on AES*. Vol. 31. No. 1. pp. 267-278, April, 1995.
- [71] R. L. Mitchell, *Radar Signal Simulation*, Dedham, MA: Artech House, 1976.
- [72] H. C. Han and C. S. Wang, "Coherent microwave imaging for buried objects," *Review of Progress in QNDE*, 14A, pp. 607-613, 1995.
- [73] E. M. Johansson and J. E. Mast, "Three-dimensional ground penetrating radar imaging using synthetic aperture time-domain focusing," *SPIE Vol. 2275*, pp. 205-214, 1994.
- [74] Microwave NDE Group, Department of Electrical Engineering and Computer Engineering, Iowa State University, FORTRAN program: *genhs.f*, 1994.
- [75] Y. Ozaki, H. Sumitani, T. Tomoda, and M. Tanaka, "A new system for real-time synthetic aperture ultrasonic imaging," *IEEE Trans. on Ultrasonics, Ferroelectrics, and Frequency Control*, Vol. 35, No. 6, Nov. pp. 828-838, 1988.

- [76] S. Barbarossa and A. Farina, "Space-time-frequency processing of synthetic aperture radar signals." IEEE Trans. on Vol. 30, No. 2, pp. 341-358, April, 1994.
- [77] J. C. Liu and T. P. Lin, "Short-time Hartley transform," IEE Proc. - F, Vol. 140, No. 3, pp. 171-174, June, 1993.
- [78] I. Daubechies, *Ten Lectures on Wavelets*, Philadelphia: SIAM, 1992.
- [79] C. K. Chui, *An Introduction to Wavelets*, New York: Academic Press, 1992.
- [80] Y. Meyer, *Wavelets: Algorithms and Application*, Philadelphia: SIAM, 1992.
- [81] G. Kaiser, *A Friendly Guide to Wavelets*, Boston: Birkhauser, 1994.
- [82] Y. T.Chan, *Wavelet Basics*, Boston: Kluwer Academic Publishers, 1995.
- [83] S. Mallat and S. Zhong, "Characterization of signals form multiscale edges," IEEE Trans. on Pattern Analysis and Machine Intelligence, Vol. 14, No. 7. pp. 710-732, July, 1992.
- [84] R. A. Carmona, "Wavelet identification of transients in noisy time series." SPIE. Mathematical Imaging, Vol. 2034, pp. 392-400, 1993.
- [85] L. Cohen, "Time-frequency distributions - A review," Proc. IEEE, Vol. 77, No. 7, pp. 941-981, July, 1989.
- [86] R. Altes, "Detection, estimation and classification with spectrograms," J. Acoust. Soc. Am., Vol. 67, pp. 1232-1246, 1980.
- [87] A. Dziewibski, S. Bloch, and M. Landisman, "A technique for the analysis of transient signals," Bull. Seism. Soc. Am., Vol. 59, pp. 427-444, 1969.
- [88] K. Kodera, C. de Villedary, and R. Gendrin, "A new method for the numeral analysis of non-stationary signals," Phys. Earth and Planetary Interiors, Vol. 12, pp. 142-150, 1976.
- [89] K. Kodera, R. Gendrin, and C. de Villedary, "Analysis of time-varying signals with small BT values," IEEE Trans. Acoust., Speech, Signal Processing, Vol. ASSP-26, pp. 64-76, 1978.
- [90] A. L. Levshin, V. F. Pisarenko, and G. A. Pogrebinsky, "On a frequency-time analysis of oscillations," Ann. Geophys., Vol. 28, pp. 211-218, 1972.
- [91] A. V. Oppenheim, " Speech spectrograms using the fast Fourier transform," IEEE Spectrum, Vol. 7, pp. 57-62, 1970.
- [92] M. R. Portnoff, "Time-frequency representation of digital signals and systems based on short-time Fourier analysis," IEEE Trans. Acoust., Speech, Signal Processing, Vol. ASSP-28, pp. 55-59, 1980.

- [93] R. W. Schafer and L. R. Rabiner, "Design and simulation of a speech analysis-synthesis system based on short-time Fourier analysis," *IEEE Trans. Audio Electroacoust.*, Vol. AU-21, pp. 165-174, 1973.
- [94] K. Kristoffersen, "Time-domain estimation of the center frequency and spread of Doppler spectra in diagnostic ultrasound," *IEEE Trans. Ultrason., Ferro., and Freq. Control*, Vol. 35, No. 4, pp. 484-497, July, 1988.
- [95] P. Flandrin, "A time-frequency formulation of optimum detection," *IEEE Trans. Acoust., Speech, Signal Processing*, Vol.-36, No. 9, pp. 1377-1384, Sept., 1988.
- [96] M. Wang and Z. Bao, "Modified short-time Fourier transform," *Optical Eng.*, Vol. 34, No. 5, pp. 1333-1336, May, 1995.
- [97] J. Flanagan, *Speech Synthesis and Perception*, New York: Springer, 1972.
- [98] M. H. Ackroyd, "Short-time spectra and time-frequency energy distributions," *J. Acoust., Soc., Am.*, Vol. 50, pp. 1229-1231, 1970.
- [99] M. I. Skolnik, *Introduction to Radar Systems*, New York: McGraw-Hill, 1980.
- [100] J. B. Allen and L. R. Rabiner, "A unified approach to short-time Fourier analysis and synthesis," *Proc. IEEE*, Vol. 65, No. 11, pp. 1558-1564, Nov., 1977.
- [101] D. C. Munson, Jr and R. L. Visentin, "A signal processing view of strip-mapping synthetic aperture radar," *IEEE Trans. on ASSP*, Vol. 37, No. 12, pp. 2131-2147, December, 1989.
- [102] H. C. Han and M. T. Lusk, "Coherent and incoherent components in microwave SAR images," *Rev. Prog. Quant. Nondest. Eval.*, Vol. 13A, pp. 599-605, New York: Plenum Press, 1994.
- [103] H. C. Han and C. S. Wang, "Microwave imaging in inhomogeneous media," *SPIE*, Vol. 2275, pp. 226-230, 1994.
- [104] J. C. Proakis, *Digital Communications (3rd Edition)*, New York: McGraw-Hill, 1995.
- [105] J. Eberhart, "Radar reveals an asteroid's strange shape," *Science News*, p. 343, Nov. 25, 1989.
- [106] L. E. Kopilovich, "New approach to constructing two-dimensional aperture synthesis systems," *IEE Proc. - F*, Vol. 139, No. 5, pp. 365-368, October, 1992.
- [107] K. Knaell, "Three dimensional SAR from curvilinear aperture," *SPIE*, Vol. 2230, pp. 120-134, 1994.
- [108] M. D. Desai, "Spotlight mode SAR stereo technique for height computation," *IEEE Trans. on Image Processing*, Vol. 6, No. 10, pp. 1400-1411, October, 1997.
- [109] L. C. Graham, "Synthetic interferometer radar for topographic mapping," *Proc. of the IEEE*, 62(2), pp. 763-768, 1974.

- [110] C. T. Allen, "Interferometric synthetic aperture radar," *IEEE Geoscience and Remote Sensing Society Newsletter*, pp. 6-13, Sept., 1995.
- [111] C. V. Jakowatz, Jr. and D. E. Wahl, "New formulation for interferometric synthetic aperture radar for terrain mapping," *SPIE Vol. 2230*, pp. 411-418, 1994.
- [112] F. K. Li and R. M. Goldman, "Studies of multibaseline spaceborne interferometric synthetic aperture radars," *IEEE Trans. on Geosci. and Remote Sens.*, 28(1), pp. 88-97, 1990.
- [113] C. Prati and F. Rocca, "Limits to the resolution of elevation maps from stereo SAR images," *Int. J. Remote Sensing*, Vol. 11, No. 12, pp. 2215-2235, 1990.
- [114] R. M. Goldstein, H. A. Zebker, and C. L. Werner, "Satellite radar interferometry: two-dimensional phase unwrapping," *Radio Science*, Vol.23, No. 4, pp. 713-720, 1988.
- [115] M. D. Pritt and J. S. Shipman, "Least-squares two-dimensional phase unwrapping using FFT's " *IEEE Trans. Geoscience and Remote sensing*, Vol. 32, No. 3, pp.706-708, May, 1994.
- [116] D. Just, N. Adam, M. Schwabisch, and R. Bamler, "Comparison of phase unwrapping algorithms for SAR interferograms," *IEEE*, pp. 767-769, 1995.
- [117] H. Lim, W. Xu, X. Huang, "Two new practical methods for phase unwrapping," *IEEE*, pp. 196-198, 1995.
- [118] C. R. Guarino, "Weighted two-dimensional phase unwrapping," *IEEE*, pp. 193-195, 1995.
- [119] D. Labrousse, S. Dupont, and M. Berthod, "SAR interferometry: a Markovian approach to phase unwrapping with a discontinuity model," *IEEE*, pp. 556-558, 1995.
- [120] T. J. Flynn, "Two-dimensional phase unwrapping with minimum weighted discontinuity," *J. Opt. Soc. Am., A*/Vol. 14, No. 10, pp. 2692-2701, October, 1997.
- [121] G. Fornaro, G. Franceschetti, R. Lanari, E. Sansosti, and M. Tesauro, "Global and local phase-unwrapping techniques: a comparison," *J. Opt. Soc. Am., A*/Vol. 14, No. 10, pp. 2702-2708, October, 1997.
- [122] Q. Lin, J. F. Vesecky, and H. A. Zebker, "New approaches in interferometric SAR data processing," *IEEE Trans. on Geosci. and Remote Sens.*, 30(3), pp. 560-567, 1992.
- [123] L. M. Novak, S. D. Halversen, G. J. Owirka, and M. Hiett, "Effects of polarization and resolution on SAR ATR," *IEEE Trans. on AES*, Vol. 33, No. 1, pp. 102-115, April, 1997.

IMAGE EVALUATION TEST TARGET (QA-3)



APPLIED IMAGE, Inc
 1653 East Main Street
 Rochester, NY 14609 USA
 Phone: 716/482-0300
 Fax: 716/288-5989

© 1993, Applied Image, Inc., All Rights Reserved